2005

Design, construction and initial testing of experimental test package for convective spray cooling in terrestrial gravity conditions

Charles Andy Hunnell
West Virginia University

Design, Construction and Initial Testing of Experimental Test Package for Convective Spray Cooling in Terrestrial Gravity Conditions

By

Charles Andy Hunnell

Thesis

Submitted to the College of Engineering and Mineral Resources
West Virginia University

In partial fulfillment of the requirements
for the degree of

Master of Science
in
Mechanical Engineering

Committee:

John M. Kuhlman, Ph.D., Chair
Donald Gray, Ph.D.
Gary Morris, Ph.D.
Wade Huebsch, Ph.D.

Department of Mechanical and Aerospace Engineering
2005

ABSTRACT

Design, Construction and Initial Testing of Experimental Test Package for Convective Spray Cooling in Terrestrial Gravity Conditions

Charles Andy Hunnell

The design and construction of an apparatus for preliminary spray cooling tests was completed to better understand the effects of spray cooling with different geometries at varied flow rates and different spray orientations. An inexpensive yet functional apparatus was constructed for use at West Virginia University to achieve baseline data for a spray chamber that will eventually fly on the NASA DC-9 simulated microgravity research aircraft. The apparatus sprays a refrigerant (FC-72) on to a heated surfaced which was confined in a spray chamber. Three different geometries were studied at four different spray volumetric flow rates varying from 9.3 GPH to 4.6 GPH. At each spray flow rate the heat flux of the small heated pedestal located in the spray chamber was increased from 5 W/cm^2 to 32.24 W/cm^2. During these tests the spray orientation was changed from a vertical downward spray to a horizontal spray. The geometries of the sump that was used to remove the fluid from the spray chamber varied from an unconfined flow to two different types of caps, which had different curvature inside the cap. These caps were used to cover the top of the sump and create confinement for flow management when in a microgravity environment.

Both the vertical downward and horizontal sprays displayed similar trends and showed that as the heat flux was increased the surface temperature also increased. The trend of the heat flux (W/cm^2) as a function of surface temperature (^oC) resembled an S shaped curve. Comparisons between the vertical downward and horizontal spray indicated that the heat transfer effectiveness of the vertical downward spray was more efficient than the horizontal spray conditions. Some preliminary flow visualizations were conducted to help understand the spray droplet flow physics and interaction with the vaporization on the heated surface.

TABLE OF CONTENTS:

LIST OF FIGURES:

LIST OF TABLES:

ACKNOWLEDGEMENTS:

I would like to thank the Air Force Office of Scientific Research for providing funding for the present experimental study of convective spray cooling. I would also like to thank Dr. Kirk Yerkes, Dr. Richard Harris and Mr. Travis Michalak at the Air Force Research Laboratory in Dayton Ohio who have been very helpful with advice and technical support on the experiment.

I would like to thank Mr. Cliff Judy for all the machining expertise and Mr. David Estep for all the help in wiring and electrical devices. I would also like to thank Mr. Chuck Coleman for his technical advice regarding electrical devices. I would like to thank Mr. An Chen of CEE for helping with the structural testing of the 80/20 material.

Mostly I would like to thank Dr. Kuhlman for all the inspiration, hard work, and time that he has given to help me with the experiment. I would also like to thank Dr. Gary Morris, Dr. Wade Huebsch, and Dr. Donald Gray for their expert advice in experimental work. I would also like to thank Dr. Sushant Aggarwal for helping with the calibration of the thermocouples. I would also like to thank Ms. Shannon Glaspell and Mr. Paul Kreitzer for technical help with both the apparatus and my thesis.

Lastly I would like to thank my family and fiancé for the emotional support that was greatly needed for the completion of the experiment. My family has always been very supportive and was desperately needed during my college years.

NOMENCLATURE:

A	Area of the heated surface on the pedestal
AFRL	Air Force Research Laboratories
CC	Curved Cap
CFDRC	Computational Fluid Dynamics Research Corp.
CHF	Critical Heat Flux
D	Diameter of spray droplets
Dia	Diameter of pedestal
FPS	Frames Per Second
FC-72	Fluorinert Electronic Liquid
GPH	Gallons Per Hour
h	Convective heat transfer coefficient
HS	Horizontal Spray
in	inches
ITO	Indium/tin oxide heater
lbs	Pounds
Ped.	Pedestal
Press.	Pressure (PSIA)
PSIA	Absolute Pounds per Square Inch
Ma	Marangoni number
Nozz	Nozzle
Q	Power
$\dot{Q}$	Rate of Heat Transfer
Re	Reynolds number
sat	saturation
SC	Straight Cap
SG	Simulated Microgravity
T_1-T_{14}	Thermocouples located through apparatus
X_1	Extra Thermocouples
TFR	Thick Film Resistor (ceramic)
TG	Terrestrial Gravity
UC	Unconfined
V	Velocity
VS	Vertical Spray
$\dot{V}$	Volumetric flow rate
We	Weber number
X	Heat Exchanger
μ	Viscosity of FC-72
ρ	Density of FC-72
σ	Surface tension of FC-72

CHAPTER 1 INTRODUCTION:

Future Air Force technologies envision several ways to use small high density power sources such as lasers in space applications. With the advancements in space applications, thermal management is becoming more important and will require more aggressive heat rejection processes. Modern heat removal methods cannot reject the required amount of heat for these advanced applications. Several different methods are being developed to find the most efficient process for the removal of large amounts of heat over a small area. Spray cooling, liquid jet impingement and pool boiling are three examples of the different methods that are being examined. Spray cooling has become an appealing process due to the large heat flux created. Each method is a dramatic improvement over natural convection, and all three generally use boiling. Boiling exploits the phase change in a liquid which uses latent heat of vaporization to further improve the attainable heat transfer coefficients and increases the critical heat fluxes (CHF's) in cooling systems (Baysinger, 2004).

With deep space travel goals being set and a need for small powerful microchips a process must also be developed that can remove heat over a small area. These microchips will produce large amounts of excess heat and are going to require a more efficient cooling process than the current cooling techniques.

The advancements of defense technology are leaning towards use of high powered lasers, especially in future space-based applications. These high powered sources will also require a more efficient cooling process. Both microchips and lasers are examples of small high-power density heat sources that will require a rejection of large amounts of waste heat, which enables them to be used repeatedly or steadily.

The long range goal of the current project is to enhance the usefulness of spray cooling in microgravity to increase the amount of achievable heat transfer. The research is part of an ongoing study of convective spray cooling sponsored by the Air Force Research Laboratories (AFRL) and in collaboration with the National Aeronautics and Space Administration (NASA). The planned follow-on research will focus on exploring the effectiveness of electrostatics to place an electric charge on a spray for fluid management and the use of a high speed camera for qualitative data analysis of spray and vapor bubble behavior.

The objective of this thesis is to design and construct an apparatus to be used at West Virginia University to study convective spray cooling in terrestrial gravity (vertical downward spray) and simulated microgravity (horizontal spray) conditions for high heat flux cooling applications. Portions of the developed apparatus will be used in future spray cooling studies in microgravity. The present research study will also investigate the effects of confined geometry, varying flow rates, and simulated microgravity environment (horizontal) sprays.

CHAPTER 2 LITERATURE REVIEW:

Chapter 2 is a summary of previous work that is related to the topics in this thesis. Topics to be covered include: spray cooling under terrestrial gravity conditions, spray cooling in microgravity conditions, pool boiling, liquid jet impingement, and effects of electro-hydrodynamics. Each topic will give a background needed to understand the importance of the present research.

2.1 Convective Spray Cooling in Terrestrial Gravity Conditions:

There are many reasons for using spray cooling. One reason is that spray cooling is considered to be one of the most efficient forms of heat removal over a small area when below the Leidenfrost point, but above the saturation temperature of the fluid (Tilton, 1989). The Leidenfrost point is the temperature for which the material's surface temperature is so high that a vapor layer forms between the material and the cooling liquid, causing the rate of cooling to decrease as the surface temperature is increased.

Of the various types of heat transfer that exploit phase change, spray cooling has the best performance in terms of large increases in heat transfer coefficient and critical heat flux (CHF) when compared to liquid jet impingement and pool boiling (Chow et al., 1997). The CHF occurs just before the Leidenfrost point, allowing the largest value of heat flux to occur.

Spray cooling heat transfer has contributions from two primary mechanisms: forced convection with mixing due to droplet impingement, and nucleate boiling. With water as the working fluid, spray cooling can demonstrate a heat flux on the order of 1000 W/cm^2 (Lin and Ponnappan, 2003). Lin and Ponnappan also show that water is a

more effective fluid in the removal of heat when compared to refrigerants such as FC-87 and FC-72. Water is shown to be an order of magnitude higher for cooling, but is not the fluid of choice due to inability to work with electronics, due to its poor dielectric properties.

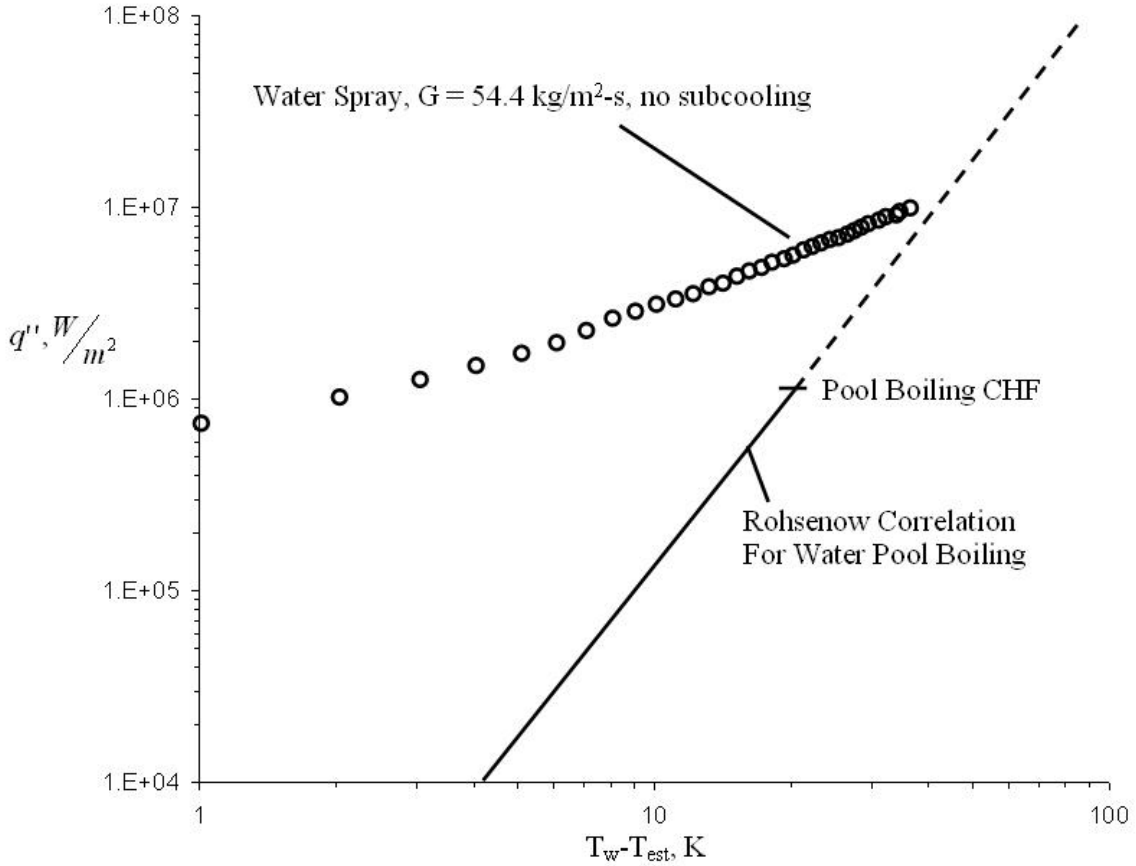

Figure 2.1: Chow et al. (1997) data showing the comparison between spray cooling and pool boiling

The typical heat transfer coefficients in spray cooling are an order of magnitude higher than in pool boiling (Chow, et al., 1997). Figure 2.1, taken from Chow et al., shows a comparison between spray cooling and pool boiling. Chow et al used data for the spray cooling from Tilton, 1989 and the data for the pool boiling from Rohsenow, 1985 for the comparison.

Spray cooling starts with a saturated or sub-cooled liquid impacting a heated surface. After the spray makes contact with the heater, the droplets interact with one another, giving rise to a thin liquid film on the heated surface (Chow et al., 1997). For pressure atomizing sprays the film has a wavy surface. Figure 2.2 shows Chow et al.'s explanation of the process of a spray impacting a heated surface.

The CHF is sparked by dry-out conditions during boiling. These conditions occur during spray cooling if the bubble mass flux production is greater than the amount of spray droplets impinging the surface. If the vapor bubbles are allowed to grow, creating a non wetted surface, macrolayer dry-out occurs.

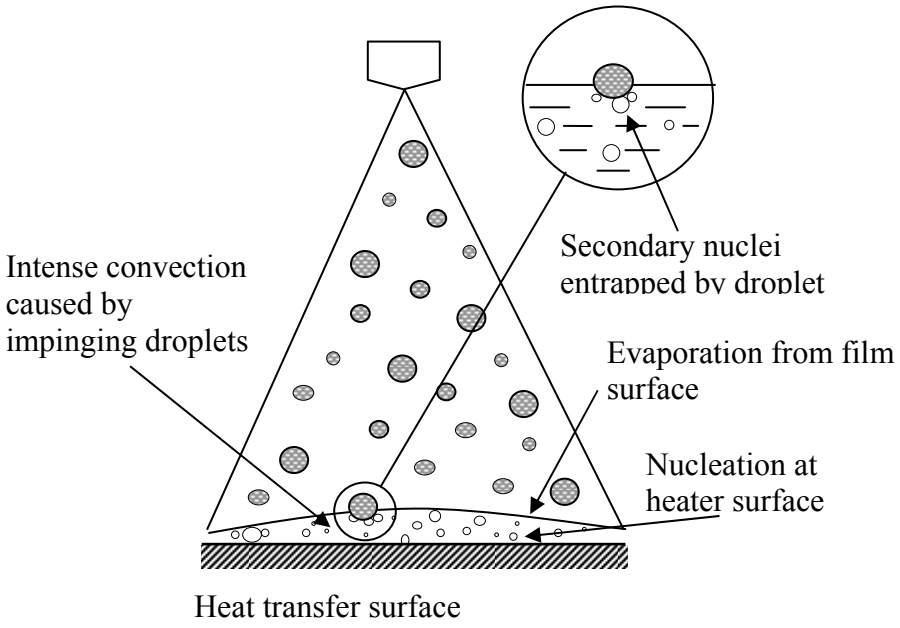

Figure 2.2: Vapor Bubble Interaction With Spray Droplets (Chow et al. 1997)

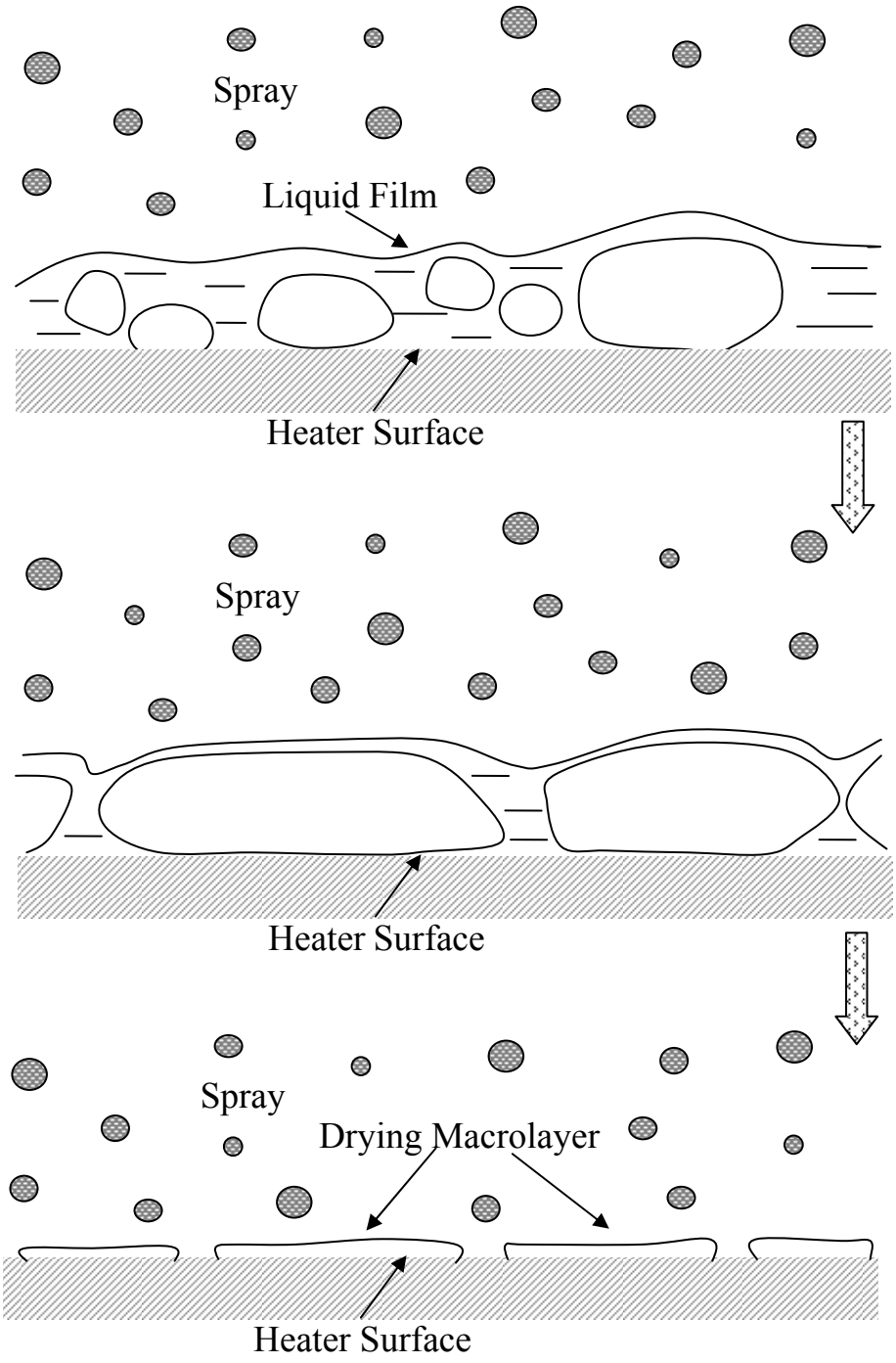

Figure 2.3: Macrolayer Dry-Out in Spray Cooling (Chow et al., 1997)

Figure 2.3 shows how an increase in bubble production from the heated surface can give rise to a larger vapor bubble. These larger vapor bubbles are broken down due to impinging droplets and the liquid forming the upper layer of these bubbles is blown

away due to vapor flow. Then the spray droplets will rewet the rapidly drying out surface.

The large difference between spray cooling and pool boiling is that pool boiling only uses evaporative cooling, while spray cooling also uses forced convection with mixing. These results account for observations in both terrestrial gravity and microgravity conditions.

A spray cooling generally results in more uniform heat flux when compared to a liquid jet. Liquid jet impingement creates large temperature gradients within the material being cooled and is discussed below in Section 2.4. The heat removal is mostly concentrated in the area of impact (stagnation region) and decreases rapidly once the fluid momentum is radial to the axis of the jet (Webb and Ma, 1992). Due to the momentum of the jet, it is considered an aggressive cooling technique and could be detrimental for electrical components depending on flow rates.

Different types of nozzles such as full cone, hollow cone, square, and rectangle have been studied by researchers at the Air Force Research Laboratories (AFRL) before a selection of an optimal one could be made. The experiment studied: nozzle droplet velocity distribution, nozzle droplet diameter as a function of position, and nozzle volumetric flux as a function of time. It was determined from the study that a full cone pressure atomizing nozzle with the capacity of 1 has the correct spray uniformity and droplet size for this project (Baysinger, et al. 2004). A full cone nozzle with capacity of 1 indicates that the flow rate will be 1 GPM at a pressure of 10 PSIG. A two-axis Dantec Phase Doppler Anemometer was used to conduct this experiment and resulted in the purchase of a Spraying Systems FullJet 1 nozzle. Even with this study of different types

of nozzles being completed, it has been noted by Chow et al. (1997) that the ability for two of the same nozzles to produce the same spray distributions is uncommon.

There are two broad classifications of spray generation, one being pressure atomization and the other a gas-assisted atomization. Pressure atomization is the most widely used method of spray generation and is when a high-pressure fluid is injected into a low-pressure surrounding, typically at ambient conditions (Chow et al., 1997). These nozzles generally use a swirling motion to create the droplets and cone angle size. The swirling motion is usually generated with flutes that are mounted inside the nozzle. Gas-assisted atomization uses a high velocity gas, usually air, which is injected into a fine stream of liquid. The shear force of the gas being injected into the liquid as it exits the orifice is what creates the droplets, through a combination of shear and instability.

Comparing pressure and air assisted atomization the CHF and heat transfer coefficients for the air atomized spray are comparable to pressure atomized spray, although the required flow rates are more than ten times lower for the gas-assisted spray (Chow, et al., 1997). Chow, Sehmbey, and Pais (1997) present an experimental study where the pressure atomized water spray had a mass flux of 52 kg/m^2s and the air atomized water spray was only 4.5 kg/m^2s, although both produced roughly the same amount of heat transfer. One disadvantage to pressure-assisted nozzles is that for lower flow rates, a small orifice is required and this increases the chances of blockage. Gas-assisted nozzles are not subject to this problem, but the main disadvantage to a gas-assisted nozzle is that it requires the use of a secondary gas. It is very difficult to use the gas-assisted nozzles in a closed loop due to problems in collecting the secondary gas.

Further classifications of sprays are high and low density. High density is when the spray is dense enough to keep a film on the heated surface of the material. For clarification a high-density spray always has more liquid supplied than the amount being evaporated. A low-density spray is when the individual droplets do not interact with one another. Due to the lack of droplet interaction the only heat transfer process is evaporative cooling (Chow, et al., 1997).

Some primary spray parameters are the liquid flow rate per unit area or volumetric flux, the mean diameter of the droplets, and the spray velocity. For a pressure-assisted nozzle all the primary parameters are controlled by the geometry and driving pressure. Chow et al. have shown a study where as the driving pressure was increased, the volumetric flux also increased, while the droplet size decreased. As the driving pressure was increased so were the heat transfer coefficient and the CHF.

Another parameter that must be taken into consideration is the distance from the heated surface to the nozzle orifice. Generally this distance is determined by the operating pressure and the cone angle for that pressure. Using simple trigonometry identities gives a separation distance so that the spray will cover the entire heated surface. Orientation of the heated surface is also of importance in terrestrial gravity, since the CHF is found to change when the surface is horizontal to when it is vertical. Chow states that the heat transfer coefficients do not change but the CHF does increase for vertically oriented surfaces.

Tilton (1989) shows that when a liquid spray is sub-cooled the heat flux increases as surfaces temperature increases, but as the surface temperature becomes greater than the saturation temperature of the fluid the amount of heat being rejected levels off.

Two spraying phenomena that need to be defined are flooding and splashing. Tilton gives a good explanation of the difference and importance of both. Flooding is when the spray flow rate is increased to the point that the droplets begin to agglomerate, causing the surface to become flooded. When the surface is flooded, heat is removed by both nucleation within the liquid film, as well as evaporation from the upper liquid/vapor interface. There are two possible reasons for splashing, one according to Tilton is that liquid can be expelled from the surface as bubbles burst, and two it could also be due to droplet entrainment by the escaping vapor.

Surface roughness is one more parameter that needs to be accounted for. The material used in this project was glass, which is a fairly smooth surface. Glass was used for optical reasons allowing one to look through the pedestal during operation to qualitatively see what types of heat transfer are occurring and how the spray is behaving. Chow et al. (1997) states that during boiling the surface characteristics play important roles in bubble nucleation. In general, rougher surfaces tend to generate better nucleate boiling at lower superheats. This is one disadvantage with the material chosen for the heater surface in the current project.

2.2 Convective Spray Cooling in Microgravity:

With a firm understanding of the parameters and physics of spray cooling one can see how it is appealing for microgravity conditions. According to Tilton (1989), one reason spray cooling may be ideal for spacecrafts is the lack of dependence on buoyancy forces for vapor removal and liquid supply. Many other types of high heat flux removal are less

suitable for spacecrafts systems because of the uncertainties concerning the effects of microgravity or transient body forces.

Dr. Kirk Yerkes and his research team at the Air Force Research Lab (AFRL) are working on a closed loop spray system to study the effects of thermal properties in a range of gravity of 0 to 1.8g. His team uses the NASA low-gravity KC-135 research aircraft for parabolic flight which gives the fluctuation in gravity needed for the experiment. Dr. Yerks has discovered that flow management is one of the main problems with spray cooling in a reduced gravity situation. He has determined that surface tension flow has dominated the fluid physics during the experiment under conditions of microgravity (Baysinger, et al., 2004). Figure 2.4 shows a picture of Dr. Yerkes experiment during testing on the KC-135 (Baysinger, 2004). It can be seen that the fluid is moving up through the cap and surrounding the nozzle. This evidence supports the conclusion that surface tension is a main contributor in sprays in microgravity conditions.

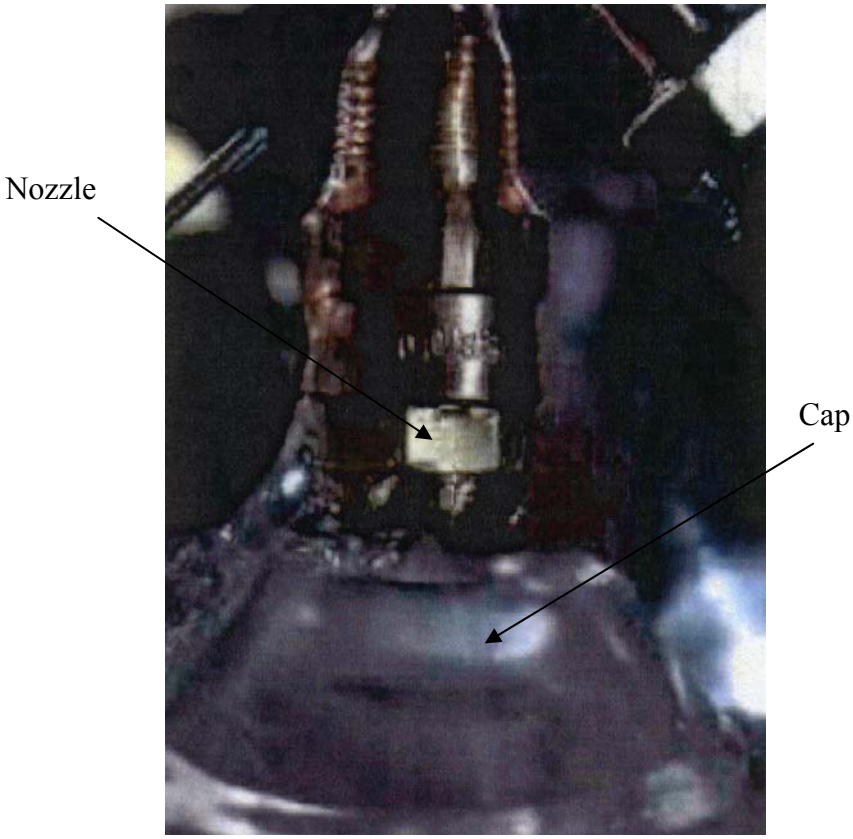

Figure 2.4: Spray Cooling During Microgravity Conditions (Baysinger, 2004)

Yoshida et al. (2001) performed a study of spray cooling under reduced gravity conditions and found that spray cooling was more effective in simulated microgravity than in terrestrial gravity. Yoshida et al. simulated low gravity conditions by rotating the apparatus 180 degrees changing the direction of the heated surface from 1g to –1g. Yoshida et al. (2001) data showed that the –1g heat flux was greater at every spray volume flux than the 1g data. These results indicate that spray cooling has potential for successful heat removal in microgravity conditions. Yoshida et al. not only used simulated microgravity on terrestrial gravity conditions, but also did some parabolic flight experiments. The data obtained from the parabolic flight experiment shows potential for spray cooling in reduced gravity as well as elevated gravity conditions when compared to terrestrial gravity.

Another experiment performed using spray cooling in microgravity was done by Kato et al. (1994). Kato et al. performed their experiment on the MU-300, which similar to the KC-135 performs a series of parabolas to simulate varying gravitational conditions. Kato et al. also used orientation to simulate microgravity conditions and found data that was comparable to that of Yoshida et al. Kato et al. also found that water gives a much high heat flux than a refrigerant (CFC-113) in microgravity as well as in terrestrial conditions. They also showed data illustrating the increase in the heat flux with the increase in spray volume flux.

2.3 Pool Boiling:

Pool Boiling uses the method of evaporative cooling to remove latent heat from heated surfaces and generally relies on buoyancy to carry vapor bubbles from the heater surface. Baysinger (2004) writes that pool boiling is expected to be inferior in microgravity, and in terrestrial gravity conditions, the orientation of the heated surface is very important. It has been seen that the CHF is reduced in microgravity due to the variation in bubble dynamics (Straub, 2001).

Straub also states that surprising results have been obtained for pool boiling in microgravity and claims that not only can saturated pool boiling exist in microgravity but also that smaller heater surfaces and low heat fluxes can produce an increase in higher heat transfer coefficients when compared to terrestrial gravity conditions. Straub indicates that the primary heat transfer mechanism must be strongly related to the development of the micro layer during bubble growth, both in microgravity as well as terrestrial gravity conditions.

There are secondary mechanisms that are responsible for the transport of enthalpy in the form of latent energy of the bubbles. It is already known that in terrestrial conditions that the external forces such as buoyancy cause transportation of enthalpy in the form of latent energy, but in microgravity Straub believes that it's the bubbles self dynamics that cause this transportation. The bubbles self-dynamics would include surface tension and Marangoni effects. Marangoni effects would be the behavior of the surface tension of bubbles as a function of the surface temperature. Straub has done exhaustive work in the this field to help engineers develop better understanding of how pool boiling can be used as a heat rejection process in microgravity.

Different experiments have been conducted to better understand bubble behavior in conditions of microgravity. Lee and Merte (1999) performed an experiment that used a 16mm camera to study the behavior of bubbles in microgravity. They used a refrigerant (CFC-113) as the working fluid and a semitransparent heat source to allow one to see the boiling process from the underside of the heater. Lee and Merte claim the experiment revealed a type convective bubble motion, which contributes to the steady effectiveness of the boiling heat transfer process in microgravity. The experiment shows a figure that compares the qualitative data between terrestrial conditions and microgravity. The surface tension mechanism with sub-cooling resulted in behaviors such as: bubble removal from the nucleation site, bubble migration along the heater surface toward larger bubbles, and bubble coalescence (Lee and Merte). As was the case for as spray cooling, Lee and Merte showed that sub-cooling increases the boiling heat transfer in microgravity.

2.4 Liquid Jet Impingement:

Impinging liquid jets have been demonstrated to be an effective tool in providing high mass or heat transfer rates in industries. The heat fluxes for impinging liquid jets typically exceed 10,000 W/m^2 (Wolf et al., 1993). Impinging liquid jets use convective and also sometimes evaporative (boiling) cooling as the heat reduction mechanisms. This shows the obvious advantage over pool boiling which is purely an evaporative cooling technique.

There are a variety of configurations for liquid jets. One configuration is a submerged jet where the fluid exits the nozzle or orifice into a body of the same fluid that is usually the same fluid as the jet itself. Another configuration is the free surface jet in which a liquid exits a nozzle or orifice into a gas environment (Webb and Ma, 1992).

Generally when jets strike a surface, thin hydrodynamic and thermal boundary layers form, originating from the stagnation region. After striking the target the liquid is then forced to turn and accelerate in a direction parallel to the surface. This flow is called a wall jet or parallel flow zone (Webb and Ma, 1992). Webb and Ma state that the thickness of the hydrodynamic and thermal boundary layers in the stagnation region may be of the order of tens of micrometers and that very high local heat or mass transfer coefficients exist.

A liquid jet can be broken into two different zones of impact, the stagnation and parallel flow zones. The stagnation zone often exhibits turbulent behavior that promotes mixing and an increase in heat transfer. The parallel flow zone cannot be determined to

have turbulent behavior and does not have a large heat transfer coefficient when compared to the stagnation region. Webb and Ma state that the peak heat transfer is confined to the stagnation zone and falls to a fraction of its maximum value just a few jet diameters from the stagnation point. Wolf et al. (1993) also state that there is little temperature fluctuation over a range of high heat fluxes in both the stagnation and parallel flow zone, but at low heat fluxes the temperature of the heated surface can vary up to as much as 40^{o}C.

Liquid jet impingement studies have been conducted in microgravity conditions. An experiment conducted by Labus (1977) determined the free surface shape of a jet impinging on an unheated flat disk where the viscous effects were shown to be negligible compared to surface tension and inertial forces. Labus's experiment yielded three distinct flow patterns, surface tension flow, transition flow, and inertial flow. A potential flow solution for the free surface shapes agreed well with the observed flow patterns.

When comparing a liquid jet to spray cooling there are some disadvantages that can be noted. Due to the impact created by the momentum, jets are considered to be an aggressive method of cooling and can be harmful to delicate devices or electronics. Jets also tend to have non-uniform surface temperature gradients at lower heat flux surface temperatures can vary widely, and thus do not cool the surface evenly. This non uniform surface temperature is due to the concentrated heat removal in the stagnation zone of the jet compared to the parallel zone.

2.5 Electro-hydrodynamics (EHD):

Electro-hydrodynamics (EHD) can be an instrumental tool for enhancing cooling in microgravity conditions. EHD has the capabilities of localizing a body force that can aid in removal of vapor bubbles, or in fluid management. Examples of factors that could make EHD attractive for mass or energy transport in microgravity are: rapid and smart control of enhancement can be achieved by varying the applied electric field, non-mechanical and simple design, suitable for special environments (space), applicability to single and multiphase flows, and minimal power consumption (Yagoobi and Bryan, 1999).

Yagoobi and Bryan show that the CHF can be increased in pool boiling with EHD for different heat transfer regimes. Figure 2.5 shows a general boiling curve verses an EHD enhanced boiling curve for various temperatures (Yagoobi and Byran, 1997). This enhancement is due to a localized body force that can aid in the removal of vapor bubbles. EHD doesn't only increase the heat transfer for water but also for refrigerants such as R-123, R-134a, and R-407C. This is useful for cooling of electrical devices, due to the dielectric properties of these refrigerants. The EHD forces can break up the vapor film patches that start to form in a boiling regime, thus delaying the CHF to higher wall superheats and heat fluxes (Yagoobi and Bryan, 1997).

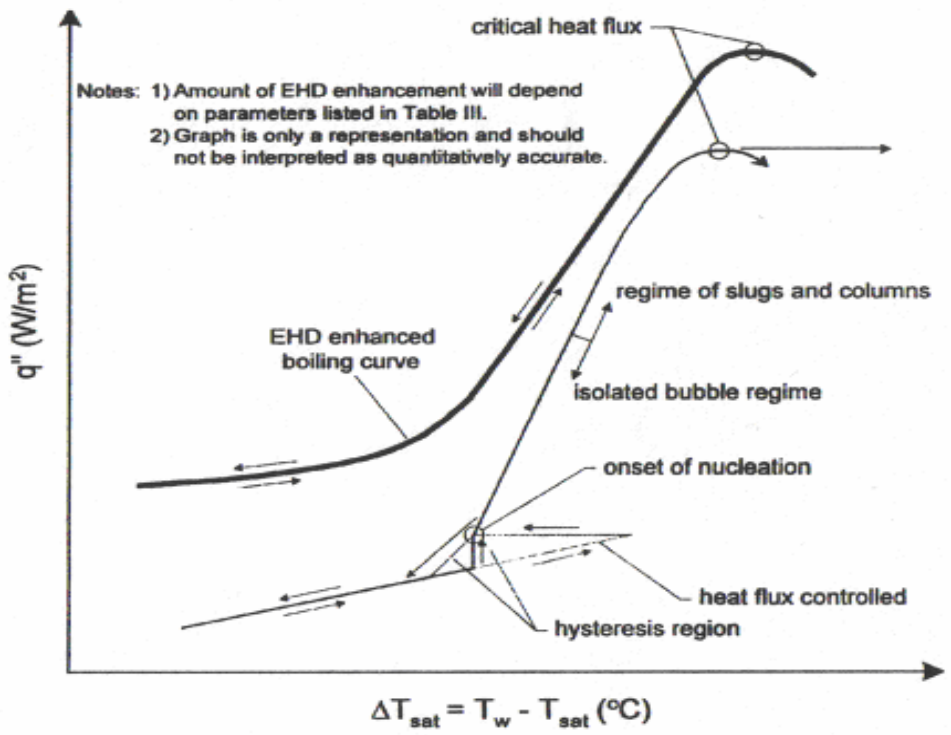

Figure 2.5: Enhancement of Electrohydrodynamic (EHD) for Pool Boiling Regimes (Yagoobi and Byran, 1997)

Yabe et al. (1987) show an increase in the CHF using R-113 of 20% at an uniform electric field strength of 20 kV/cm. Takahashi et al. (1997) also showed an increase in the CHF in R-123 with a trace of ethanol of 150% at a non uniform electric field strength of 40kV/cm. Jones (1978) states that when working with EHD that one must acknowledge the importance of electrostatic phenomena such as charge relaxation and electrohydrodynamic effects like surface wave coupling.

Appling EHD to spray cooling has been an issue that has been studied since the mid-sixties. Many agricultural companies are interested in applying EHD for crop spraying. Law (1978) studied different methods to produce a charged spray. These methods consisted of: ionized-field charging, contact charging, and electrostatic-induction charging. Constructing a cylindrical electrode and varying the combinations of

electrical potentials can produce all three particulate or droplet charging phenomena. Placing a charge on a spray for convective cooling is very similar to the agricultural applications as both processes are trying to enhance the amount of spray coverage and overall efficiency of the fluid management. Law uses the electrostatic-induction charging principle for the crop spraying application. This technique should also be investigated more thoroughly in the future research to determine its applicability for the present research experiment. Contact charging is another method mentioned by Law that shows promise, although it could be extremely dangerous if the entire apparatus was to become charged.

Generally, inductive charging can be accomplished at lower voltages compared to contact charging. Inductive charging is effective at voltages on the order of magnitude of 1-2 kV versus contact charging that often requires 10-20kV. All of these charging methods will need further evaluation before one method is selected as the best for the present experiment. The apparatus for the present work, as described in Chapter 3, has been fitted with electrical feed-throughs to permit the installation of electrodes to charge the spray, but the actual electrode design has not been accomplished in the present work. FC-72 can not be charged inductively due to its extremely high resistivity and a possible replacement dielectric liquid that may be applicable for inductive charging is HFE-7000. HFE-7000 has a much lower resistivity and can be inductively charged. FC-72 has the resistivity of 10^{13} Ωm which is high compared to HFE-7000 that has a value that is only 10^{6} Ωm. Another attractive quality of HFE-7000 is its dielectric constant of 7.4 where FC-72 has a value of only 1.75. The FC-72 and HFE-7000 was purchased from 3M.

CHAPTER 3 EXPERIMENTAL APPARATUS AND PROCEDURE:

In this chapter, both the experimental apparatus and operating procedure are described in detail. The apparatus is conceptually broken down into two different sections, the base package and spray chamber. This is because it is planned that the spray chamber will be used in subsequent microgravity flight tests, while the base has not been designed for use in flight experiments and will only be used in the WVU Spray Cooling Heat Transfer Laboratory.

Figure 3.1 shows the main components of the experiment. The nozzle produces a full cone spray with droplets that have the average diameter of 40 microns at 9.0 GPH of FC-72 (Baysinger et al., 2004). The cap is used for confinement reasons and will aid flow management in microgravity conditions. The cap fits onto the top of the sump after installation into the spray chamber (not shown). The sump is used to collect the liquid film after leaving the heated surface of the pedestal. The working fluid (FC-72) is pumped from the four outlets at the bottom of the sump (not shown in Figure 3.1) to a reservoir and then back to the spray chamber. There are two different pumps that are used to pump the refrigerant through the closed system. A flow loop schematic and a list of components are included for a further understanding of the plumbing. Figure 3.2 is a flow loop schematic to aid in the understanding how the experimental base operates. Section 3.1 will discuss the experimental apparatus in more detail. Section 3.2 will discuss the procedure and will include the ranges of experimental parameters for the testing conducted during this research. The section also contains an initial Turn-On and Operating Checklist.

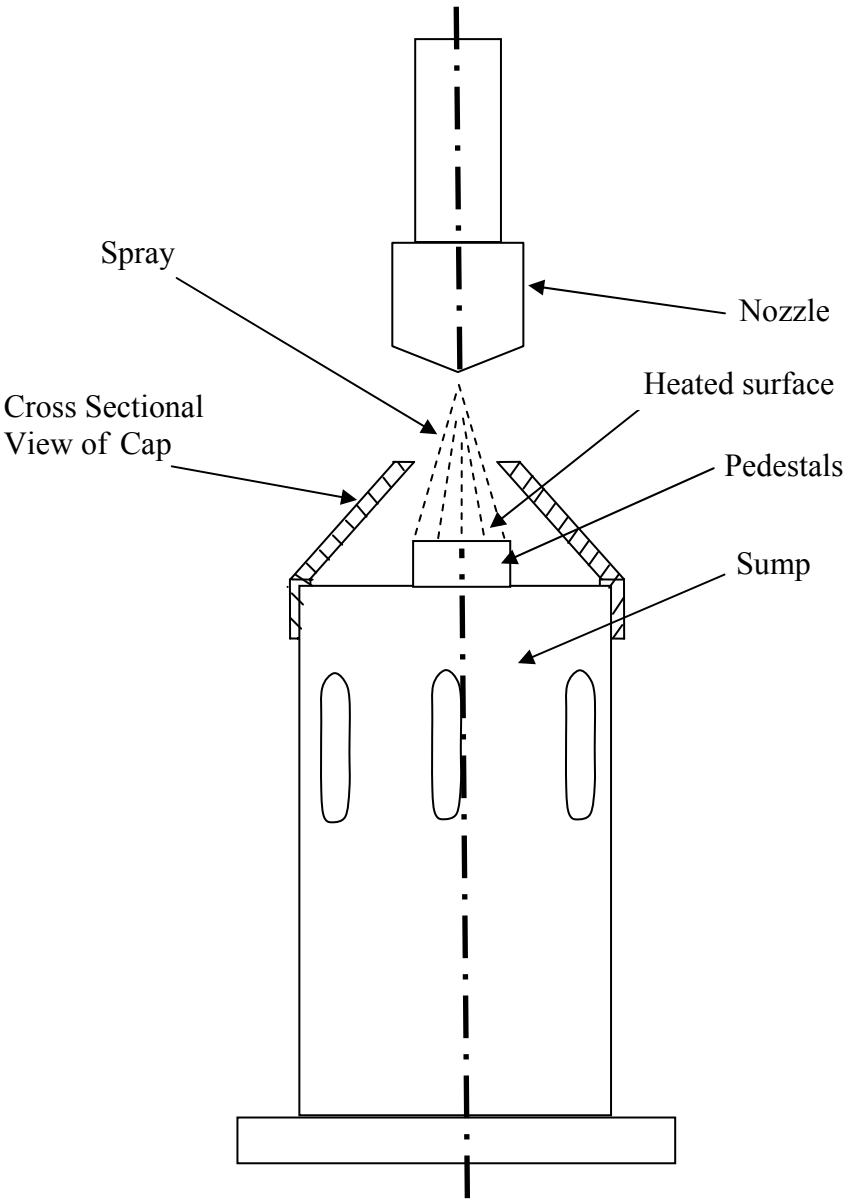

Figure 3.1: A Sketch of the Nozzle, Pedestal, Spray, Sump, and Cap

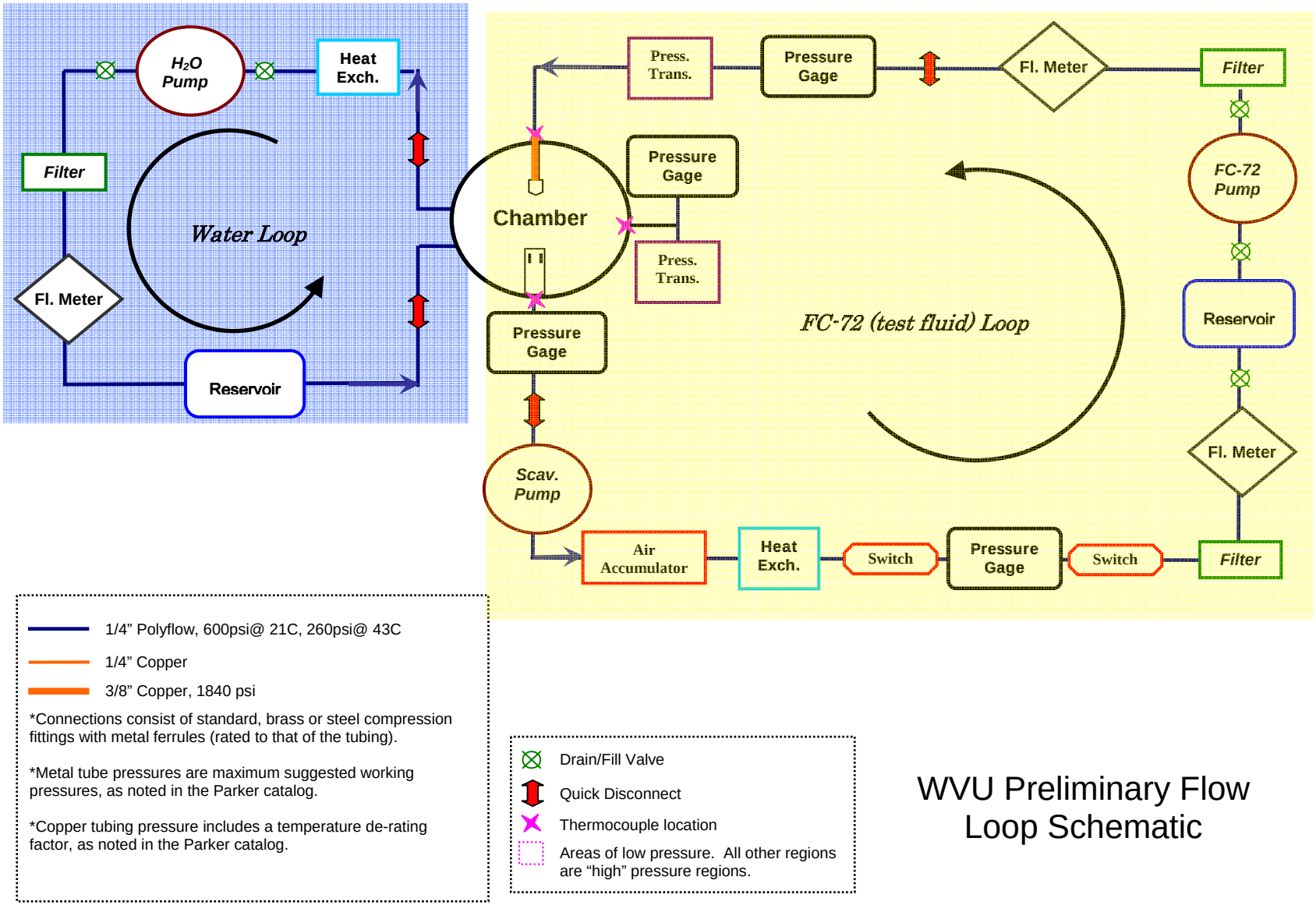

Figure 3.2: Flow Loop Schematic for Experimental Apparatus

3.1 Experimental Apparatus:

Experimental Base

The base was constructed to be a functional, but inexpensive, way to provide flow for the spray chamber. The frame of the base was welded together with 1 inch by 2 inch hollow rectangular aluminum tubing. Inside the base, there are two different closed flow loops. One is the water loop, and the other is the FC-72 refrigerant loop. Both flow loops are somewhat complicated, and thus a diagram is needed to show the plumbing for both loops. Figure 3.2 is a detailed flow loop schematic that shows each component in the loop. It can be seen that filters, flowmeters, pressure gauges and transducers are just some of the components that make up each flow loop. Each flow loop has at least one pump and one flowmeter. The FC-72 refrigerant flow loop contains two pumps. One pump is a Tuthill (D-series) magnetic driven gear pump, and the other is an Aquatec (DDP) diaphragm pump. The Tuthill pump can be controlled by its variable speed motor which allows the user to adjust the pressure and flow rate to the nozzle. The Aquatec runs at a constant rate with an override switch that turns the pump off when its back pressure exceeds 70 PSI. The Aquatec pump's main purpose is to drain the spray chamber and pump the FC-72 through the heat exchanger and back into the reservoir.

Filters have been used to keep the flow clean and reduce the chance of nozzle blockage. Pressure transducers have been installed in certain key locations where more accurate readings are required. Pressure gauges are also located in these locations to give the operator an idea of the level of pressures that are being applied at a glance. A list of parts can be seen in the Appendix titled "List of Parts."

Figure 3.3 shows an overview of the system including the base and spray chamber. The apparatus has been modified after the initial shakedown runs. Also seen are the three rotameters used to monitor the flow rates for the water, FC-72 nozzle pump, and the FC-72 sump pump. Two heat exchangers have been used. One removes heat from the water that cools the chamber, and the other aids in condensing the FC-72 for the refrigerant loop. It was noticed that the sump pump was pulling a two phase flow and an accumulator was added to separate the FC-72 vapor and air. An inexpensive vane pump was purchased from Grainger and is used to drive the water loop.

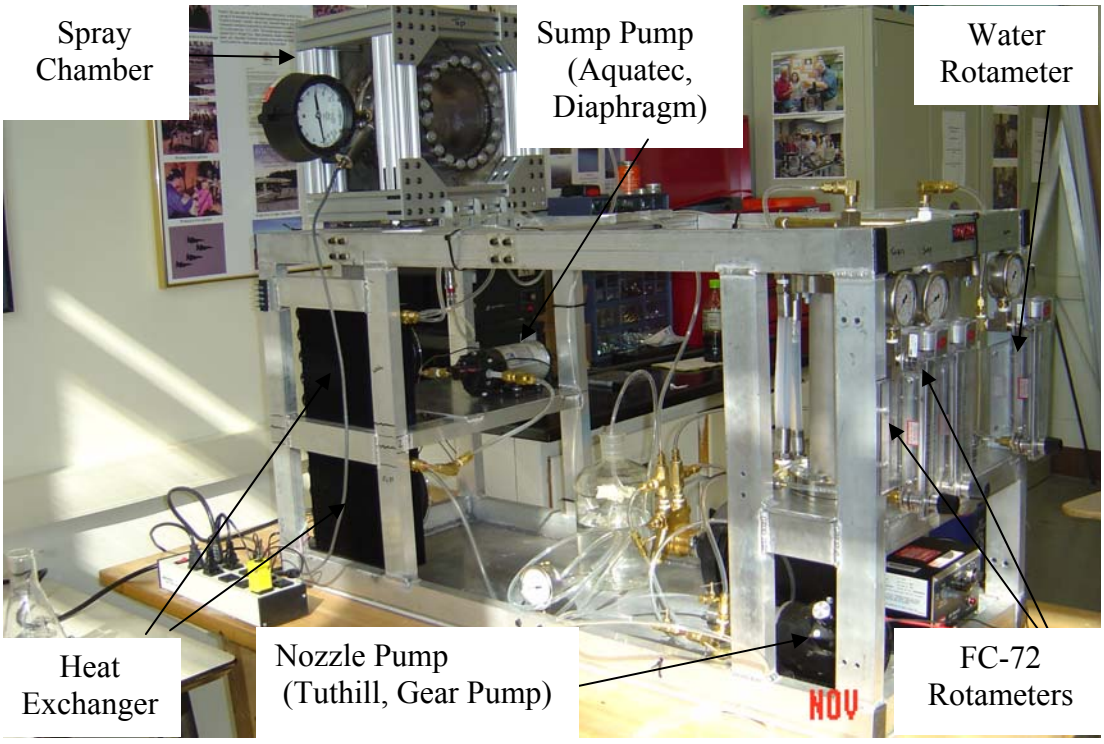

Figure 3.3: Overview of Experimental Apparatus

Figure 3.4 shows a more detailed photograph of an end view of the apparatus. The rotameters used were the basic variable area flow meter type (Dwyer, RMB-82-SSV) that are calibrated for standard conditions with the use of water. The two rotameters used in the FC-72 flow loop have to be corrected since the fluid is a refrigerant with density

different from water (approximate specific gravity = 1.7). Each rotameter has a pressure gauge located just after it in series. These pressure gauges are not for the correction of the flowmeters but to give the operator an idea of how much pressure is being produced by the pumps.

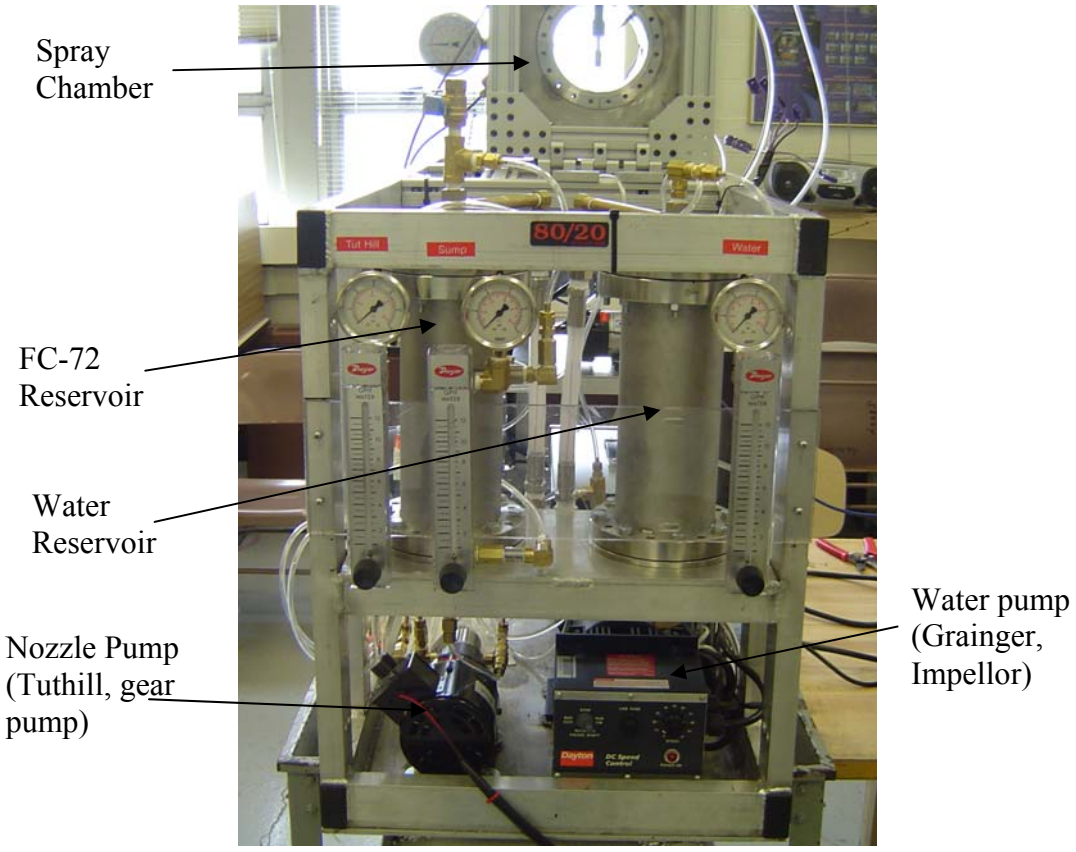

Figure 3.4: End View of the Apparatus

Figure 3.5 shows a photograph of the sump pump, accumulator, refrigerant heat exchanger (top), and water heat exchanger (bottom). The picture shows the flow loop just exiting the test cell. The sump pump (Scavenging Pump) is an Aquatec diaphragm pump that can handle a liquid-vapor flow mixture better than an impellor or gear pump. The accumulator was installed directly after the sump pump and before the heat exchanger. This was done to remove the FC-72 vapor and air before it entered the heat exchanger for better heat transfer, and to obtain a more accurate reading on the sump

pump rotameter. Also, a pressure gauge was installed just downstream of the sump to help determine the pressure at the sump outlet for boundary conditions needed to run a CFD model. The model is being created by CFDRC (Computational Fluid Dynamics Research Corporation) which is working closely with the AFRL. This pressure gauge can be replaced with an electronic transducer in the future if accuracy is an issue.

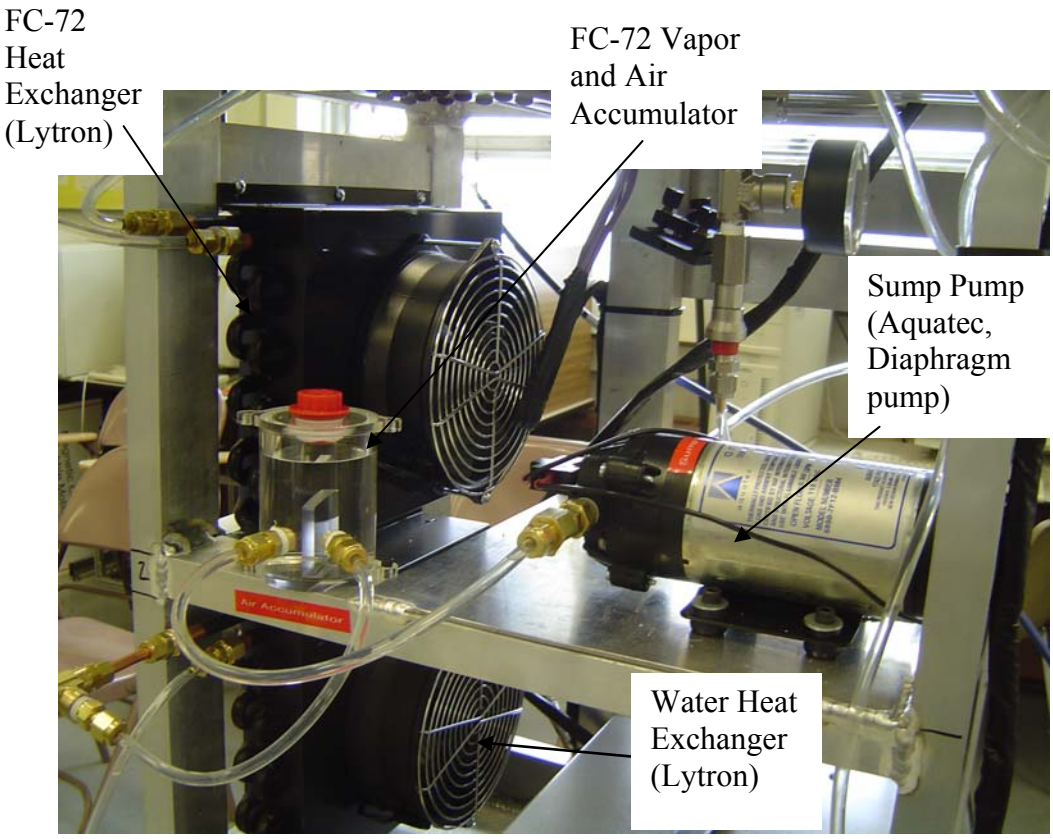

Figure 3.5: The Sump Pump, Accumulator, and Heat Exchanger

Experimental Test Chamber

80/20 Material:

The spray chamber was constructed using many different components in order to create a NASA approved chamber. The first component constructed was the frame that housed the chamber. Aluminum, 2 inch 80/20 rails were used due to their capability of

being put together and taken apart if the design needs were not optimally met. This material allowed for adjustments and offered adequate strength for the frame structure.

The frame was built using twelve 80/20 ten-inch long rails that were connected using special corner plates and angle connectors. Figure 3.6 shows the 80/20 rails before installation along with other various parts of the experimental apparatus. The 80/20 rails are called 20/20 rails which signifies the cross sectional dimensions, 2 inches by 2 inches. Figures 3.7 and 3.8 show different views of the angle connectors that are used for reinforcing joints of the frame. Figure 3.9 shows a picture of a corner joint plate which fasten to the 80/20 rails to create a stronger joint. With the combination of corner plates and angle connectors, the joints created with 80/20 material had adequate strength as will be seen later in this section. Each plate and connector was fastened to a rail using a special 80/20 fastener and ¼-20 screws. Figure 3.10 is a picture of the screws and special fasteners that were used in construction of the 80/20 frame. These fasteners are designed to slide into a slot inside the rails allowing them to be positioned virtually anywhere along the rail. Once the correct position is found and the screws are tightened, the fasteners become tight and the joint becomes immobile.

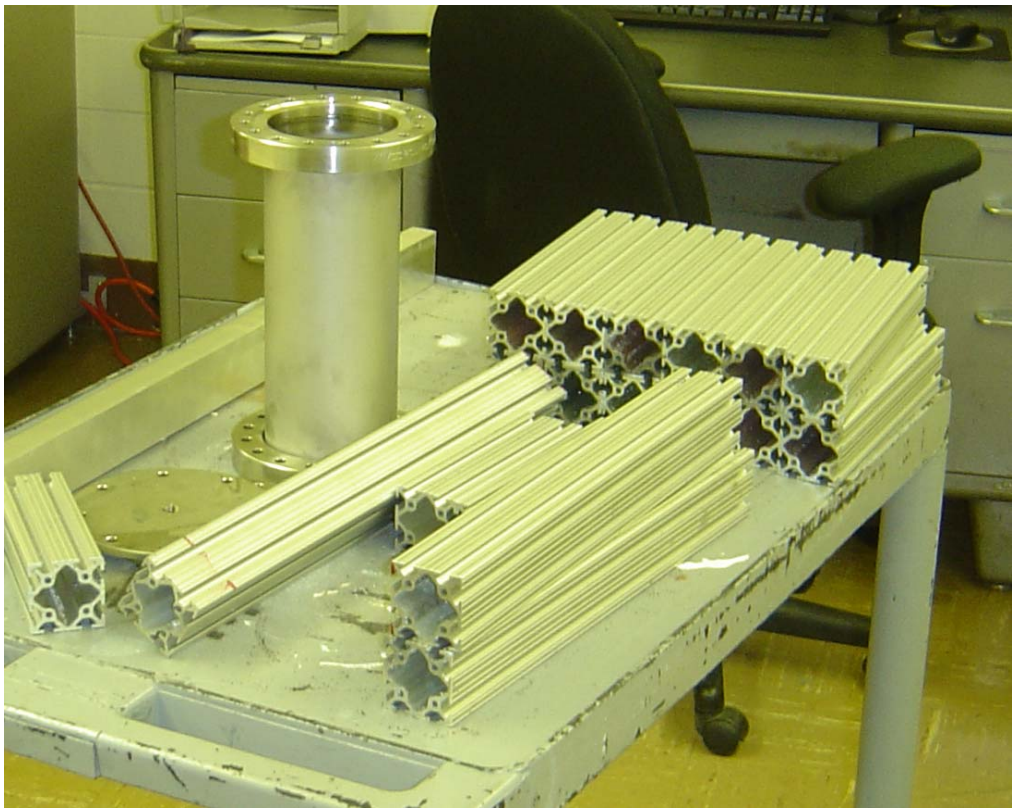

Figure 3.6: 80/20 Pre-cut Rails for Construction of the Spray Chamber Frame and Miscellaneous Parts

Figure 3.7: Top View of an 80/20 Angle Connectors for the Construction of Joints

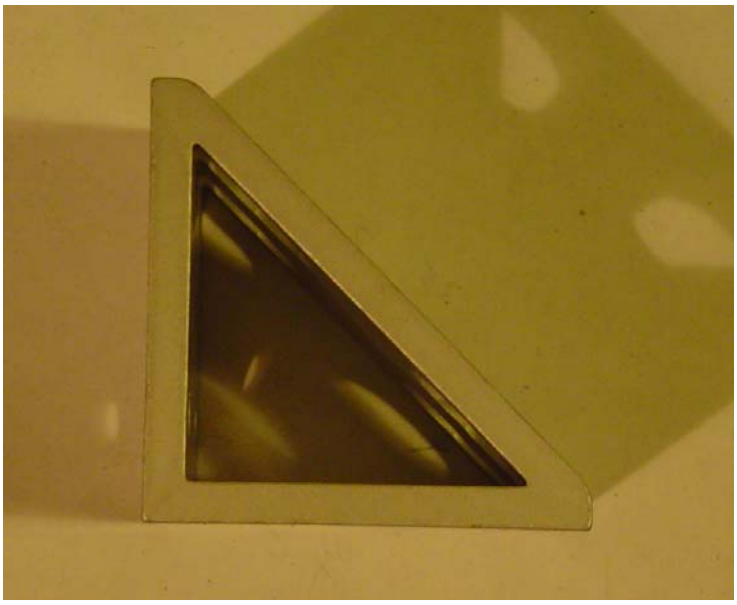

Figure 3.8: Side View of an 80/20 Angle Connector for Joining of Two Rail Pieces

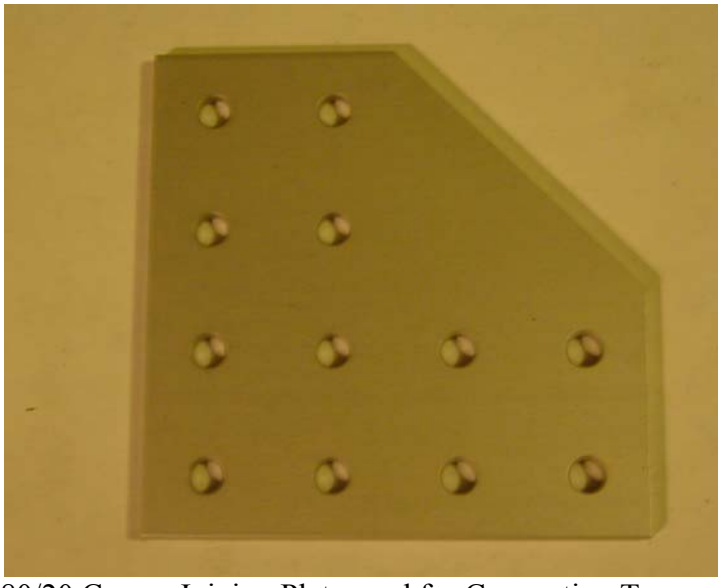

Figure 3.9: 80/20 Corner Joining Plate used for Connecting Two or Three Rails (depending on joint specifications)

Figure 3.10: Special 80/20 Fasteners and Screws for Construction of the Chamber Frame

Tests were conducted using a WVU Civil and Environmental Engineering Department 4000 pound load limit frame, hydraulic ram, and load cell to apply and measure the load, and a 2 inch LVDT to measure the displacement. Load and displacement data were recorded versus time using a PC based data acquisition system. A corner and tee joint were tested to see exactly how much deflection and load the 80/20 joints could handle. Figure 3.11 shows a load being applied with intervals of five minutes between increases in load. The total load used was approximately 550 lbs. Although the joint did not fail, a large amount of deflection was observed.

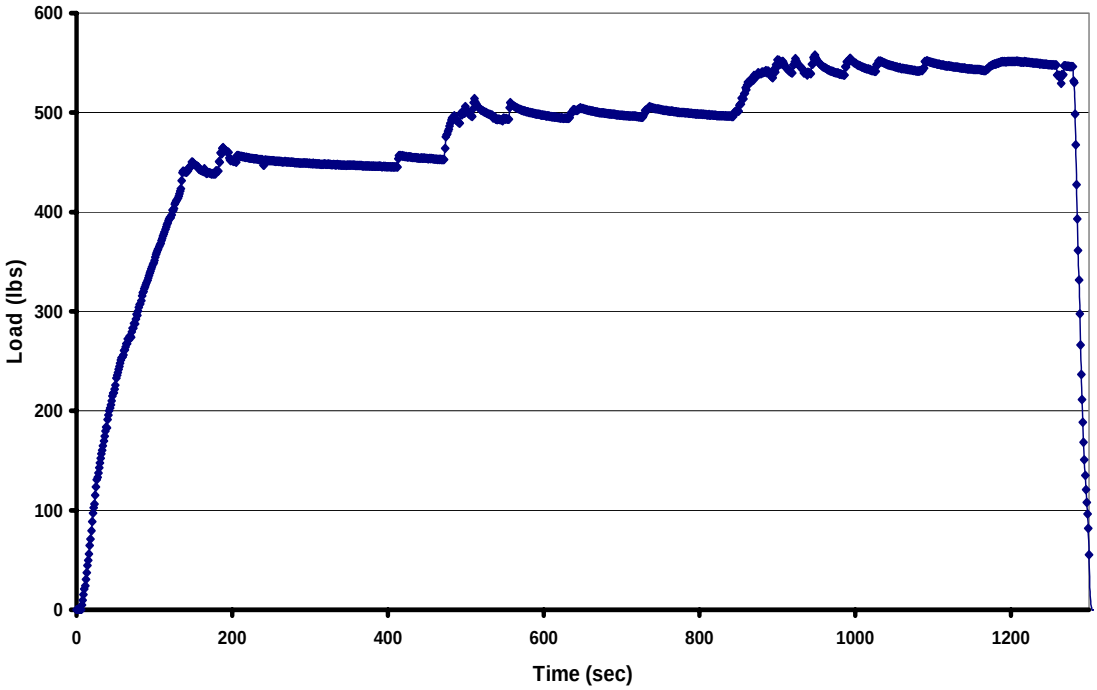

Figure 3.11: Load as a Function of Time on an 80/20 Corner Joint

Figure 3.12 shows the deflections of the rail during the test to illustrate the amount of movement that can occur during loading. The LVDT had a range of only 2 inches and the test produced a deflection greater than that range. Therefore a tape measure had to be used to obtain meaningful measurements of larger deflection.

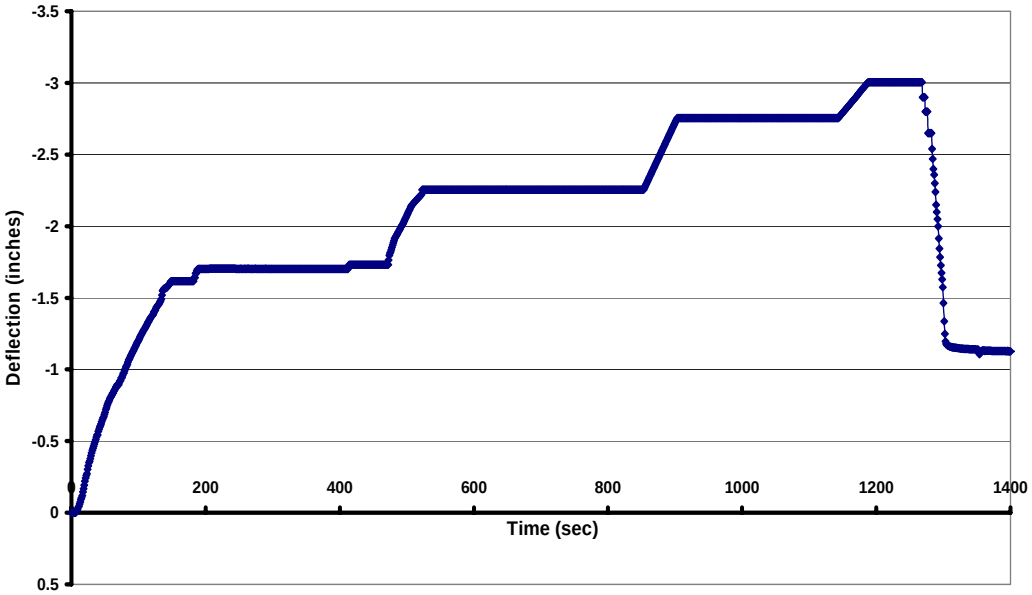

Figure 3.12: Deflection Versus Time for Corner Section: Test on June 7, 2004 (Note: Deflections < 2" measured via LVDT, deflections > 2" measured via tape measure)

Figure 3.13 shows a photograph of the deflection that was produced by the largest load applied to the corner joint during the test. A hydraulic jack was used to apply the load at the distance of 21 inches from the joint, and it was noted that the jack had to be continuously pumped to keep the load at somewhat steady state. The maximum applied moment about the end of the cantilevered 20/20 section corresponding to the maximum applied load of 550 lbs was 12,650 in-lbs. Similar tests were conducted for a "tee" joint.

Figure 3.13: Picture Taken at Maximum Applied Load on an 80/20 Corner Joint

Spray Chamber:

With the frame being completed, the actual spray chamber had to be connected to the 80/20 frame. Two ¼ inch stainless steel plates were fabricated using a CNC plasma torch at Wilson Works Inc. for joining the chamber and the 80/20 rails. Figure 3.14 shows a CAD drawing in Solidworks that was created for the construction of the stainless steel plates. The spray chamber was attached to the stainless steel plates by welding every 45^{o} around the circumference. Figure 3.15 allows one to see how the stainless steel joining plates are designed to house the spray chamber. The figure also illustrates that the spray chamber and frame are hinged to allow rotation for horizontal spray conditions. The rotation allows the orientation of the heated surface to be altered.

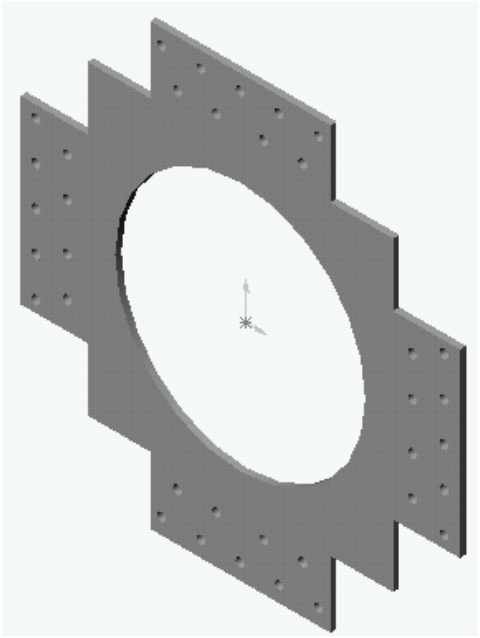

Figure 3.14: A Solidworks Drawing to Help in Designing the Spray Chamber (Picture Courtesy of Mr. Travis Michalak of the AFRL)

Figure 3.15: Preliminary Stages in Construction of the Frame of the Spray Chamber

The spray chamber was a special-order part from MDC Vacuum Products Corp. (The spray chamber is identical to one used by AFRL except the top port inner diameter is 2.5 inches instead of 1.5 inches.) The larger port was chosen to give more options for installation of the high voltage feed-through. The chamber was a cross with two optical ports that measured approximately 5.97 in inner diameter, a top port that was 2.5 in inner diameter, and a bottom port that was 1.5 in inner diameter. Figure 3.16 shows the chamber before it was joined to the stainless steel housing plates.

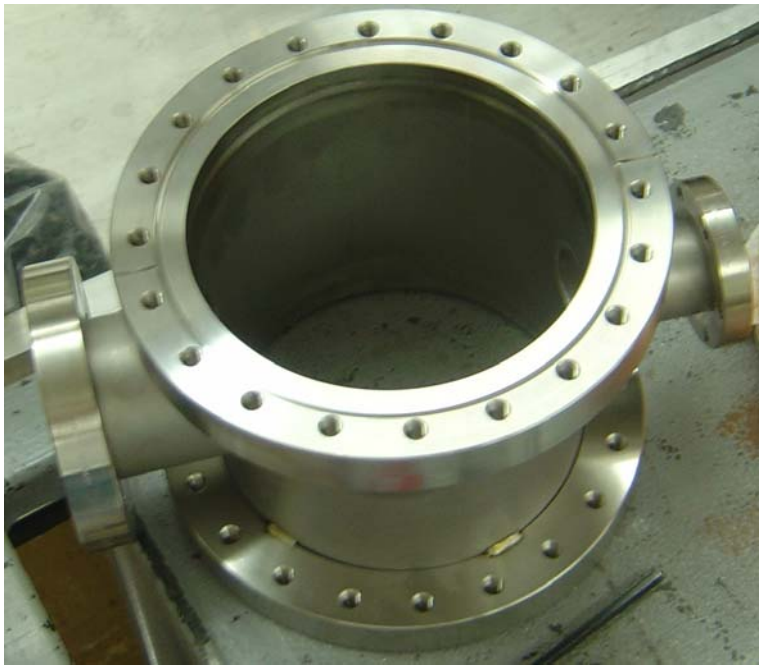

Figure 3.16: The Spray Chamber Before Any Fabrication or Alterations

There were many different alterations that were done before the spray chamber could be joined to the stainless steel plates. Thermocouple, high voltage, and pressure transducer feed-throughs were installed. An in-house technician (Mr. Cliff Judy) welded all three stainless steel feed-through bulkheads at specified locations. The high voltage and thermocouple feed-throughs were at 45^{o} angles from the inlet of nozzle or sump depending on orientation, and the pressure feed-through is along the center line. Type E

thermocouples (Chromega-Constantan) have been used because the spray chamber must be able to interchange with the NASA certified base at AFRL for future use in microgravity flights.

The view ports were machined from Polycarbonate Hygard Laminate BR100. The material is also called bullet proof lexan and was purchased from AIN Plastics. The view ports had to be able to resist large amount of impact in order to meet the safety requirements for microgravity testing.

After the installation of the various feed-throughs, the chamber was then wrapped with copper tubing for convective water cooling of the spray chamber. The copper tubing was attached to the stainless steel chamber using thermal conductive epoxy (Master Bond, EP21ANHT). Figure 3.17 shows a side view of the test cell with the feed-through fittings at the 45^{o} angles and the joining of the copper tubing to the chamber. It can be seen that a generous amount of the thermal conductive epoxy was used. EP21ANHT epoxy has roughly the same thermal conductive coefficient as the stainless steel. Quick disconnects have also been used to make removal of the chamber easier and less time consuming.

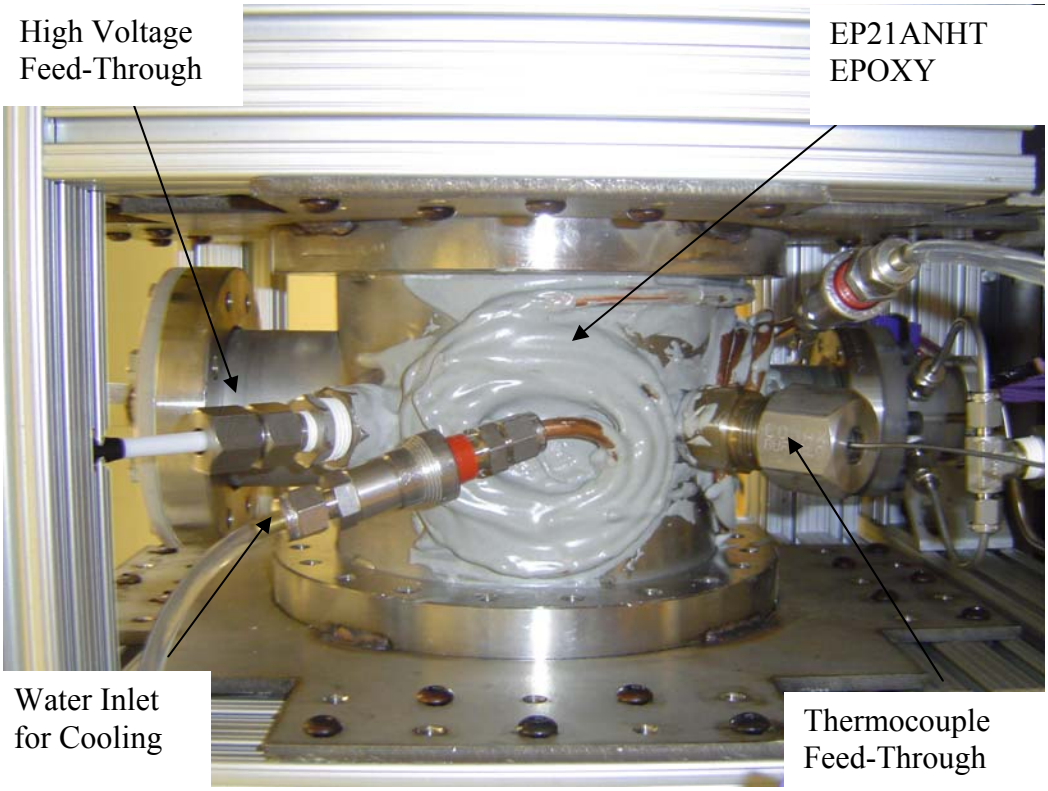

Figure 3.17: Side View of the Spray Chamber

Thermocouples and Location:

As stated before, type E thermocouples have been used for compatibility reasons with the Air Force Research Laboratories experimental test apparatus. There are fifteen different thermocouple locations in the spray chamber. Each thermocouple was calibrated using a temperature controlled, Fisher Scientific bath and mercury thermometer with 0.1 ^{o}C graduations. Figure 3.18 shows a typical calibration curve for one of the thermocouples. Appendix A contains the calibration curves and equations for all thermocouples that may be used in the experiment.

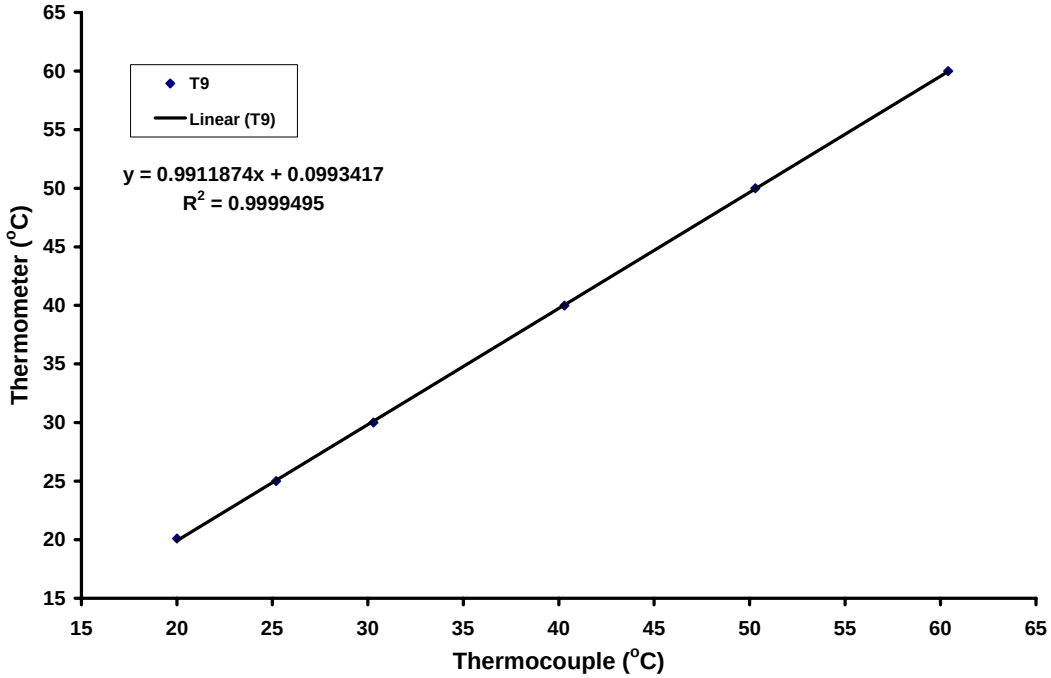

Figure 3.18: Thermocouple X_1 Calibration Curve With Calibration Equation and R^2 Number

The pedestal has seven different thermocouple locations to allow the computation of the conduction heat loss down the pedestal. These locations will be discussed in a later section. The spray chamber has six thermocouple locations. Figure 3.19 shows the locations of the six thermocouples in the chamber. These thermocouple locations have been selected to help in understanding the fluid thermal behavior inside of the chamber. Also, the thermocouple locations were selected to match those used in the AFRL apparatus as nearly as possible. One additional thermocouple was located just upstream of the nozzle to give the temperature of the fluid before impacting the heated surface.

T_8	Wall temp.
T_9	Nozzle vapor temp.
T_{10}	Inside sump temp.
T_{11}	Pedestal spray temp.
T_{12}	Outside sump temp.
T_{13}	Up near HV feed through
T_{14}	Fluid entering the nozzle

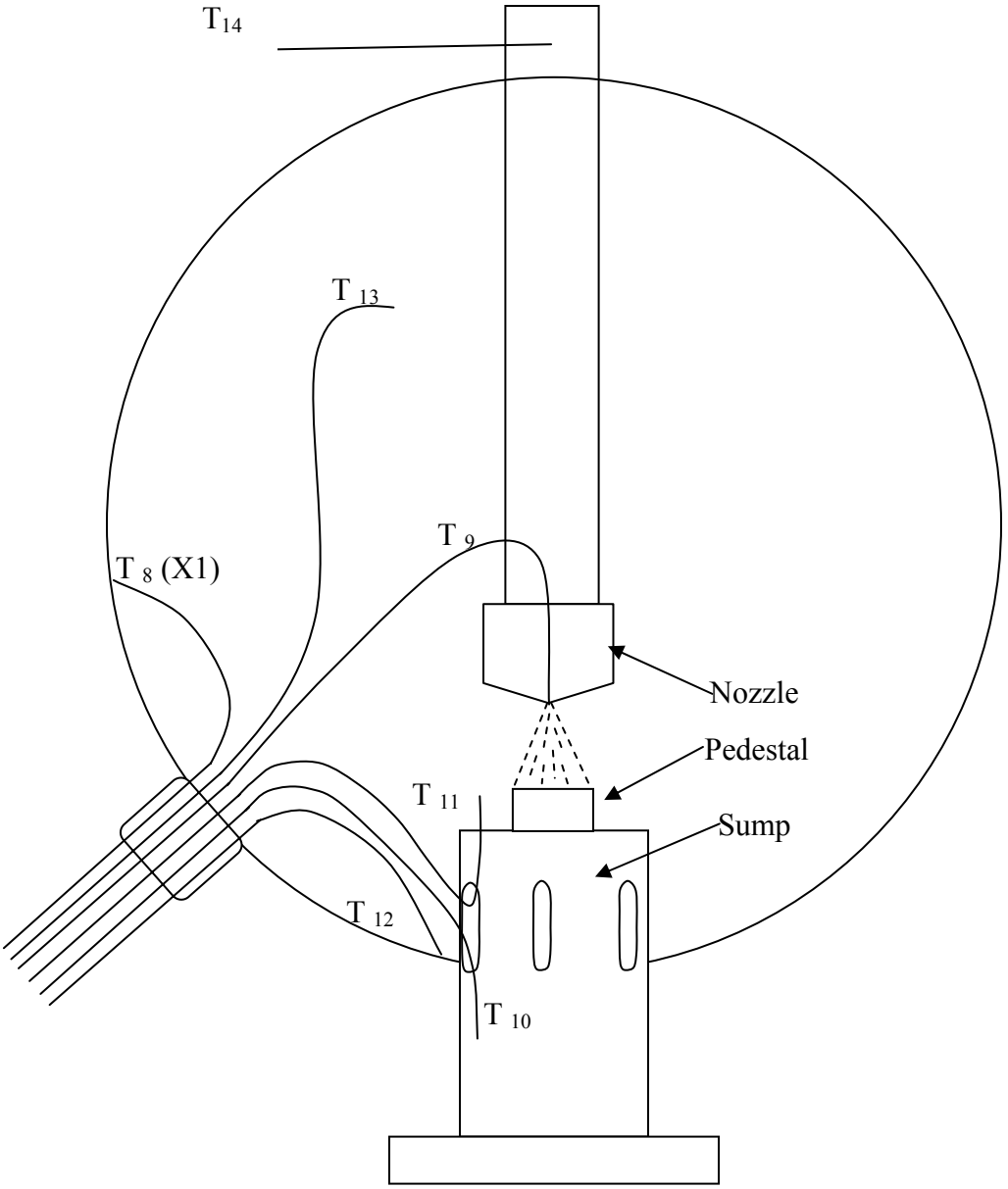

Figure 3.19: Thermocouple Locations Inside of the Spray Chamber

Nozzle:

The nozzle feed-through was constructed from various fittings and a Spraying Systems FullJet 1 (full cone) nozzle. The FullJet 1 is a pressure atomizing spray nozzle with a capacity of 1. Spraying Systems refer to capacity as a measurement of flow rate at a certain pressure. The FullJet 1 with a capacity of 1 will run at 1 GPH with a pressure of 10 PSIG. It can be run at fairly low flow rates and has operated at flow rates between 4.6 GPH and 9.3 GPH. Figure 3.20 shows a photograph of the nozzle, pedestal, sump, and high voltage feed-through. Teflon fittings were used as half of the plumbing inside of the chamber because of the planned use of EHD (Electro-hydrodynamics) during future experiments. Copper tubing was used and had to be covered with heat shrink wrap to prevent electrical arcing to the electrode. Copper tubing was used because of the ability to flex the nozzle into the correct position over the center of the heated surface (pedestal).

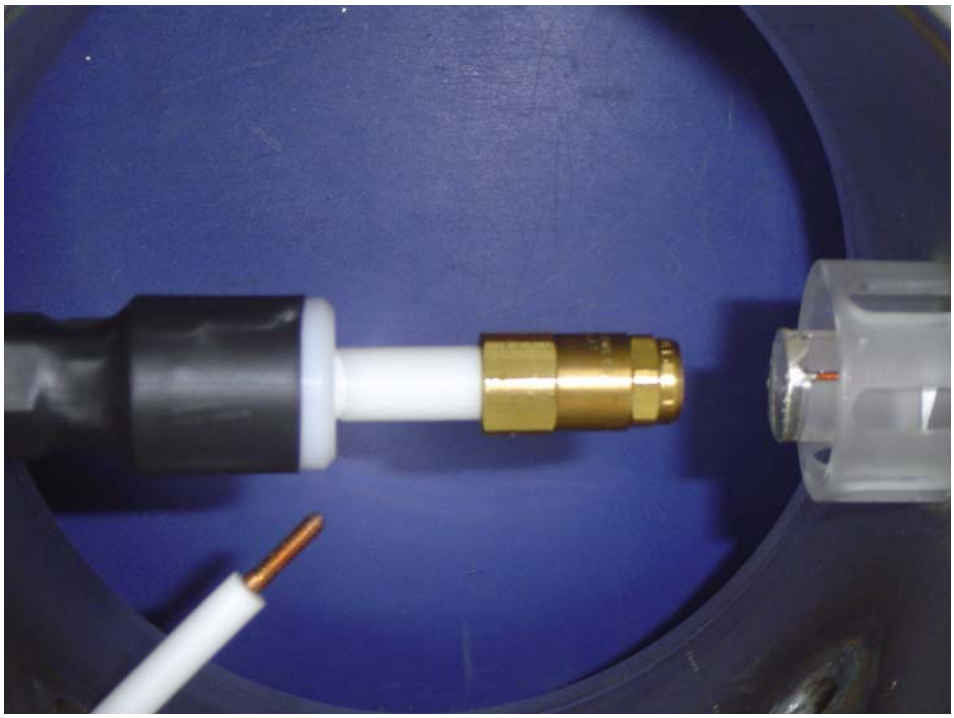

Figure 3.20: Nozzle Plumbing Position Approximately 13 mm from Heated Surface

Upstream of the nozzle, a pressure gauge and transducer were installed. The pressure gauge is for a quick reading and is used to adjust the pump. The pressure transducer will give a more accurate measurement and will be used for future data collection. In the bottom of Figure 3.20, one can see a possible design under consideration for the high voltage feed-through. There could be changes with the high voltage feed-through as more work is being done to determine the best configuration. This was one of the reasons for making the port that now houses the nozzle entrance larger in diameter (2.5 inches) than the sump port (1.5 inches).

Sump, Cap, and Pedestal:

The sump was constructed at the Devall Brothers Inc. machine shop. The sump was designed to insert into the smallest port of the spray chamber. The sump was designed to protrude into the chamber and to house the heated pedestal. Figure 3.21 shows a Solidworks CAD drawing of the assembly of the sump, pedestal, and clamp. This design is identical to that used by the AFRL. The pedestal is designed to protrude past the sump 0.2 inches. The pedestal was constructed to have a thin heating element at the top of the pedestal surface. The pedestal design will be covered more thoroughly in a later section. The clamp is used to seal the pedestal inside of the sump and to ensure a leak-free seal. The pedestal is sealed using O-rings and compression to create a leak-free system that can withstand pressures exceeding 150 PSI. Figure 3.22 shows the final setup of the sump with the drain plumbing connected. Quick-disconnects were again used in order to allow one to change a sump out in a timely manner.

The slots in the top of the sump were created to help in the draining process of the liquid spray that escapes from the cap or when unconfined flows are being studied. The slots protrude into the chamber and allow the liquid in the chamber to reenter the sump. Figure 3.23 shows the sump and pedestal inserted into the chamber and how the slots extend past the top of the port.

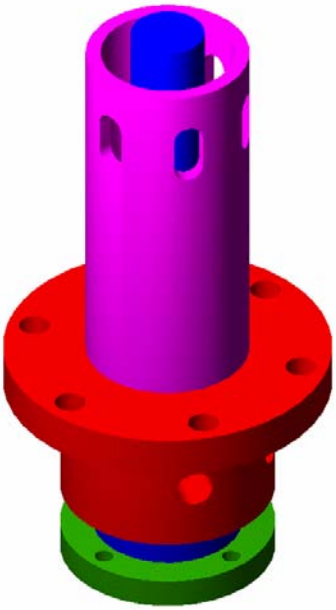

Figure 3.21: A Solidworks CAD Drawing of the Sump, Pedestal, and Clamp
(Drawing Courtesy of Mr. Travis Michalak of the AFRL)

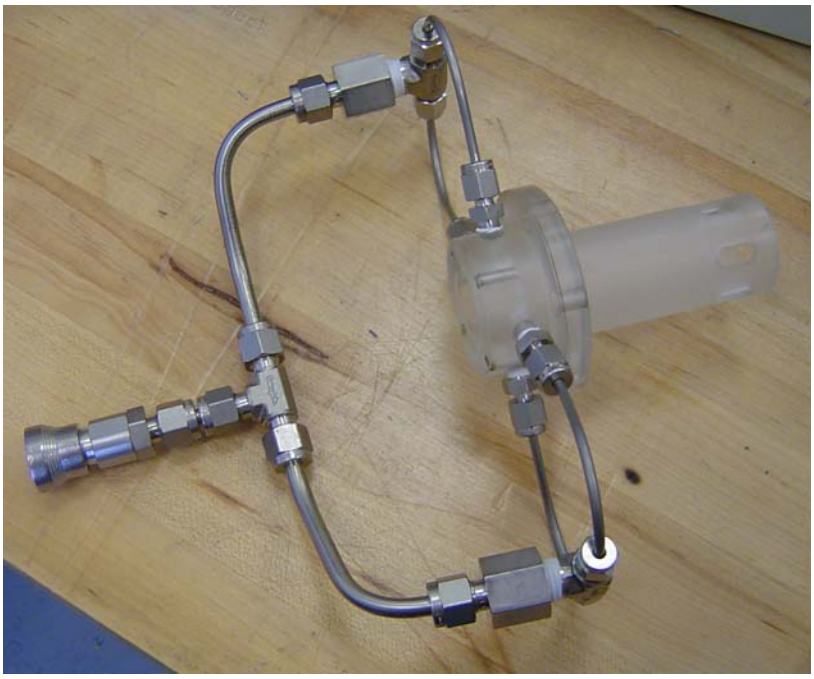

Figure 3.22: The Sump Before Insertion into the Spray Chamber

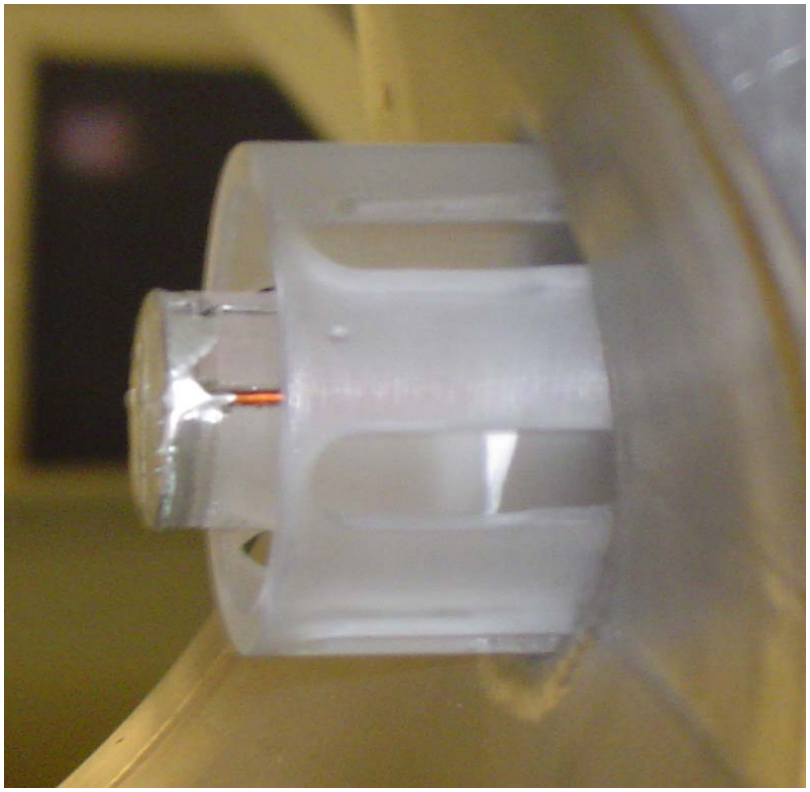

Figure 3.23: Sump Inserted into the Spray Chamber with Pedestal, without a Cap Installed

The caps are used to confine the flow and direct it down the sump. The caps are more critical for microgravity conditions but should also be studied to find the best geometry that yields both the highest heat transfer and optimal flow management. Four caps were machined at Devall Brothers using different inside curvatures (Figure 3.24). A quarter was used in the photograph of Figure 3.24 for scale. The fluid's entrance to the cap is approximately 0.25 inches in diameter and should be no more than 0.25 inches away from the nozzle. Each cap has a nylon set screw to fix the cap to the end of the sump. Two caps and the unconfined (no cap) configuration have been tested to see if there is a significant difference in heat transfer, CHF, or gross flow behavior. The two caps that were studied have different inside slopes, with the straight cap having a straight angle from the top of the sump to the entrance of the cap. The cap with a straight slope has an inside surface that is closer to the heated surface and may not allow the fluid flow to escape properly. This cap may cause some of the splashing to rebound back onto the heated surface. The cap with a curved inside geometry could allow for better flow management.

Figure 3.24: Various Caps (Note Quarter in Center of Photograph)

Figure 3.25 shows a CAD drawing of the straight cap, and one can see how there might be some recirculation or rebound of fluid with higher flow rates. This cap geometry is identical to that used by the AFRL. Figure 3.26 shows a sketch of the two different caps used. The unconfined flow case is the spray impinging on the pedestal without the presence of either cap.

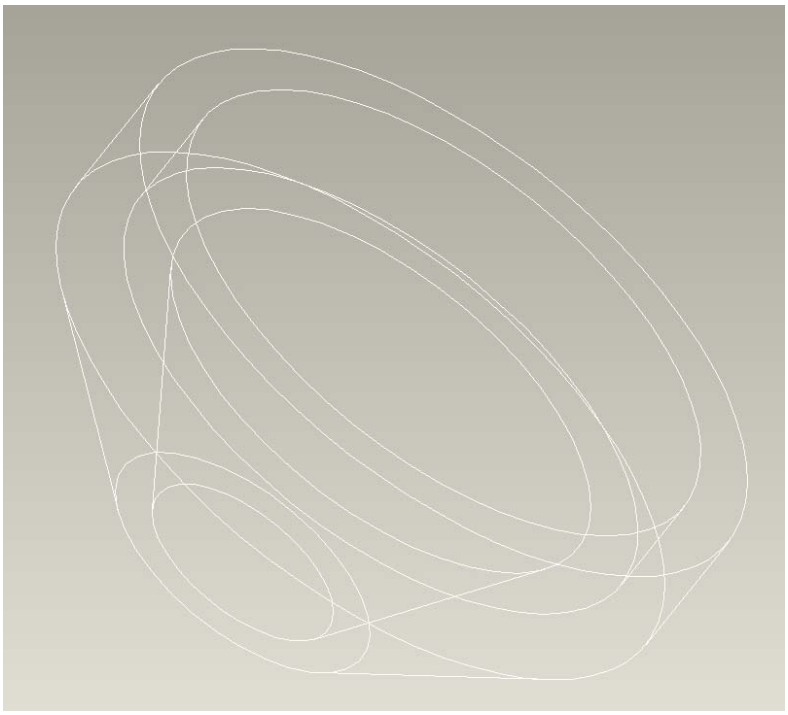

Figure 3.25: CAD Drawing of a Straight Cap
(Drawing Courtesy of Mr. Travis Michalak of the AFRL)

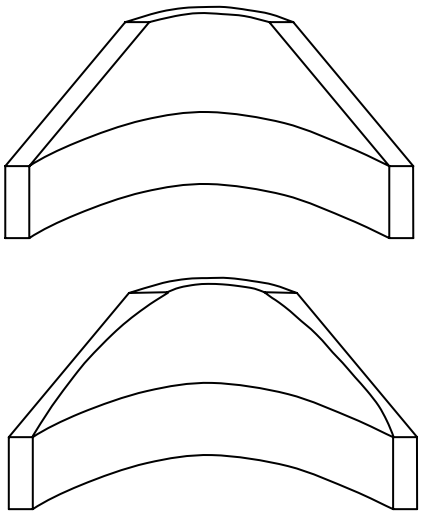

Figure 3.26: Sketch of the Straight and Curved Caps Used for the Confinement Study.

The pedestal is made of glass (Corning AMLCD 1737) and can be said to be very fragile. Its construction is very tedious. Figure 3.27 shows the pedestal geometry with the heights and diameters of the components. The pedestal pieces were machined using

diamond tipped bur tools and cutting wheels, under direction from Mr. Richard Harris at AFRL. Two thin slices were removed from the top, and grooves were machined into the thin slices to allow installation of thermocouples in certain locations. Each slice was approximately 1 mm or 0.040 inch thick, and after thermocouples were inserted into the grooves, optical cement was used to fuse the glass back together. Optical cement (Summers SK-9) was used to allow visibility from the bottom of the pedestal. After assembly of the thermocouples and electrodes for the heater was completed, a glass disk that had been drilled for feed-throughs was glued onto the back of the pedestal. The glass disk allowed there to be a seal between the pedestal and the sump using a compression O-ring seal. Again, this pedestal is the same as the AFRL pedestals.

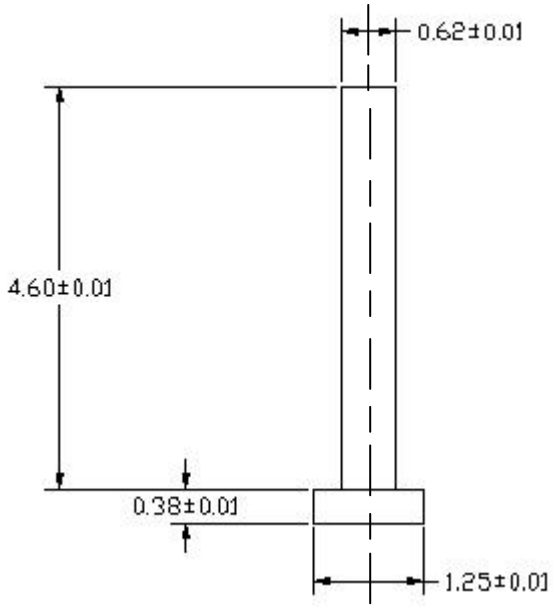

Figure 3.27: Drawing of the Glass Pedestal for Construction with Dimensions in Inches (Drawing Courtesy of Mr. Richard Harris of the AFRL)

Figure 3.28 shows a drawing of the thermocouple locations for the pedestal. An ITO (indium-tin oxide) heater was also glued onto the top surface of the glass pedestal and was connected to the electrodes using electro conductive epoxy (H2OE). One

pedestal was constructed with a ceramic or TFR (thick film resister) heater because it is not as fragile as the ITO heaters and was expected to be able to create higher heat fluxes without damage. The drawback to the TFR heater is that it is not transparent, and thus flow visualization through the pedestal is not possible.

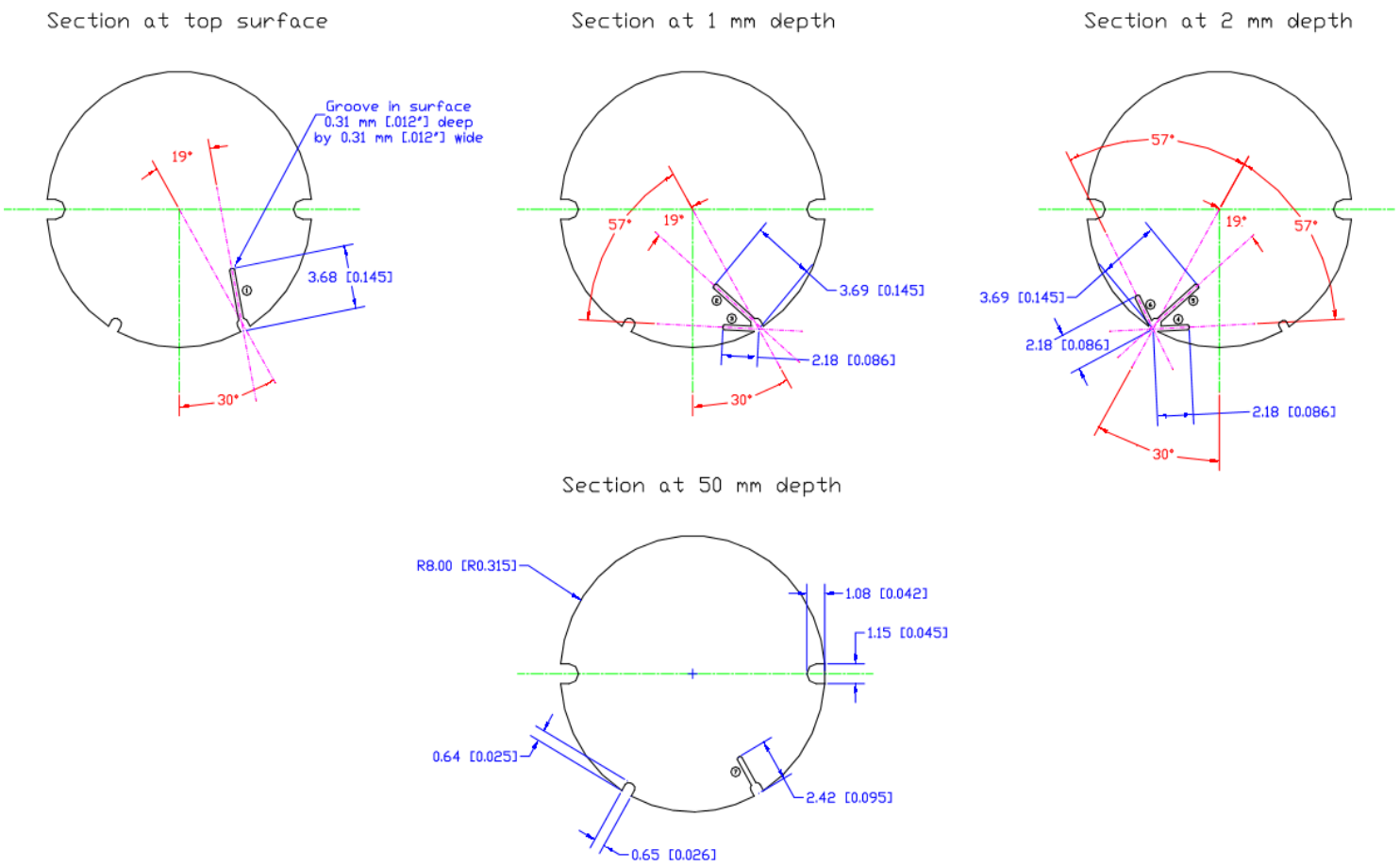

Figure 3.28: Thermocouple Locations inside the Pedestal
(Drawing Courtesy of Mr. Richard Harris of the AFRL)

Figure 3.29 shows pedestal components (ITO heater, two thin slices of glass, the glass rod, and the glass disk) prior to assembly. The ITO and TFR heaters have different thicknesses and could cause a slightly different reading for thermocouple one. The ITO and TFR have thicknesses of 0.020 and 0.025 inches respectively. The scale of the pedestal can also be seen in Figure 3.29.

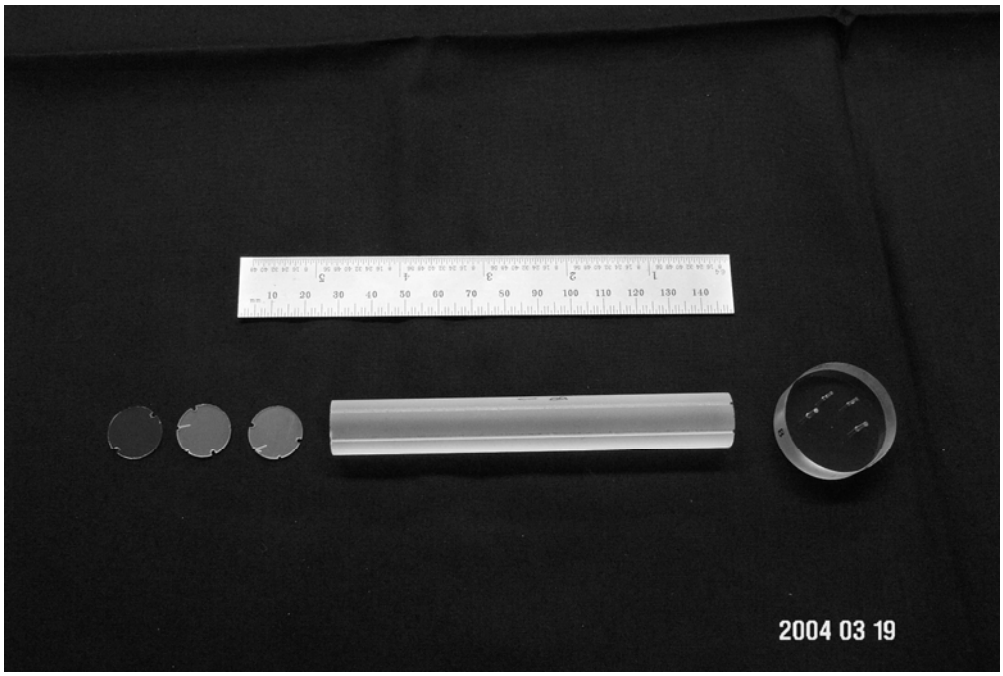

Figure 3.29: Pedestal Components Before Assembly (Baysinger,2004)

3.2 Procedure:

The apparatus can be run by one individual, but it is much more easily operated with two people. A definite procedure needs to be followed when starting the apparatus. The first step in the procedure is to follow the Turn-On Checklist given in Table 3.1. It is easy to forget to properly open or close one or more valves which will not allow the system to run properly. After the Turn-On Checklist is completed, all components may

be started safely. Now that the system is running, the Operating Procedure Checklist in Table 3.2 should be followed. One will have to adjust the accumulator and nozzle pump (Tuthill) to remove the unwanted FC-72 vapor and air from the system, and to achieve a steady chamber pressure. With the removal of air and FC-72 vapor, the rotameters should be accurate and set to the desired flow rate. The water rotameter should always be set at 12 GPH for effective cooling. With both the nozzle and sump pumps driving the FC-72 at the same flow rate, the spray chamber should be adjusted to the correct orientation. The spray chamber can rotate 90 degrees for horizontal spray tests. With the adjustments made to the spray chamber, the pedestal's heater power supply then needs to be adjusted to the correct power from 10 W to 70 W during a test where the flow rate will remain constant. Once the desired power is obtained, the steady state pressures and temperatures should be recorded. Data at four different flow rates varying from 9.3 GPH to 4.6 GPH with three different geometries were recorded in the present work. Tests have been conducted with both vertical downward and horizontal spray conditions. At each flow rate, the heater power was varied from 10 W to 70 W in increments of 10 W. Note that at the lower flow rates such as 4.6 GPH, the higher power settings cannot be used for fear of damaging the pedestals. To prevent damage to the pedestal heaters, the ceramic heater and ITO heater temperatures should not go above $75^{o}C$ and $55^{o}C$ respectively.

Table 3.1: Turn-On Checklist

1. Check to see if rotameters are fully open
2. Check to see if air accumulator is fully closed
3. Check all gage readings
4. Turn on thermocouple reader
5. Check temperature readings
6. Plug in Tuthill pump – Astron power supply
7. Plug in H_2O pump
8. Plug in scavenging pump
9. Plug in fans
10. Plug in heater power supply
11. Check all other switches and valves to make sure they are in proper position
12. Turn on power from outlet

After the initial setup has been completed, a checklist for the operating procedure has been formulated and should be followed to obtain the most accurate results.

Table 3.2: Operating Procedure Checklist

1. Check rotameter settings- (match sump flow rate to spray nozzle flow rate)
2. Open air accumulator to get flow steady
3. Balance Tuthill and sump rotameters, make sure flow in equals flow out
4. Read pressure at the following locations:
    a. Rotameters
    b. Nozzle
    c. Chamber
    d. Sump
5. Read temperature at the following locations:
    a. Pedestal (6 to 7 thermocouples depending on pedestal used T1-T6 or T7)
    b. Chamber (Six thermocouples (T8-T13))
    c. Nozzle (one thermocouple, T14)
6. Adjust flow rate according to desired test rate
7. Start pedestal heater (do not exceed 50W for the ITO Heater)
8. Record thermocouple recordings
9. Repeat Steps 3 → 5
10. If more tests are desired go back to step 6

CHAPTER 4 PRESENTATION OF RESULTS AND DISCUSSION:

In this chapter, the results will be presented and discussed in seven different sections covering data for conditions ranging from vertical downward sprays to horizontal spray conditions. Section 4.1 will reveal the apparatus's ability to operate under steady state conditions for a period of time. Sections 4.2 and 4.3 will illustrate the results of vertical downward sprays and horizontal spray studies respectively. The vertical spray conditions will consist of the spray directed in a downward position, while the horizontal spray condition will consist of a spray positioned in the horizontal position. Sections 4.4 and 4.5 will present the comparison study between spray orientations as well as between the two different types of heating sources (Ceramic and ITO). Section 4.6 will show the calculated heat transfer coefficient at different spray orientations and flow rates. Section 4.7 will illustrate preliminary flow visualization results obtained with the use of a high speed video camera and laser light sheet illumination.

A non-dimensional analysis was completed for use in the comparison of the present results with previous related work. Three non-dimensional parameters were computed: the Weber number (We), Reynolds number (Re), and Marangoni number (Ma). The Marangoni number is dependant on the Reynolds Number and Weber Number. The equation for the Marangoni number is

$$Ma = \frac{\mathrm{Re}}{We} \qquad 1$$

Equation 2 is the equation used to calculate the Weber number

$$We = \frac{\rho V^2 D}{\sigma} \qquad 2$$

where ρ is the density, V is the velocity, D is the diameter of the spray droplets, and σ is the surface tension of the liquid.

Equation 3 was used to calculate the Reynolds number

$$\mathrm{Re} = \frac{\rho V D}{\mu} \qquad 3$$

where μ is the viscosity of the liquid.

Baysinger et al., 2004 using a nozzle identical to the one in this research project, found that a spray flow rate of 9 GPH produced a spray droplet with a size of approximately 40 microns and a velocity of 12 m/s. Using the size and velocity of the spray droplets, the Weber number and Reynolds number were found to be 1141 and 1655 respectively. The Marangoni Number yields a value of 1.45. A Marangoni number approximately equal to 1 indicates that neither the viscous or surface tension forces are dominant. Also, the relatively large values of the Weber and Reynolds numbers indicate that droplet momentum dominates over both surface tension and viscous forces.

Tables 4.1 through 4.3 present a typical set of data that was used to produce the following results. Locations for thermocouples T_1 through T_6 and T_8 through T_{14} have been shown in Figure 3.23 and Figure 3.14 respectively. The complete data set used for the Results and Discussion section can be seen in Appendix B.

Table 4.1: Data for Power, Flow Rates, and Pedestal Thermocouples for Terrestrial Gravity Conditions with the TFR (Ceramic Thick Film Resistor)

	$\dot{V}$			Ped. Thermocouples					
Power	Nozz	Sump	H2O	T_1	T_2	T_3	T_4	T_5	T_6
Watts	GPH	GPH	GPH	°C	°C	°C	°C	°C	°C
9.92	6.2	6.2	12	31.1	23.5	26.9	24.1	26.7	25.0
20.02	6.2	6.2	12	41.0	26.5	33.2	27.6	32.0	29.3
29.89	6.2	6.2	12	50.0	29.3	38.9	30.5	36.9	32.6
39.93	6.2	6.2	12	58.9	32.1	45.0	34.0	41.9	36.5
50.06	6.2	6.2	12	66.9	34.7	50.3	36.9	46.5	39.8
60.12	6.2	6.2	12	74.5	37.4	55.4	39.2	50.5	42.8
70.03	6.2	6.2	12	80.1	40.3	59.9	42.3	54.8	45.8

Table 4.2: Chamber Temperatures for Terrestrial Gravity Conditions with the TFR

Chamber Temperatures						
T_8	T_9	T_{10}	T_{11}	T_{12}	T_{13}	T_{14}
°C	°C	°C	°C	°C	°C	°C
25.4	24.5	25.5	25.2	24.6	25.3	24.6
25.0	25	26.7	25.5	24.9	25.3	26.0
25.7	25.6	28.4	26.6	25.6	26.0	26.9
26.7	26.3	30.0	27.8	27.0	26.6	28.1
27.4	27.1	31.7	29.2	28	27.5	29.2
28.4	28.0	32.9	30.3	28.9	28.0	30.4
29.4	28.5	33.8	31.1	29.9	28.7	31.5

Table 4.3: Apparatus Pressures for Terrestrial Gravity Conditions with the TFR

Press					
Drain	FC-72 Heat X	Nozz	Chamber	Nozz	Sump
psia	psia	psia	psia	psia	psia
9.8	17.6	14.5	10.5	15.4	14.8
9.8	17.6	14.5	10.5	15.4	14.9
9.8	17.6	14.7	10.5	15.5	14.9
10.0	17.6	14.8	10.7	15.5	15.0
10.2	17.9	14.8	10.7	15.6	15.0
10.2	17.9	15.0	11.0	15.9	15.1
10.5	18.1	15.1	11.2	15.9	15.2

Figure 4.1 shows the trend of heater power and temperature for all test runs. These 37 different data sets show the general trend of all the data collected. The trends of

all the data have a slight S shape curve and resemble qualitatively the data presented by Baysinger (2004), Lin and Ponnappan (2003), and Tilton (1989). Baysinger (2004) and Tilton (1989) studied the effects of a single nozzle where Lin and Ponnappan (2003) used an array of nozzles for their spray cooling. During one of the data runs the CHF occurred causing one curve to reach a temperature of approximately 95 ^{o}C.

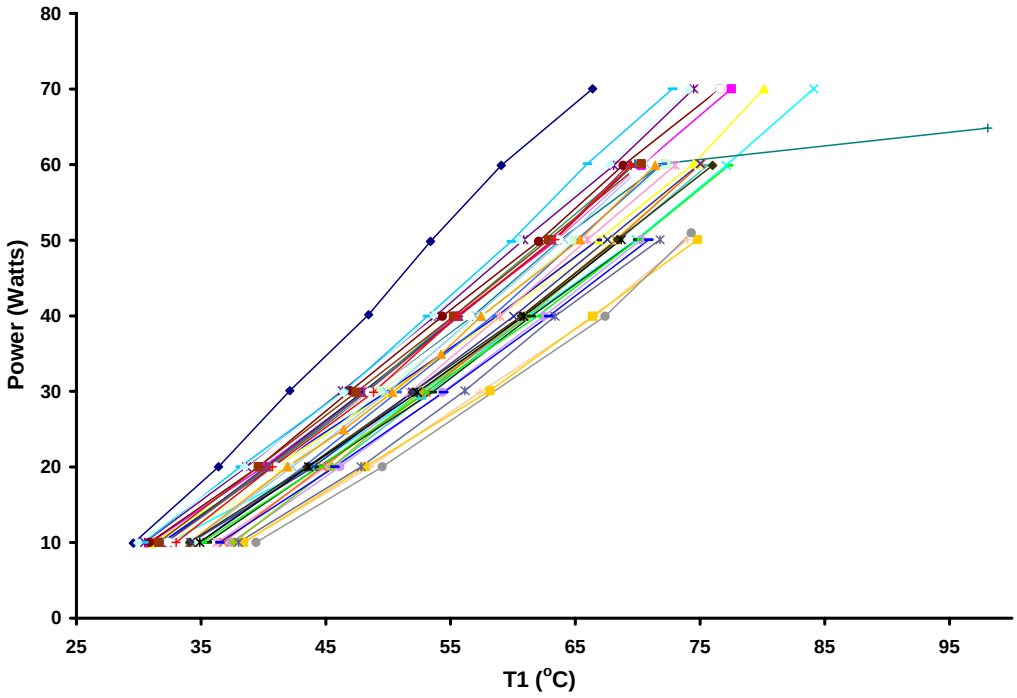

Figure 4.1: Master Plot of all Data Collected During the Present Research Showing the Temperature of Thermocouple T_1 as a Function of the Heater Power

4.1 Evaluation of Steady State Operation:

Figure 4.2 shows data consisting of temperatures near the heater surface (T1), and in the spray chamber (T8) as well as the chamber pressure, power input, and flow rate as a function of time for the spray directed vertically downwards ("Terrestrial gravity") at a nominal flow rate of 9.3 GPH. Each reading was recorded in one minute intervals for 21 minutes total. There are no apparent trends that can be noticed from any of the readings, and therefore it can be said that the apparatus stays at steady state for data collecting in the present work.

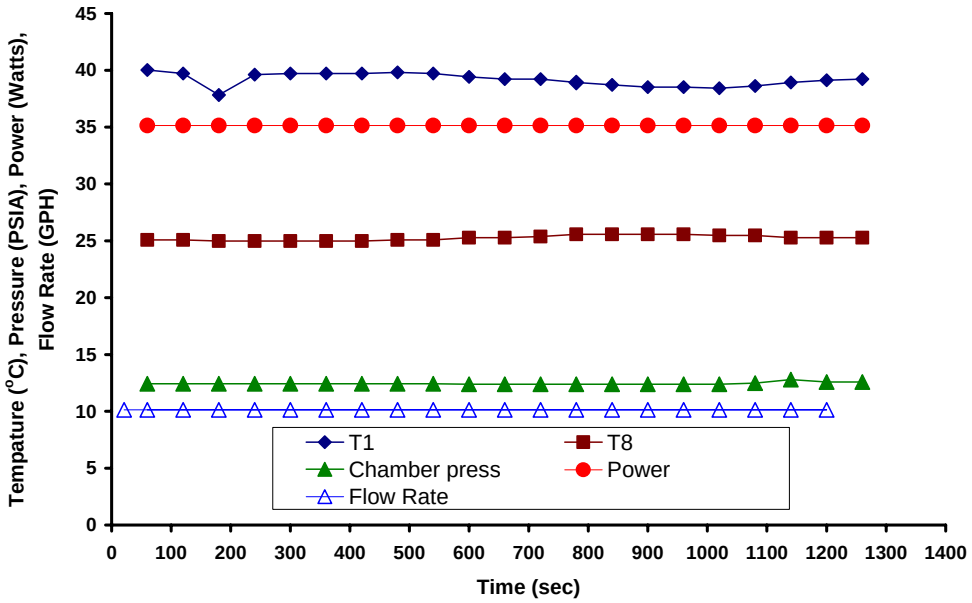

Figure 4.2: T_1, T_8, Chamber Pressure, Power, and Flow Rate as a Function of Time

4.2 *Vertical Downward Spray:*

Figure 4.3 shows the experimental heat flux versus T_1 minus the saturation temperature of the refrigerant FC-72 for varying flow rates for a vertical downward spray. The heat flux was computed by taking the amount of power going to the heater divided by the total surface area. The amount of Q (thermal heat) was computed knowing the voltage and current that was experienced by the thick film resistor. The heat loss down the pedestal was neglected since Baysinger (2004) used identical material for her experiment and found the loss to be 1 to 3 percent. Figure 4.3 presents results for the unconfined geometry under conditions of vertical downward spray. Figures 4.4 and 4.5 also show the heat flux as a function of surface temperature, but for the curved cap and straight cap respectively. Figure 3.21 shows a sketch of both the straight and curved caps.

All three figures show the same trend, that as the heat flux increased so did the surface temperatures. For the unconfined flow, the higher flow rates provided higher

levels of cooling. This would be expected as the spray keeps the heated surface flooded and washes any vapor bubbles away, preventing dry out. Also, convective heat transfer would be greater for the higher liquid flow rates. Each figure displays the average saturation temperature and sub-cooling temperature difference during the experiment. Knowing the thermodynamic properties of FC-72 and the spray chamber pressure, the saturation temperature could be calculated. This temperature helps to understand the trend of the curves. The sub-cooling was calculated as the difference between the saturation temperature and the temperature of the fluid coming into the spray chamber. The saturation temperature and sub-cooling temperatures varied from 41.8 ^{o}C to 50.0 ^{o}C and 22.3 ^{o}C to 24.5 ^{o}C during terrestrial gravity testing.

Some curves have more data points than others due to the fact that certain flow rates allowed higher power and temperatures to be read. For the following figures, when T_1-$T_{sat} < 0$, boiling cannot exist because the temperature of the fluid could not possibly reach the saturation temperature. For T_1-$T_{sat} > 0$, boiling and phase change could be expected as the temperature of the fluid has the possibility to be above the saturation temperature.

The estimated errors are computed for Figures 4.3, 4.4, and 4.5 to show the uncertainty of the heat flux and T_1-T_{sat}. The error for the heat flux was computed from the specifications in the instruction manual for the power supply used to power the heated surface. The error for T_1-T_{sat} was calculated with the uncertainty of the two mercury thermometers used to calibrate T_1 with an accuracy of 0.1 ^{o}C, and the accuracy of the spray chamber pressure gage which yielded the pressure that was used to interpolate for the saturation temperature. The error for the heat flux was larger than the error for T_1-

T_{sat}, having an average error of 4.2%. As the current and voltage was increased the percentage of error decreased. The overall estimated error for T_1-T_{sat} was 0.73 ^{o}C, combining both the error for T_1 and T_{sat}. Figure 4.3 shows that the highest flow rate has a significantly larger efficiency of cooling compared to the other three flow rates. There is not much difference in cooling efficiency for the lower three flow rates which are within the band of uncertainty.

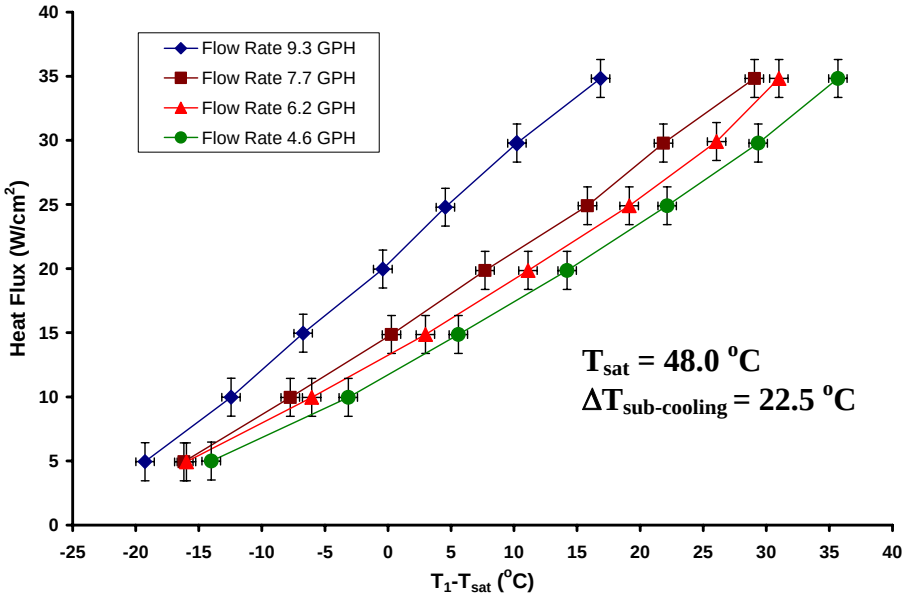

Figure 4.3: Heat Flux as Function of Surface Temperature for Various Flow rates with an Unconfined Flow, for Vertical Downward Spray

Figure 4.4 presents the results for the curved cap, which has a curved area inside of the cap allowing the fluid to exit the surface of the pedestal in a radial direction further without contacting the cap. Figure 4.4 shows that flow rates 9.3 and 7.7 GPH have almost the same trend followed closely by 6.2 GPH. This Figure also shows that 4.6 GPH has a significantly lower cooling efficiency when compared to the three higher flow

rates. The three higher flow rates are all within the range of probable error. The lowest flow rate had a significantly lower cooling efficiency and is not within the error band for the three higher flow rates.

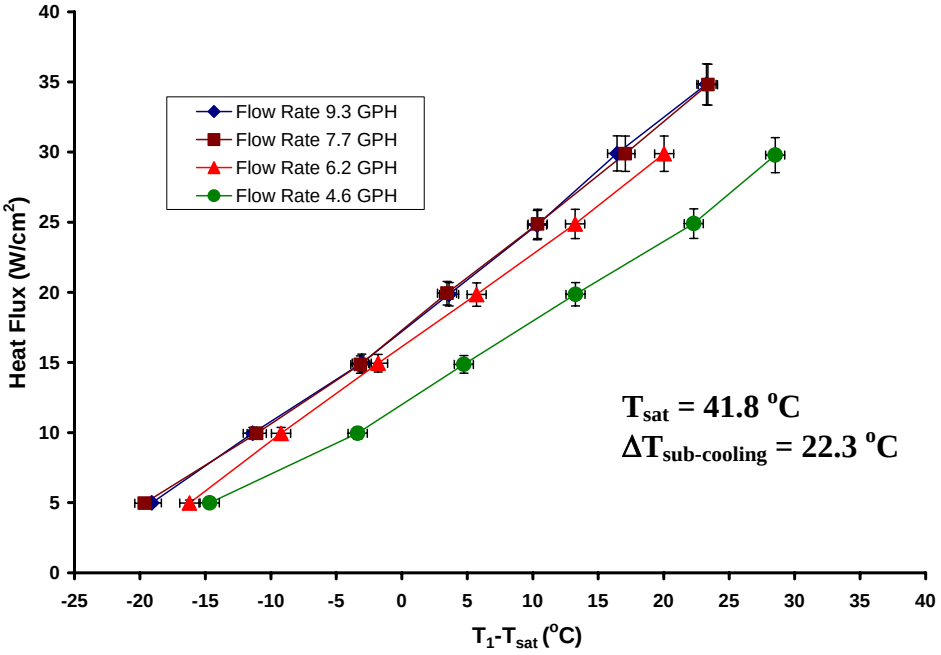

Figure 4.4: Heat Flux as a Function of Surface Temperature with Various Flow rates for the Curved Cap, for Vertical Downward Spray

Figure 4.5 presents results for the spray cooling process with a straight conical cap which confines the flow more than either the curved cap or the unconfined flow. This figure shows that the three highest flow rates have nearly the same cooling efficiency and all are within the band of error. An explanation for the three highest flow rates being much closer in efficiency than in the unconfined study could be the recirculation pattern caused by the cap. This could be beneficial in a microgravity environment where, due to the absence of the body force, the surface tension forces are a more significant effect.

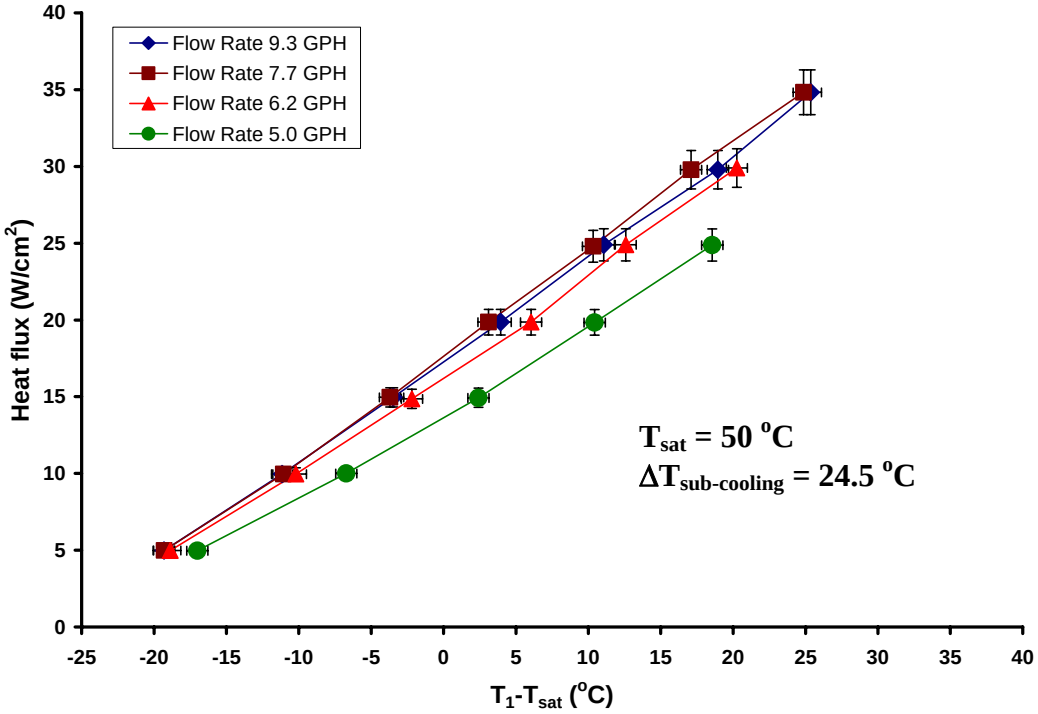

Figure 4.5: Heat Flux as a Function of Surface Temperature for Various Flow Rates for the Straight Cap, for Vertical Downward Spray

Figure 4.6 is a sketch to present the hypothesis of recirculation or rebound due to the cap geometry. As the fluid impinges onto the heated surface it splashes off the pedestal and then impinges on the cap and back onto the pedestal again, rewetting the surface.

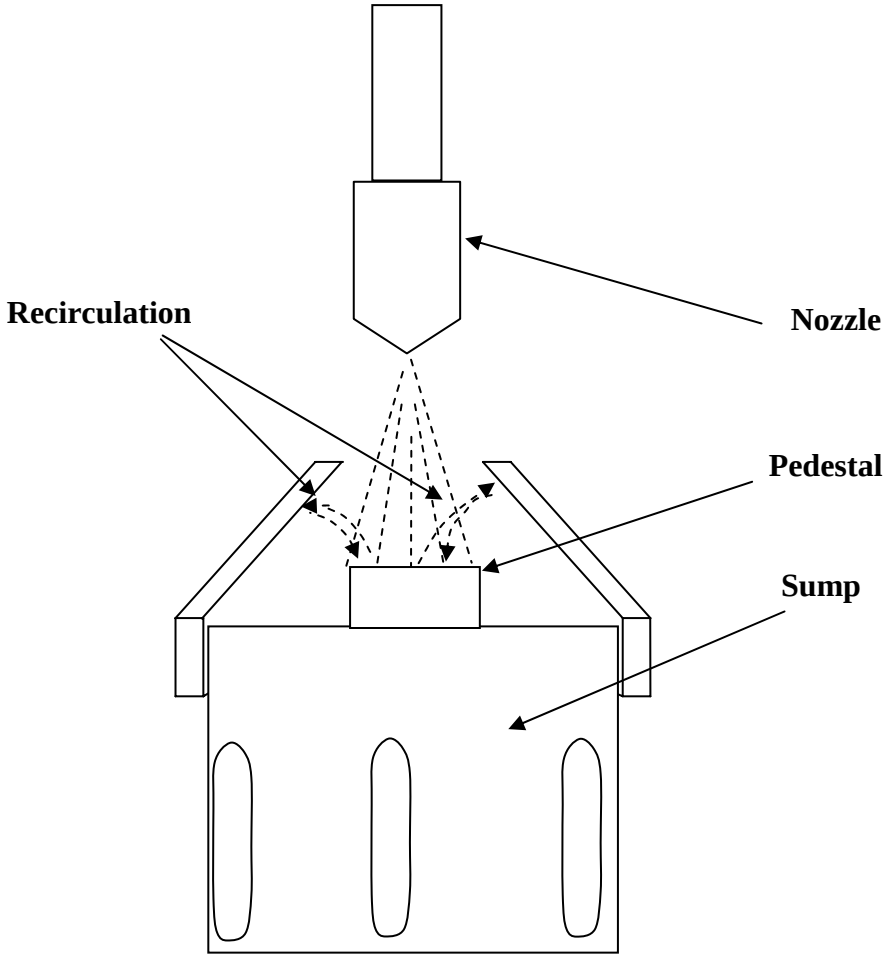

Figure 4.6: Sketch of the Hypothesis of Recirculation of the Spray Droplets

Figures 4.7 through 4.10 show a heat flux as a function of sub-cooling with geometry as a parameter for each flow rate. Error bars have not been shown to make the figures less cluttered. These figures are cross plots of the three previous figures. Figure 4.7 shows heat flux versus the surface temperature for the three different geometries at the largest spray flow rate 9.3 GPH. As the figures increase from 4.7 to 4.10, the flow rates decrease from 9.3 to 4.6 GPH. Figures 4.7 through 4.10 illustrate more clearly that as the spray flow rate decreases, the more confined the flow the better the cooling efficiency. At the lowest flow rate, 4.6 GPH, the straight cap is more efficient than the

other two geometries. 4.6 GPH was the lowest flow rate that could be achieved without subjecting the experimental apparatus to CHF and malfunction. This is why one of the spray flow rates for this figure is 5.0 GPH instead of 4.6 GPH.

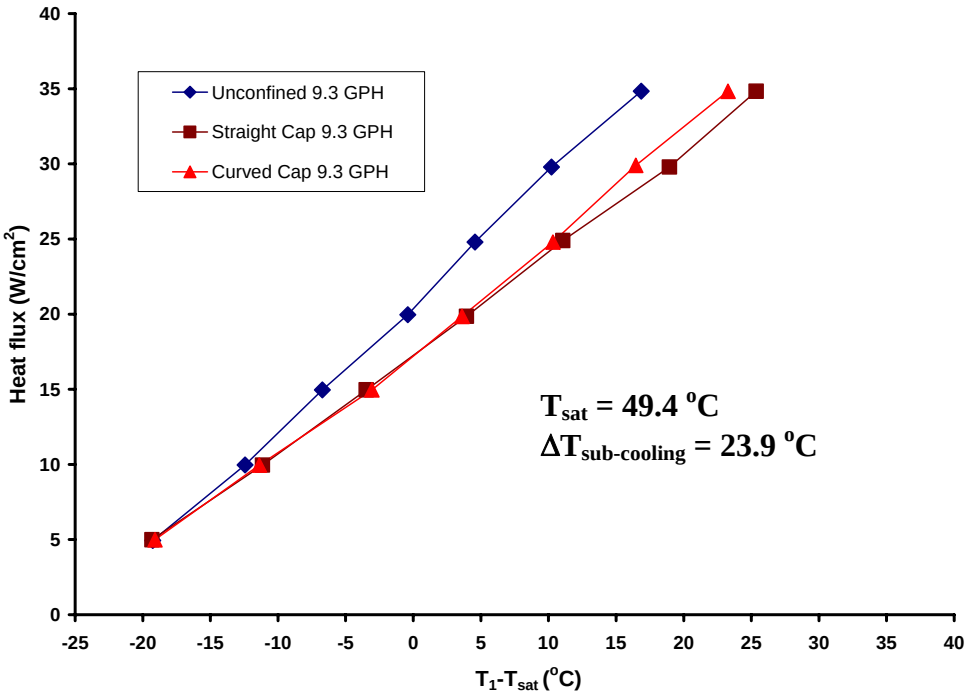

Figure 4.7: Heat Flux as a Function of Surface Temperature for the Different Geometries with a Fixed Flow Rate of 9.3 GPH, for Vertical Downward Spray

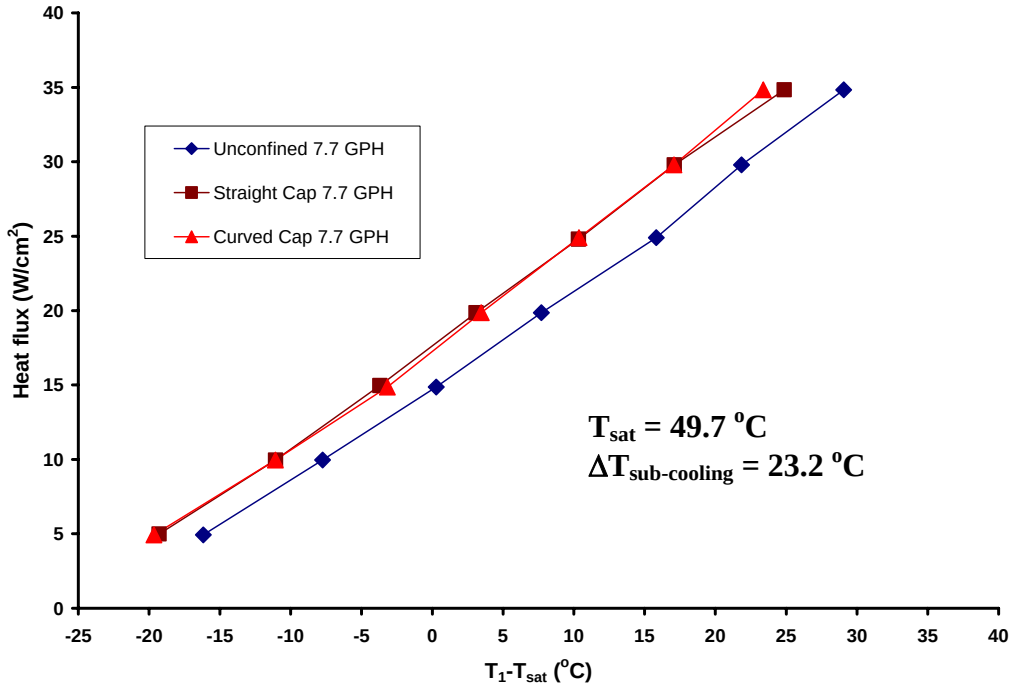

Figure 4.8: Heat flux as a Function of Surface Temperature for the Different Geometries with a Flow Rate of 7.7 GPH, for Vertical Downward Spray

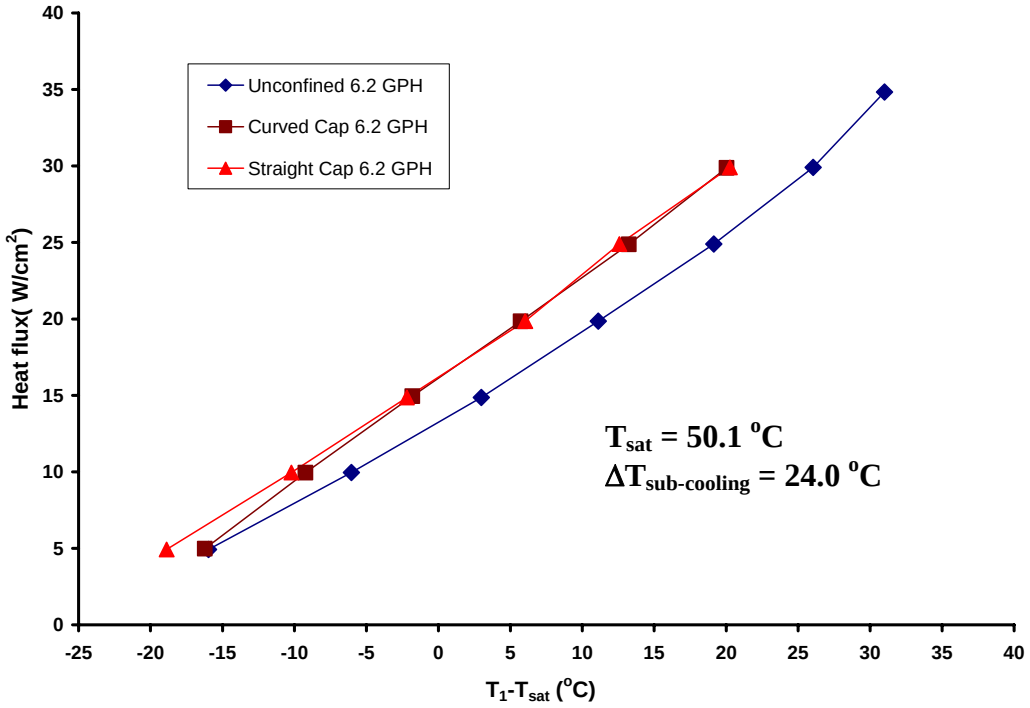

Figure 4.9: Heat Flux as a Function of Surface Temperature for the Different Geometries with a Flow Rate of 6.2 GPH, for Vertical Downward Spray

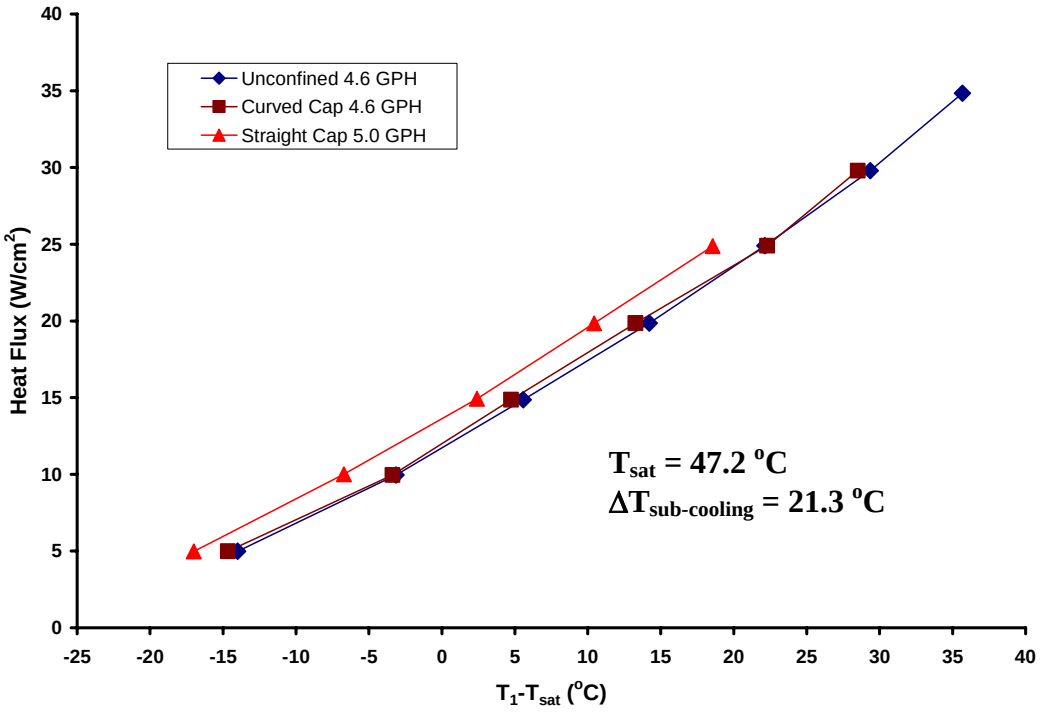

Figure 4.10: Heat Flux as a Function of Surface Temperature for the Different Geometries with a Flow Rate of 4.6 GPH, for Vertical Downward Spray

4.3 Horizontal Spray:

Microgravity was simulated in the present work using a horizontal spray, consistent with the definition of Kato et al. (1994). Yoshida et al. (2001) also presented simulated microgravity work except instead of using a horizontal spray they used a vertical upwards spray. For the present data, a hole was drilled in the view port located at the bottom of the spray chamber for use as a drain when rotated to the horizontal spray position. The plumbing between the spray chamber and the sump pump was also modified to allow the sump pump to drain fluid either from the sump (for vertical spray operation) or from the bottom of the view port (for horizontal spray operation). This allows the fluid to drain properly and the sump pump to run correctly.

Figures 4.11 through 4.13 show the experimental heat flux for the horizontal sprays as a function of surface temperature for various flow rates. Figure 4.11 shows the classic trend that as the heat flux increases so does the surface temperature. Not much difference can be seen in the trends for the terrestrial gravity and the simulated microgravity cases with the unconfined flow.

Figure 4.12 and 4.13 follow the same trend as Figure 4.11, where an increase in flow rate also increased the cooling efficiency. These results are consistent with the explanation of recirculation for the confined flows in terrestrial gravity. With simulated microgravity the fluid was not able to recirculate as the draining is different for the two different testing methods.

The same error analysis was completed for the horizontal spray data as for the vertical downward spray. Figures 4.11 through 4.13 have error bars to show the estimated uncertainty for each measurement. Although the error bars sometimes overlap, there is a clear and consistent trend of lower surface temperature as the flow rate is increased.

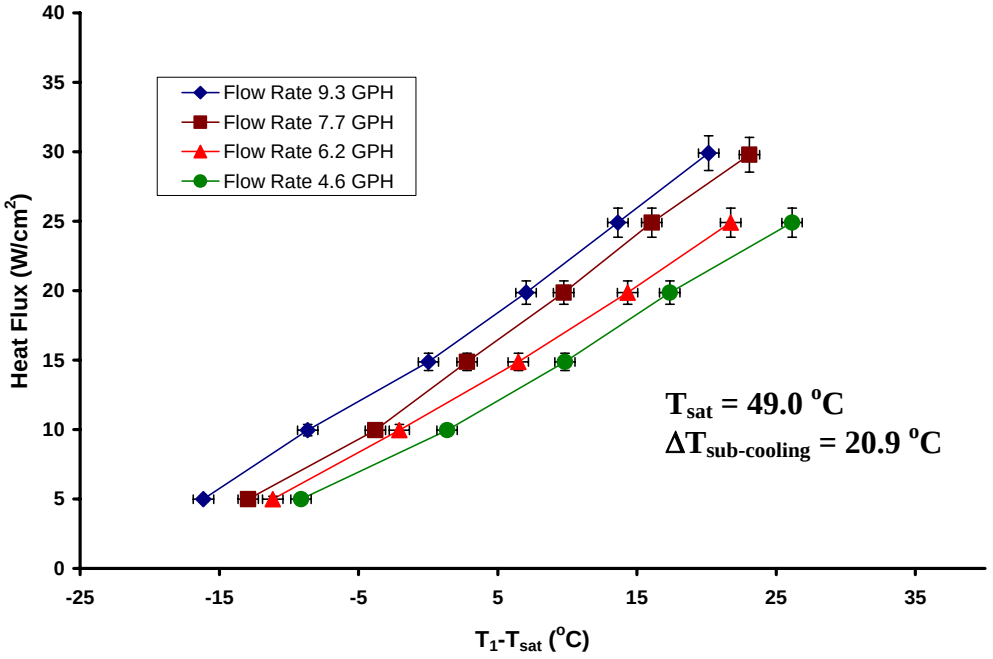

Figure 4.11: Heat Flux as Function of Surface Temperature for Various Flow Rates with an Unconfined Flow for a Horizontal Spray

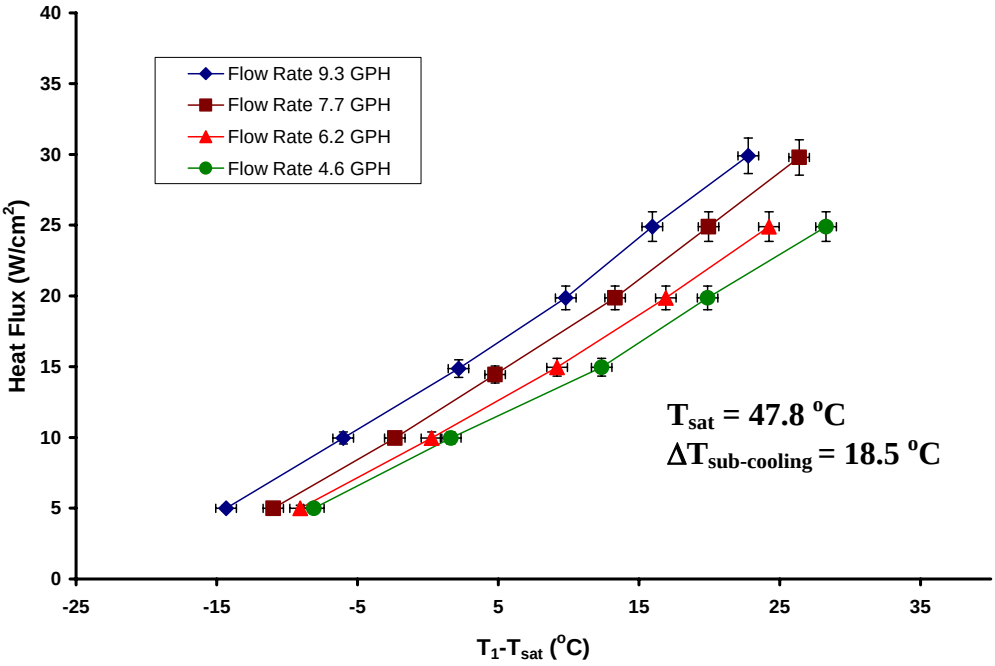

Figure 4.12: Heat Flux as a Function of Surface Temperature with Various Flow Rates for the Curved Cap for a Horizontal Spray

Figure 4.13 also supports the explanation of recirculation and shows the same trend as the two previous figures. Figure 4.13 also shows the lowest amount of sub-cooling, and this is attributed to the increase of room temperature during testing. Here, the amount of sub-cooling is the saturation temperature minus the temperature of the fluid entering the spray chamber. T_{14} was used to obtain the temperature before entering the nozzle's orifice (see Figure 3.14).

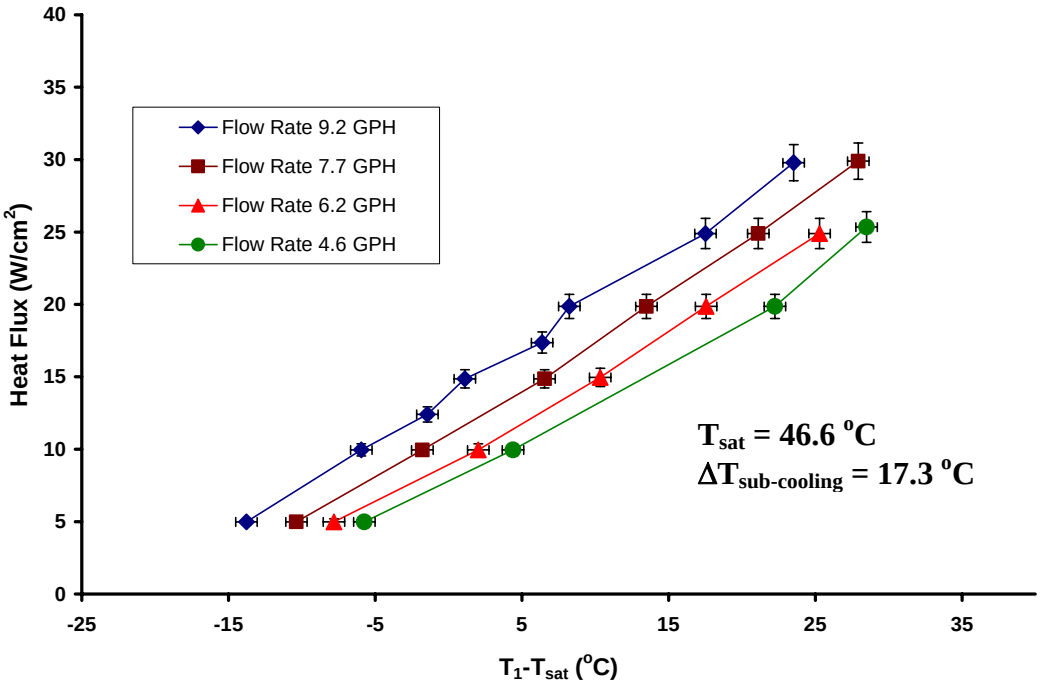

Figure 4.13: Heat Flux as a Function of Surface Temperature for Various Flow Rates for the Straight Cap for a Horizontal Spray

Figures 4.14 through 4.17 are cross plots of the previous three figures. Figures 4.14 through 4.17 show the horizontal spray heat flux as a function of surface temperature for the three different geometries, each with a fixed flow rate. Figure 4.14 shows the highest flow rate tested for the horizontal spray, 9.3 GPH. The same flow rates used for the vertical downward spray conditions were used for the horizontal spray. This

was done to compare results from both tests, but the sub-cooling and saturation temperatures were too different to make a good comparison between the two spray orientations. Figure 4.14 shows that none of the geometries were clearly superior in cooling efficiency at this flow rate, but the unconfined flow had the largest amount of heat removal at a given temperature.

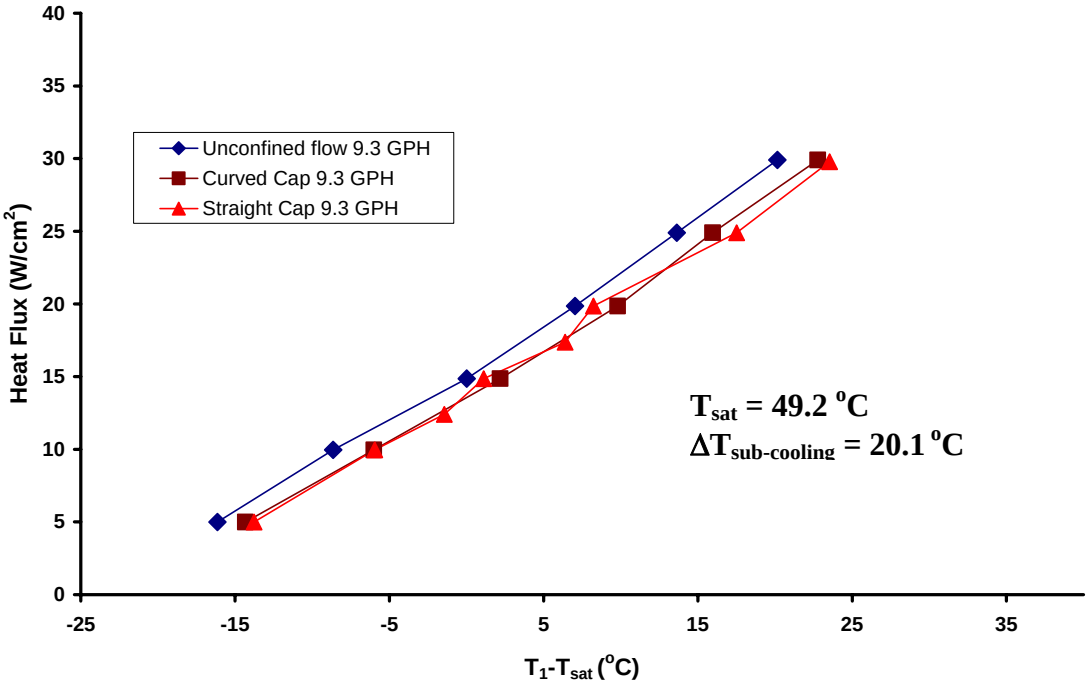

Figure 4.14: Heat Flux as a Function of Surface Temperature for the Different Geometries with a Fixed Flow Rate of 9.3 GPH for a Horizontal Spray

Figure 4.15 also shows that the unconfined flow had the best spray cooling efficiency at a spray flow rate of 7.7 GPH. Both the straight and curved cap presented results that were similar in heat removal. Figure 4.16 also shows that the unconfined flow proved to be most efficient in cooling at a flow rate of 6.2 GPH. There was not very much difference in the heat removal for both cap geometries.

Figure 4.17 showed results at the lowest spray flow rate for all three geometries. At this flow rate all three geometries seemed to have nearly the same values for heat removal. The unconfined geometry still was the most efficient, although the straight and curved cap curves were very similar.

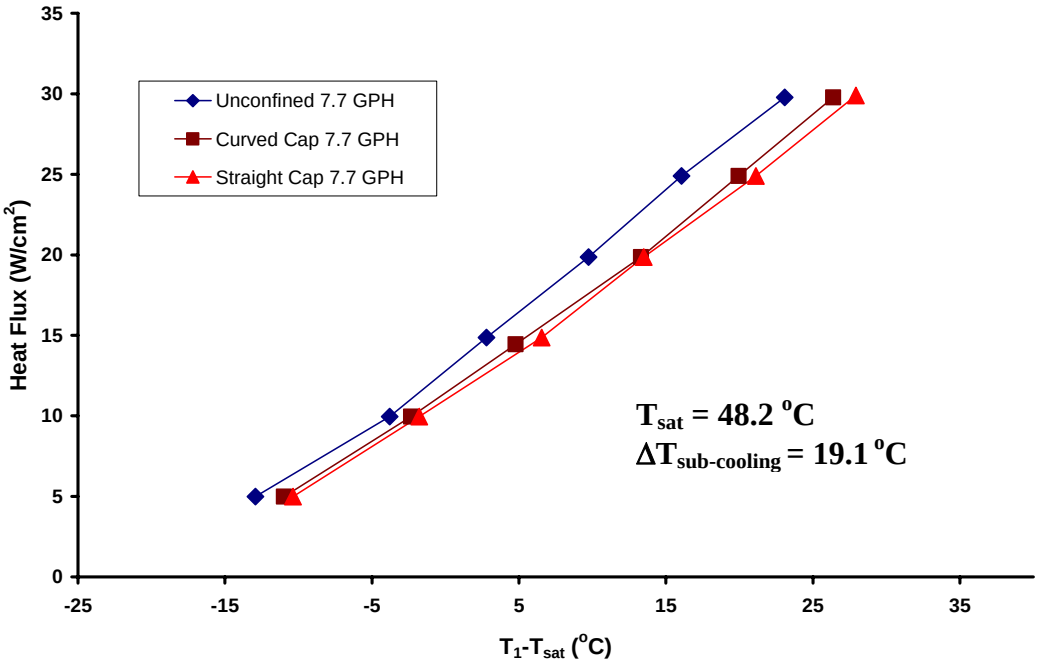

Figure 4.15: Heat flux as a Function of Surface Temperature for the Different Geometries with a Flow Rate of 7.7 GPH for a Horizontal Spray

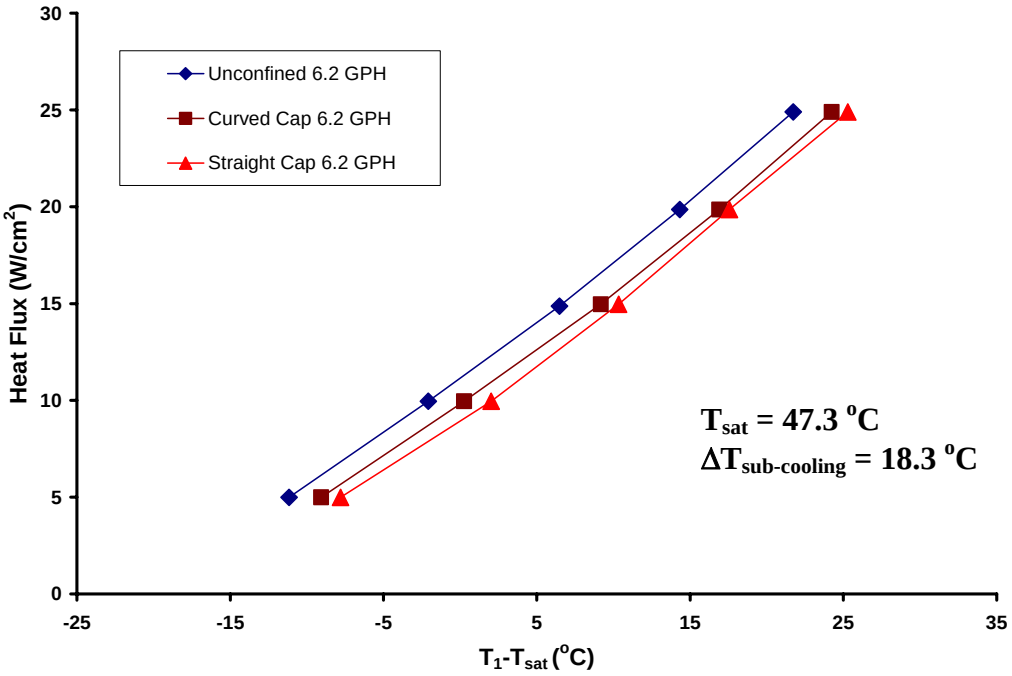

Figure 4.16: Heat Flux as a Function of Surface Temperature for the Different Geometries with a Flow Rate of 6.2 GPH for a Horizontal Spray

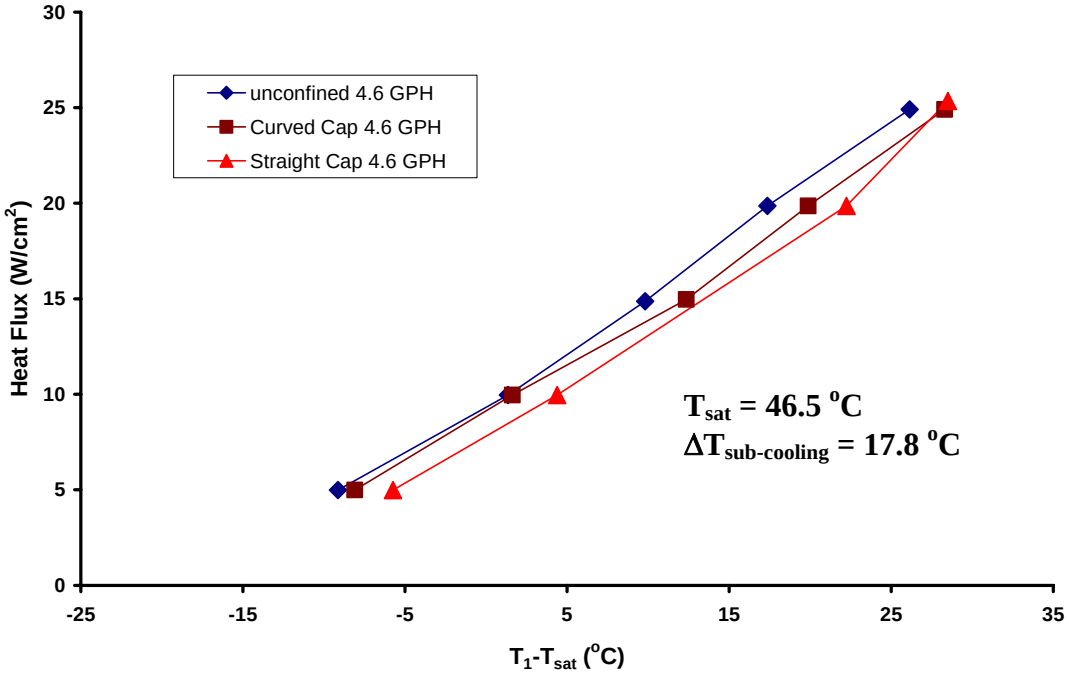

Figure 4.17: Heat Flux as a Function of Surface Temperature for the Different Geometries with a Flow Rate of 4.6 GPH for a Horizontal Spray

4.4 Comparisons between Vertical Downward Spray Data and Horizontal Spray Data Using the TFR Ceramic Heater:

Since the sub-cooling was so different for the above vertical and horizontal spray tests, another data set was recorded. During this test the spray chamber pressure and temperature of the fluid entering the nozzle were both closely monitored to be as close to constant as possible, for the best comparison. All data were recorded during the same test for each flow rate and geometry configuration. The experimental apparatus was never shut off as the spray chamber was rotated 90 degrees from a vertical spray to the horizontal spray position. The new plumbing allowed the spray chamber to rotate while still spraying.

Figure 4.18 shows the comparisons between vertical downward spray and the horizontal spray for the unconfined geometry at two different spray flow rates. The figure shows a distinct difference between the flow rates for both the vertical spray (VS) and the horizontal spray (HS). However, in contrast to evidence found in some previous work, this data did not show an improvement in cooling for the horizontal spray conditions for this type of geometry.

As discussed in Chapter 2, Yoshida et al. (2001) performed a study of spray cooling under reduced gravity conditions and found that spray cooling was more effective in simulated microgravity than in terrestrial gravity. For the present data in Figure 4.18, the horizontal spray results (filled symbols) are consistently less efficient than the corresponding vertical downwards spray results at the same flow rate. A reason for these results could be that with a change in plumbing for the vertical and horizontal spray could

cause less head loss and the sump pump can achieve a larger vacuum for the horizontal spray. This larger vacuum would cause a change in the saturation temperature and may be part of the reason for the apparent lower efficiency in the horizontal spray conditions. Another reason the data may not agree with the previous work is because of the widely different flow rates and fluids used which yield different non-dimensional values for parameters such as Weber number.

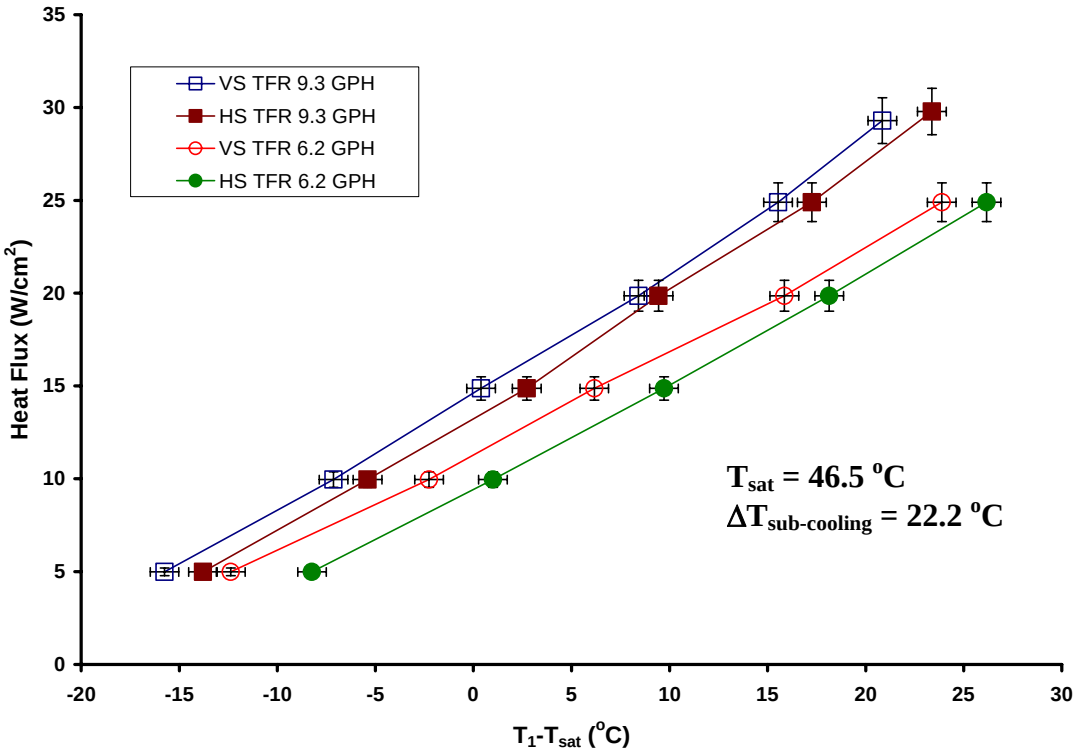

Figure 4.18: A Comparison of Vertical and Horizontal Spray Heat Flux as a Function of Surface Temperature for the Unconfined Geometry at Two Different Flow Rates

Figure 4.19 shows the comparison between vertical downward spray and the horizontal spray for the curved cap geometry. Again, the figure did not show a significant improvement with spray cooling in the horizontal spray. Each trend was very similar when compared at the same flow rate for both the vertical spray and the

horizontal spray. At the lower flow rate, the horizontal spray was slightly better at cooling for the curved cap geometry.

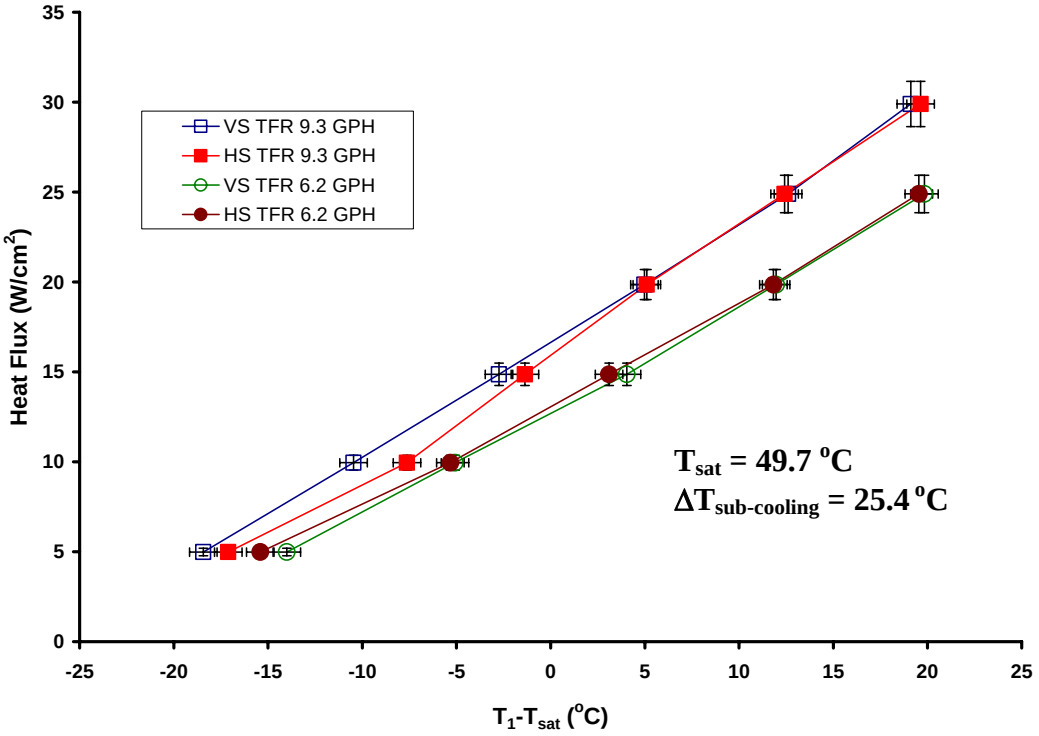

Figure 4.19: A Comparison of Vertical and Horizontal Spray Heat Flux as a Function of Surface Temperature for the Curved Cap Geometry at Two Different Flow Rates

Figure 4.20 shows the comparison between the vertical spray and the horizontal spray for the straight cap configuration for two different flow rates. Figure 4.20 actually shows that vertical downward spray was slightly more efficient at cooling than the horizontal spray conditions. These results are believable due to the recirculation of the confined geometry, but for the unconfined flow of Figure 4.18 it was expected that the results would indicate that the horizontal spray was better for spray cooling process. The reason for this inconsistency is unknown at this time.

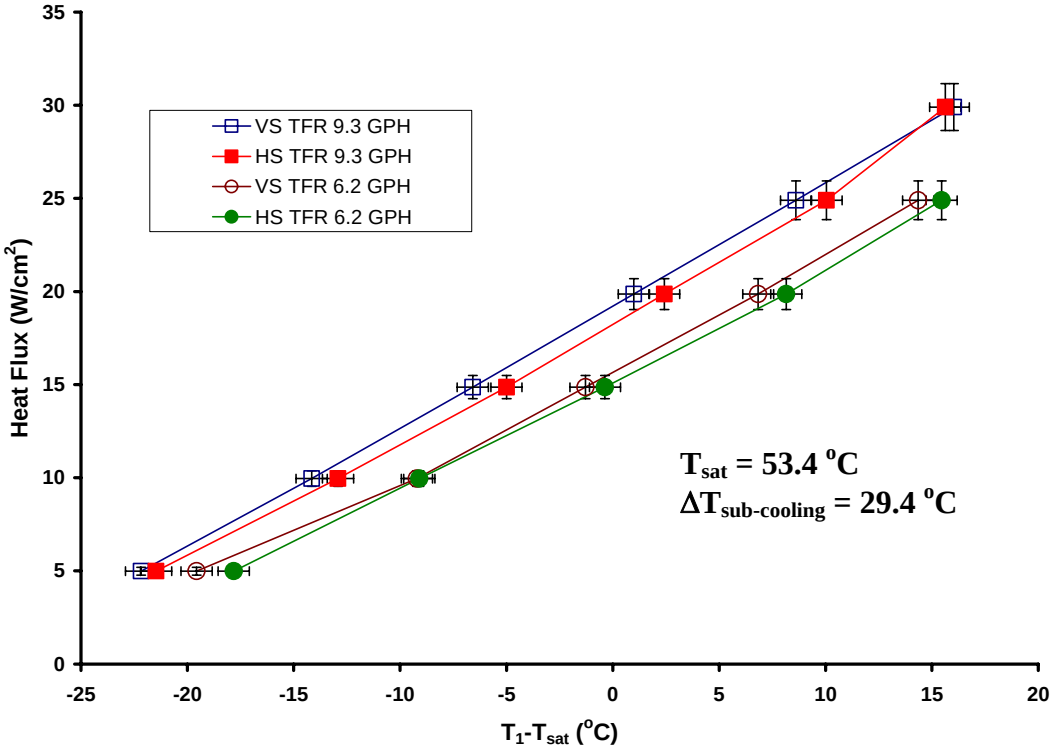

Figure 4.20: A Comparison of Vertical and Horizontal Spray Heat Flux as a Function of Surface Temperature for the Straight Cap Geometry at Two Different Flow Rates

4.5 Comparison between the Ceramic and ITO Heaters in Vertical Downwards Spray Conditions:

A comparison between the performance of the Ceramic Thick Film Resistor (TFR) and the transparent Indium Tin Oxide (ITO) heaters was conducted. This evaluation was also performed because the ITO heater was used during preliminary flow visualization tests. By evaluating both heaters one can see if any drastic differences occur during testing. Figure 4.21 shows the vertical spray cooling trends for the unconfined and straight cap geometries for both the TFR and ITO pedestals at the same spray flow rate of 9.3 GPH. Figure 4.21 illustrates that the spray cooling trends are fairly similar, but that the TFR can handle higher heat fluxes than the ITO without damaging the pedestal. One must be very careful and aware of the CHF when using the ITO heater

because exposing it to higher temperatures is very risky. With CHF, dry-out occurs, and puts the ITO heater in danger of being damaged. Also, the ITO heater consistently runs cooler than the TFR heater for both geometries. This may be because the ITO resistive film is in direct contact with the impinging spray.

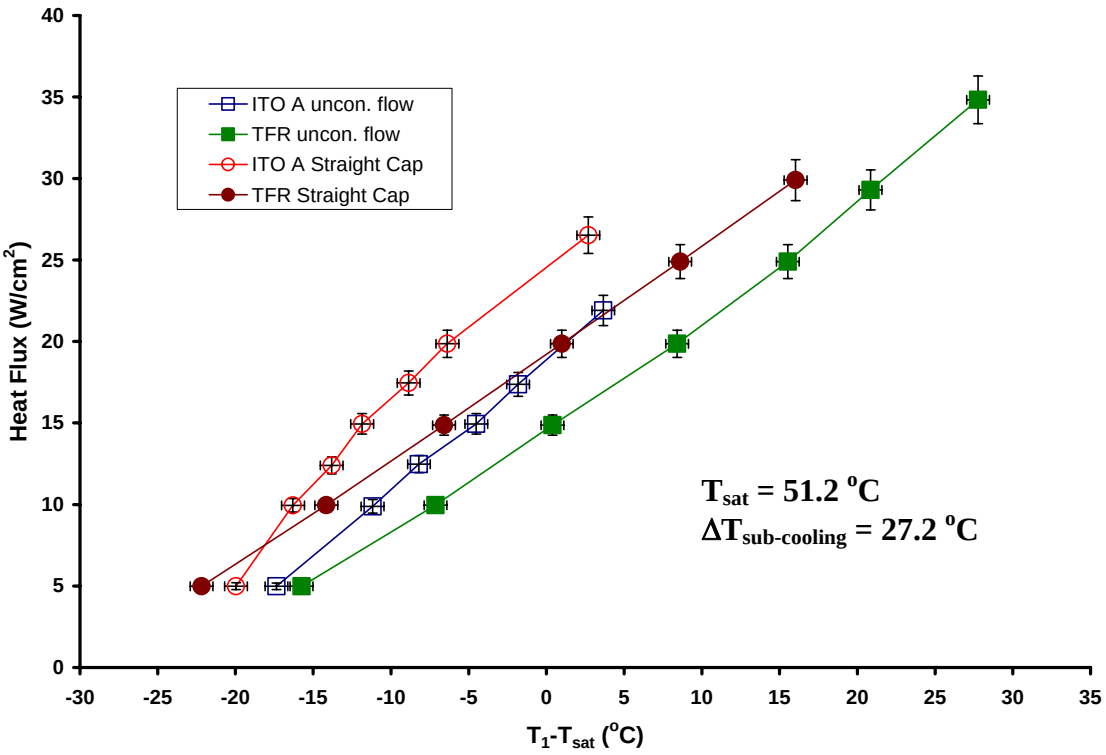

Figure 4.21: Comparison of Vertical Spray Heat Flux as a Function of Surface Temperature for Both the ITO A and TFR Pedestals at a Flow Rate of 9.3 GPH

For both the unconfined flow and the straight cap geometry, the present data indicate that the ITO heater is consistently more efficient than the TFR ceramic heater. This might perhaps be due to differences in construction of the two heater-pedestal geometries. The portions of the heater surface covered by the high-temperature conductive epoxy varied for these two pedestals as shown in Figure 4.22. Another reason for some of the differences is that both heaters have different thicknesses, and T_1 is located under the ceramic TFR or ITO heaters. The ceramic TFR heater is .025 inches

thick and was glued on with a less expensive epoxy than the ITO heater. The ITO heater has a thickness of .020 inches and was attached to the pedestal with optical cement for visualization reasons. The epoxy and optical cement used to glue on the ceramic TFR and ITO respectively could have different thermal conductivity properties and would cause a difference in temperatures for T_1 at identical surface temperatures. The estimated heated region for both the TFR and ITO pedestals is 1.79 cm^2 and 1.47 cm^2 respectively. These regions were estimated by measuring the amount of glue and calculating the unglued surface area.

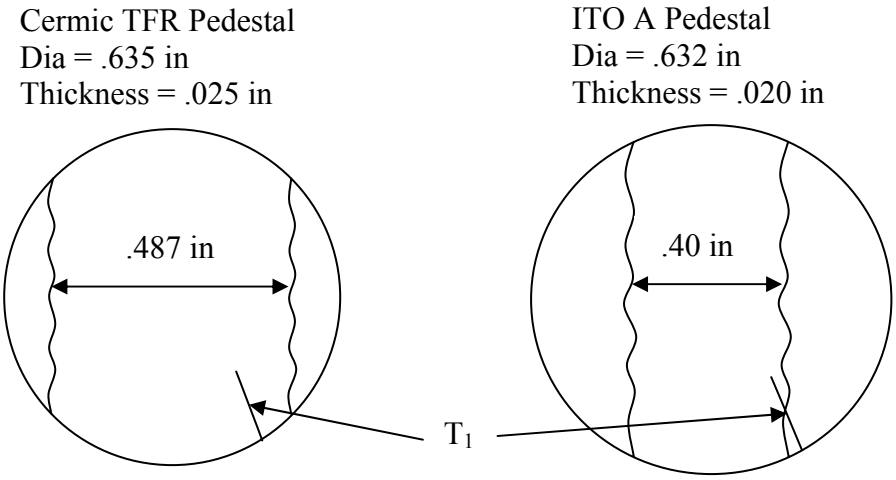

Figure 4.22: Sketch Showing the Comparison of High-Temperature Epoxy for the Ceramic TFR and ITO Heaters

4.6 Heat Transfer Coefficient:

The heat transfer coefficient was calculated to help in the evaluation of the cooling efficiency. As the value of h (heat transfer coefficient) increases so does the cooling efficiency. Equation 4 was used in determining the value of h

$$\dot{Q} = hA\Delta T \qquad 4$$

where $\dot{Q}$ is the heat transfer rate, A is the area of the heated surface on the top of the pedestal, and ΔT is the temperature difference between the fluid on the heated surface T_1 and the spray entering the system T_{14}. Figures 4.23 through 4.25 show the calculated convective heat transfer coefficient as a function of the heater power (Power is equal to the voltage multiplied by current). Figure 4.23 shows the expected trend that as the flow rate increased the value of h also increased. With the exception of the first point for the 9.3 GPH the general trend of the data shows as the power increased the value of h also increased a small amount. The inconsistency for the first data point on the 9.3 GPH trend could be due to the system not achieving steady state before testing was begun. For the 9.3 GPH flow rate the heat transfer coefficient stayed fairly constant in Figures 4.23, 4.24, and 4.25 with the exception of the first data point of Figures 4.23 and 4.24. The heat transfer coefficient ranged from roughly 4500 W/m^2K to 7500 W/m^2K for Figures 4.23, 4.24, and 4.25. These values for the present TFR results are somewhat lower than values reported by Baysinger (2004), of about 10,000 – 15,000 W/m^2K, for an ITO heater. This difference is consistent with the comparison of the present TFR and ITO results shown in Figure 4.21.

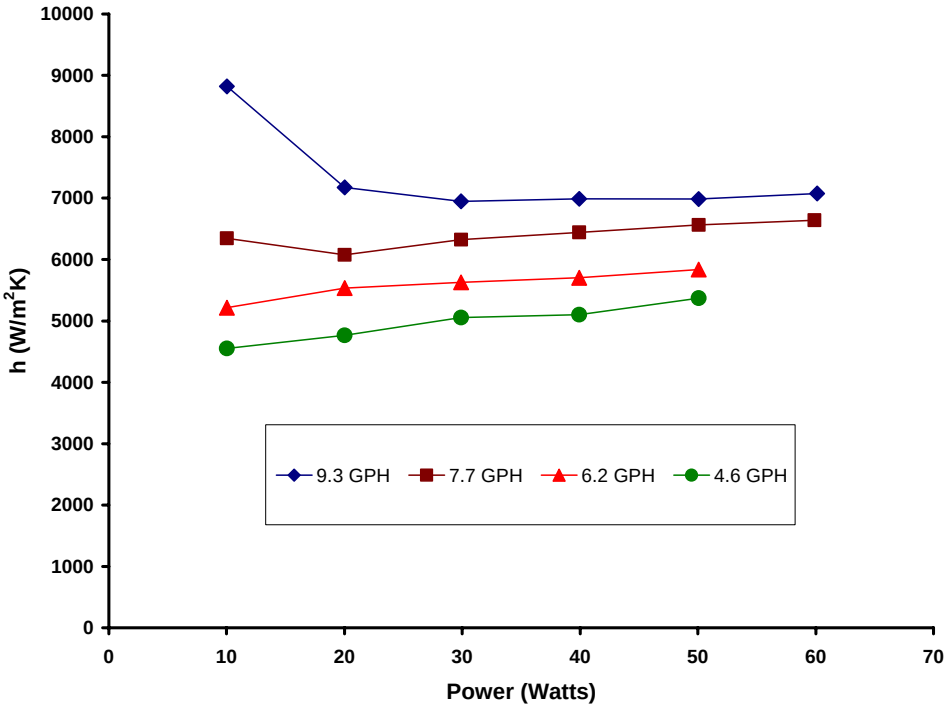

Figure 4.23: Heat Transfer Coefficient as a Function of Power for the Horizontal Spray with the Unconfined Geometry at Various Flow Rates

Figure 4.24 shows a similar trend as Figure 4.23. As the flow rate increased so did the heat transfer coefficient. Again the first data point of the highest flow rate (9.3 GPH) is different than the rest of the trends, possibly due to starting the test before the apparatus reached steady state.

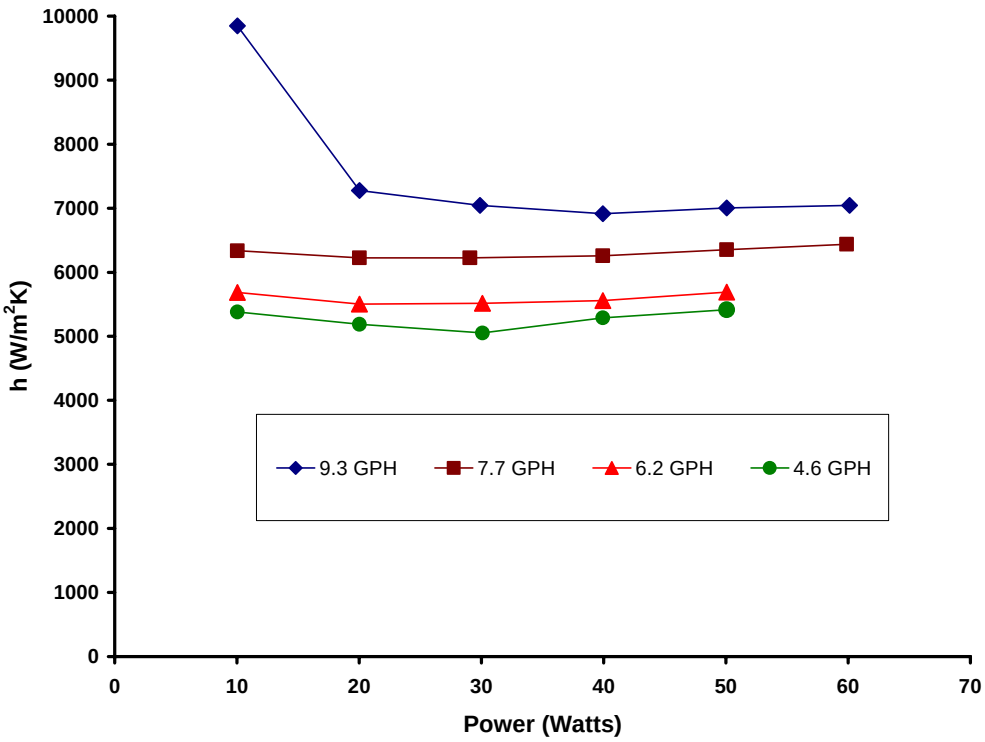

Figure 4.24: Heat Transfer Coefficient as a Function of Power for the Horizontal Spray with the Curved Cap Geometry at Various Flow Rates

Figure 4.25 also shows the same trend as Figures 4.23 and 4.24, that as the flow was increased so did the heat transfer coefficient. The values for the heat transfer coefficient stay fairly constant as the power was increased. The lowest flow rate, 4.6 GPH, shows the largest change in value for the heat transfer coefficient. For the four flow rates the heat transfer coefficient stayed mostly constant and no significant changes could be noticed. The increase in heat transfer coefficient as the power increased is similar to the general trend for Figures 4.23 and 4.24.

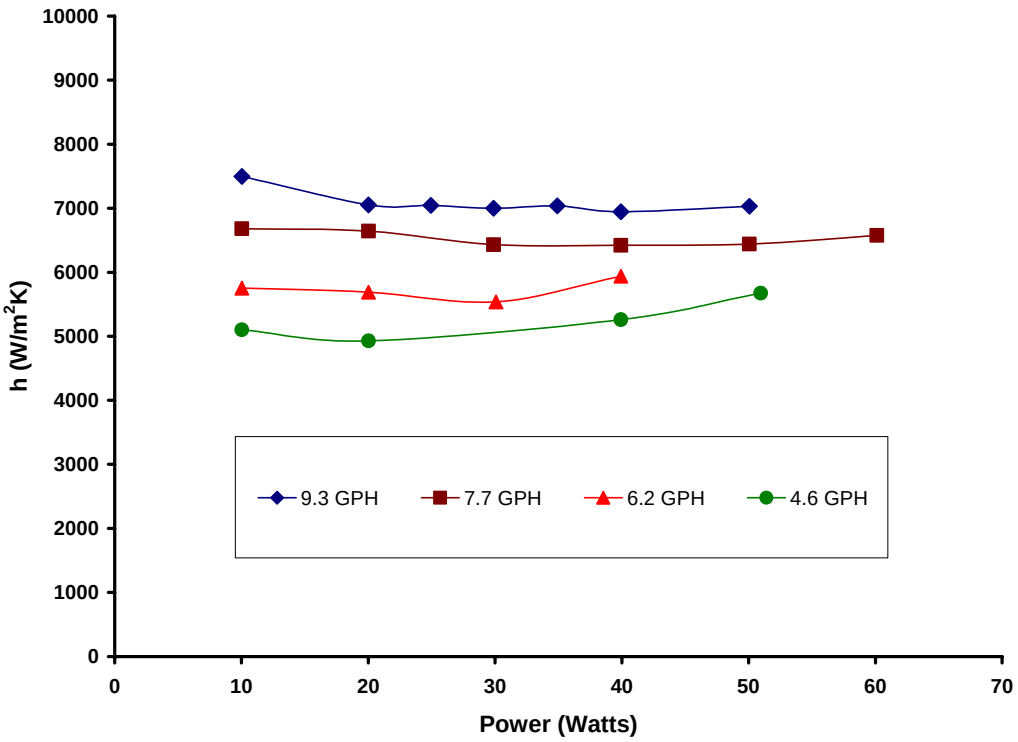

Figure 4.25: Heat Transfer Coefficient as a Function of the Power for the Horizontal Spray with the Straight Cap Geometry at Various Flow Rates

Figure 4.26 shows a comparison of the heat transfer coefficient between the vertical downward spray (VS) and horizontal spray (HS) at two different flow rates for the straight cap geometry. As the flow rate was increased so did the heat transfer coefficient for both the vertical and horizontal sprays. It can be seen that spray orientation did not change the value of the heat transfer coefficient. Therefore it can be stated that the heat transfer coefficient is not dependent on spray orientation. Again the lower flow rate 6.2 GPH showed an increase in h as the power was increased where the higher flow rate 9.3 GPH stayed fairly constant throughout the experimental test.

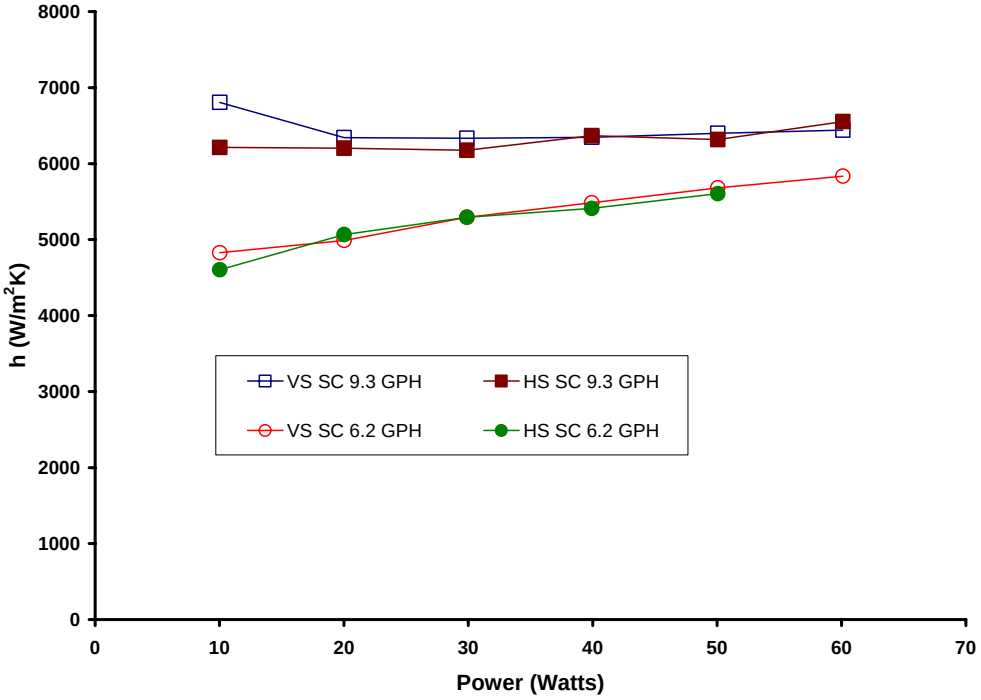

Figure 4.26: Heat Transfer Coefficient as a Function of Power for both the Vertical Downward Spray and Horizontal Spray with a Straight Cap

4.7 Preliminary Flow Visualization in Terrestrial Gravity using a Laser and High Speed Camera:

A high speed camera (Redlake model HG-LE) was used to gather video and still photographs that would help determine the flow physics, both in the spray and the interaction between the spray droplets and the vapor bubbles on the pedestals heated surface. A high-power Argon-ion laser light sheet was used to create the illumination for the high-speed videos. The light sheet was created by directing a high power laser beam into the center of a cylindrical glass rod. The laser sheet was always perpendicular to the glass rod and could be rotated to any angle by merely rotating the glass rod. Figure 4.22 shows a sample image from the video taken of the spray at 5.4 GPH exiting the nozzle and impinging on the heated surface with a heat flux of 17.11 W/cm^2. A swirling motion

is present in the figure and is due to the flutes just upstream of the spray nozzle orifice that helps in droplet generation. The light spots in the following still video images are the high power laser reflections off the spray droplets. As discussed in Chapter 2, pressure atomizing nozzle uses shear forces to produce the droplets. They also tend to impart a swirling motion that increases that spray cone angle. The relatively low spatial resolution in Figure 4.27 is the result of the high framing rate of 30,000 FPS.

Figure 4.27: Sample Video Image of Spray at 5.4 GPH Using a High Speed Camera Set at 30,000 FPS (Frames Per Second)

Figure 4.28 is a sample video image that was taken with the same Redlake high speed video camera using 1000 frames per second with a heat flux of 17.11 W/cm^2 at 5.4 GPH. Figure 4.28 shows both flooding and droplet splashing at a low flow rate of 5.4 GPH. The flow on the pedestal surface appears to be very turbulent. This figure does illustrate that use of the high speed camera with laser light sheet illumination shows promise for helping one to understand the flow physics and should be further investigated.

Figure 4.29 is a second sample video image from a high speed camera at a flow rate of 5.4 GPH and a framing rate of 3,000 FPS. This figure shows a large amount of splashing and flooding which would increase the rate of vapor bubbles being removed. Droplets can be seen moving in a radial direction after impinging on the heated surface. Again this video image shows promise for understanding the flow physics of the interaction of the spray and pedestal surface and should be further investigated.

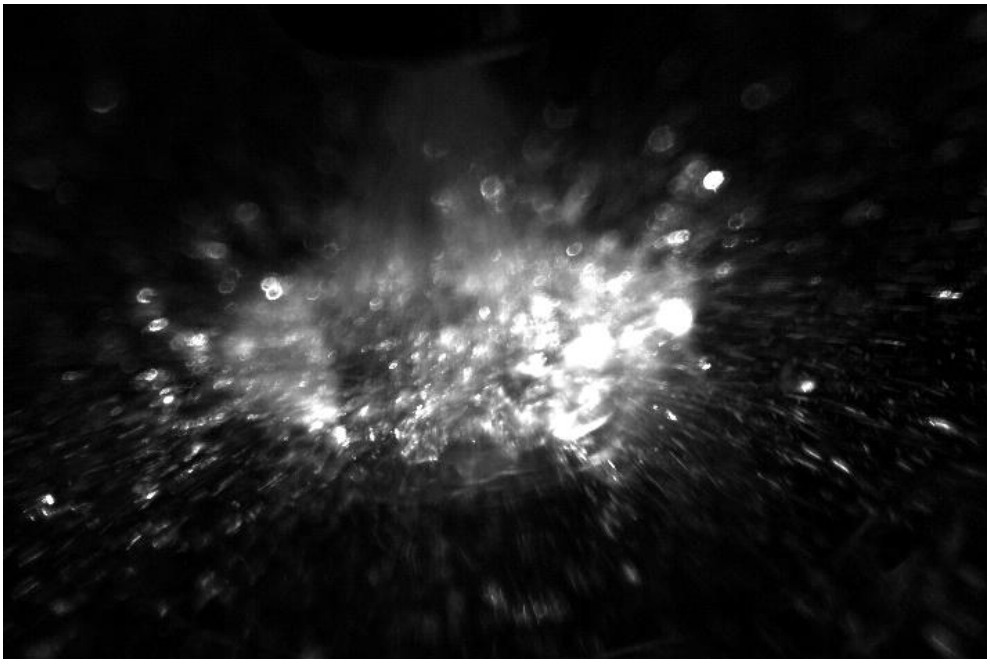

Figure 4.28: Interaction Between the Spray Droplets and the ITO Pedestal Heated Surface during a High Speed Camera at 1000 Frames Per Second

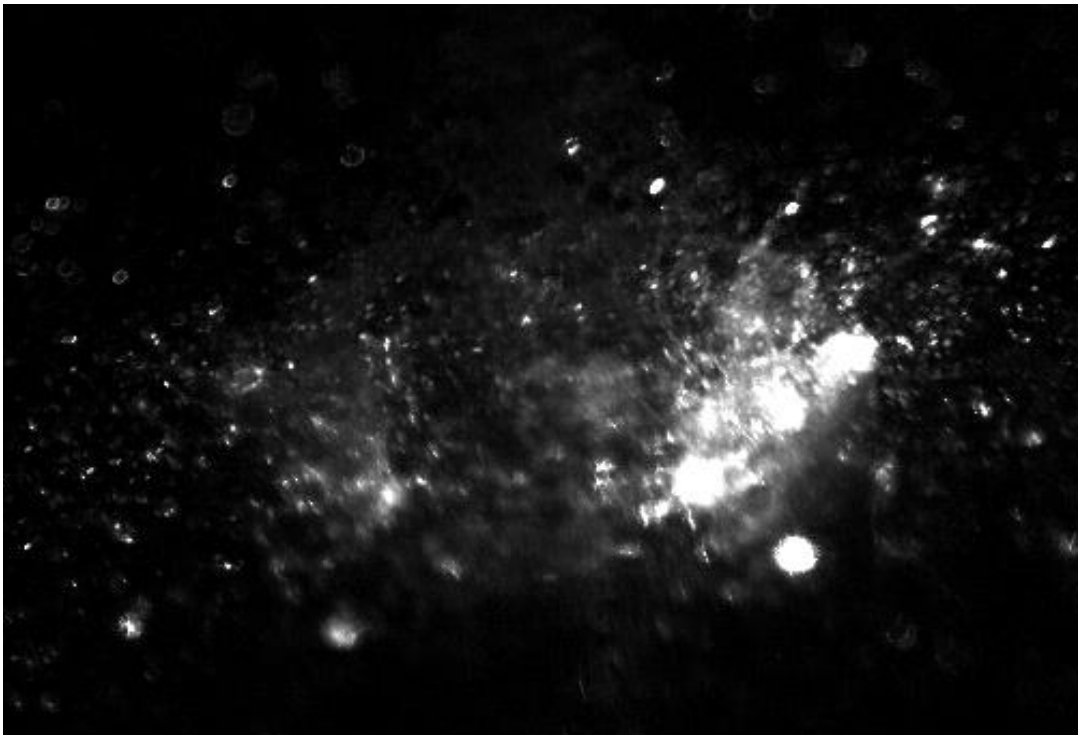

Figure 4.29: Sample Video Image of Spray Interaction with the ITO Pedestal in Terrestrial Gravity for a Flow Rate of 5.4 GPH

Figure 4.30 shows the interaction of the spray and heater surface using a high power laser and high speed camera viewing from below looking through the transparent pedestal and ITO heater. The heat flux is 17.11 W/cm^2 and the spray has a flow rate of 5.4 GPH. Figure 4.30 shows flooding with what appears to be some voids that might be vapor bubbles. As the spray impacted the pedestals heated surface the voids were observed to move in a radial direction, removing them from the surface.

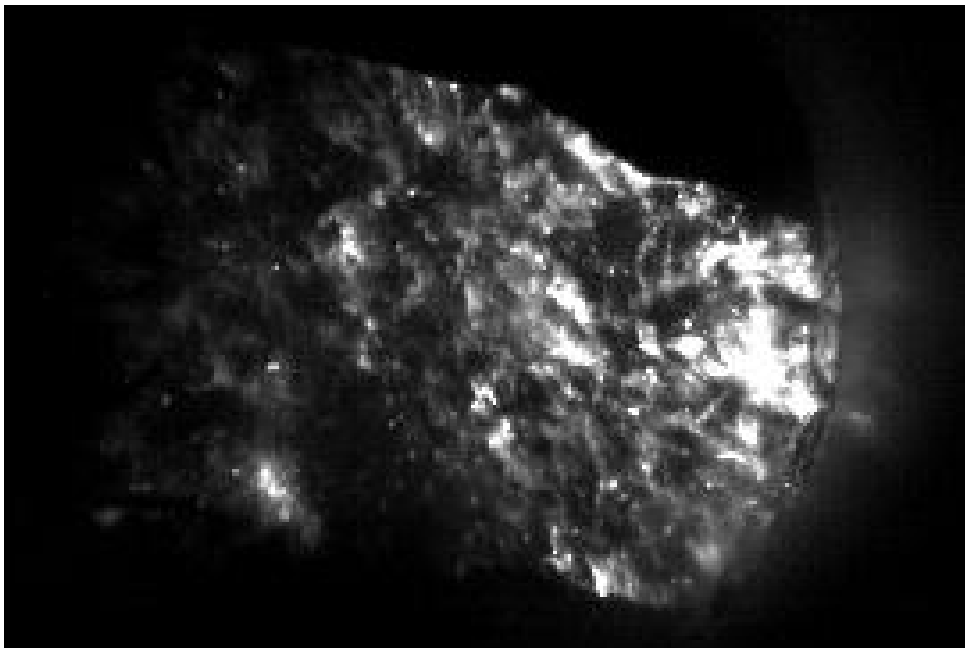

Figure 4.30: Sample Video image of the Spray and Heated Surface Interaction through the Bottom of the Pedestal using Special Optics and a High Speed Camera With Shutter Speed of 3,000 Frames Per Second

Figure 4.31 is a sample video image showing the bottom view, with the use of the high speed camera at 3,000 FPS, of the pedestal heated surface with a heat flux of 17.11 W/cm^2. Figure 4.31 shows many voids on the surface of the pedestal that will be removed by the spray motion in the radial direction after impingement. Figure 4.30 was taken just before Figure 4.31 which demonstrates that the spray has the ability to remove voids from the pedestal heated surface. These voids could possibly be FC-72 vapor bubbles that are removed from the spray. The use of the high speed camera has been shown to be a useful research tool and further investigation needs to be done.

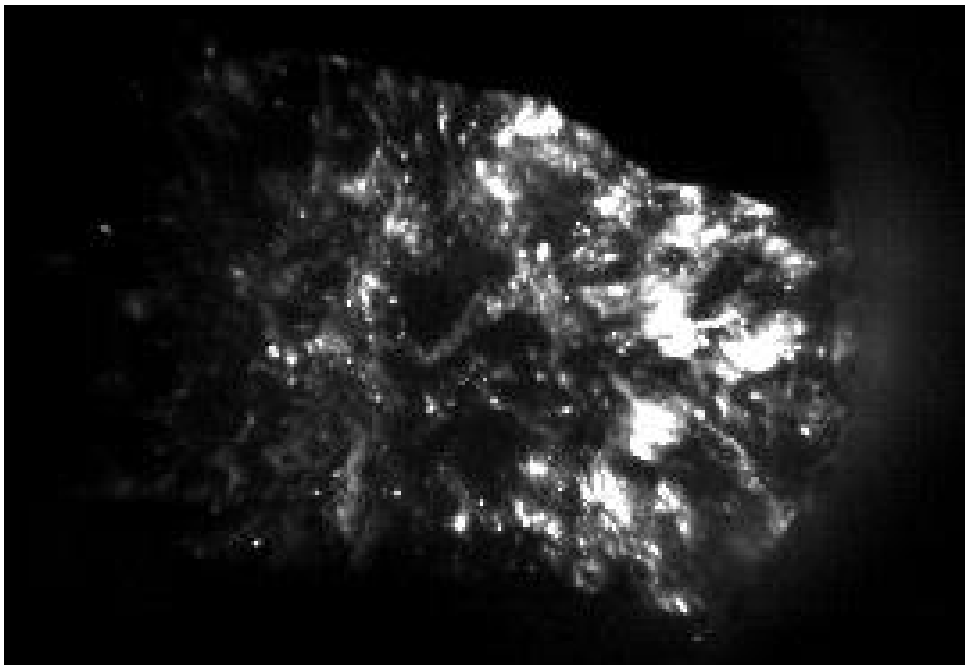

Figure 4.31: Photograph of the Pedestals Heated Surface from the bottom using Special Optics at a Flow Rate of 5.4 GPH and Heat Flux of 17.11 W/cm^2

CHAPTER 5 CONCLUSIONS AND RECOMMENDATIONS:

In this chapter, conclusions from the present research will be discussed and recommendations for future work will be made.

5.1 Conclusions:

The objective of this thesis has been to design and construct an apparatus to be used at West Virginia University to study evaporative spray cooling in both spray orientations, vertical and horizontal, and for high heat flux cooling applications. The apparatus design and construction has been described in Chapter 3, and the data collected were presented in Chapter 4.

The design and construction of the apparatus is always changing with the updates of the present research. With goals of the research changing, modifications may have to be made to alter the working system of the apparatus. The apparatus at this time does work efficiently, and it can be said that this portion of the objective has been successfully met.

Data collected and presented in Chapter 4 show a preliminary baseline set of results to help understand the effectiveness of spray cooling on high heat fluxes. Some comparisons were made to better understand the effects of spray cooling in vertical downward and horizontal sprays. Also, a comparison between the two different types of heaters was made and discussed to illustrate the importance of documenting the type of heater used.

The results show that the apparatus does function at a steady state and tends to be reliable under terrestrial gravity conditions. It has yet to be studied how the spray

chamber will act in simulated microgravity conditions such as the parabolic flights on the NASA DC-9.

A set of data was collected for both vertical downward spray and horizontal spray. Both sets of data showed similar overall trends; that is, as the heat flux increased so did the surface temperature. All curves for both the vertical and horizontal sprays show an S-type curve which resembles previous related spray cooling studies done by Tilton (1989) and Baysinger (2004), among others. One difference between the vertical and horizontal spray is that for the vertical spray at lower flow rates, there was more efficient cooling for the confined geometries. One explanation for this higher efficiency with the more confined geometries is recirculation or rebound of the spray droplets splashing off the pedestal in the radial direction and striking the cap. After impinging on the cap, the spray droplets will tend to reflect back onto the heated surface.

A comparison study for both the vertical and horizontal spray was completed that showed, for most cases, that vertical spray was more efficient than the horizontal spray. Previous work done by Kato et al. (1994) showed that spray cooling for horizontal sprays was more efficient than the vertical downward sprays. At this time there is no explanation for this discrepancy between the previous work and the present results other than the working fluid was different. Another probable cause for the discrepancy could be the difference in plumbing between the spray chamber and sump pump for the two different spray orientations. The difference in plumbing would create a change in head loss, and since the sump pump runs at a constant RPM (Revolutions per Minute), this would cause the spray chamber to be at different vacuum pressures. These different vacuum pressures would change the values of thermodynamic properties for the working

fluid (FC-72) in the chamber and vaporization would occur at different heating levels for the pedestal.

Another comparison was made between the ITO and ceramic TFR heaters, as presented in Chapter 4. The two different types of heaters produced different cooling efficiencies at identical heat fluxes. Reasons for this could be due to the amount of high-temperature epoxy that was used to connect the electrodes to the heater surfaces. Other possible explanations for the differences could be the fact that the heaters vary in thickness and different types of glue were used to attach them to the pedestal.

The computed heat transfer coefficients increased as the spray flow rate was increased, and tended to be relatively constant versus heat flux. These heat transfer coefficients ranged from approximately 4500 to 7500 W/m^2K.

Preliminary flow visualizations were studied with the use of laser light sheet illumination to show spray droplet characteristics and interaction with the vaporization on the pedestals heated surface. The high speed camera was used at various angles including looking through the bottom of the transparent pedestal and heater. Each angle showed promising results in understanding either the spray flow physics or the interaction between the spray droplets and vaporization on the pedestals heated surface.

5.2 Recommendations:

The following recommendations have been made based on the results of the present study.

After many hours of collecting data manually, one recommendation is to install an adequate data acquisition board which will acquire all the temperature and pressure data

in the pedestal and chamber at a selected sampling rate. Use of a data acquisition board allows one to be confident that the temperatures are steady by the large amount of data points and more importantly will cut the time it takes to collect the data.

Another item that needs to be investigated would be to vary the amount of sub-cooling systematically. This experiment used a large amount of sub-cooling which is why portions of the x-axes of the figures in Chapter 4 are negative. By decreasing the sub-cooling the spray liquid would reach its saturation point, perhaps causing boiling and vapor to form at lower liquid flow rates or heat fluxes. This would be beneficial for this research, and a pre-heater should be installed just before the fluid enters the spray chamber to enable independent control of the sub-cooling. The pre-heater would benefit the flow visualization because increasing the liquid temperature would likely enhance the interaction between spray droplets and vapor bubbles formed from the pedestals heat source.

Also, the heat loss down the glass pedestal needs to be accounted for. Baysinger (2004) found this correction to generally be between 1% and 3% of the total heat produced by the heater. This correction was not made in the present work, but should be added in future studies.

Working at lower flow rates seemed to be beneficial for different reasons during the research. Lower flow rates seem to help the performance for flow visualizations and for different confinement geometries. To achieve lower flow rates with this apparatus, one should install a variable speed pump for the sump. The diaphragm pump seems to handle the liquid vapor mixture well but controlling the flow rates is tedious. This is partly because the sump pump motor operates at a constant RPM. The rotameter does a

good job, but at flow rates below 6 GPH (FC-72), the system tends to get a lot of air/FC-72 vapor bubbles in the return flow from the sump to the FC-72 reservoir. It is believed that the sump pump is driving the entire system pressure and is causing more air/FC-72 vapor to be removed from the chamber than the nozzle is spraying. By being able to turn the suction down lower on the sump pump, the nozzle and sump could be adjusted to have the same driving pressure, and the system should behave more normally.

Also new rotameters should be purchased for the water flow loop as it needs to be run at a higher flow rate in order to maintain the chamber at a constant temperature. The chamber temperature should be kept below the saturation temperature of the working fluid.

Another component that would help the user with the apparatus would be a pressure bleed off needle valve for the accumulator. This pressure bleed off valve, once set to the correct pressure, would allow the user to operate the system without having to manually remove the air/FC-72 vapor mixture. This would help the user spend more time studying the flow and heat transfer phenomena that occur inside the spray chamber.

This research collected a preliminary set of baseline performance data for the apparatus, and much more work needs to be done. Future work needs to investigate the use of EHD (Electro-hydrodynamics) to enhance the efficiency of spray cooling. EHD could prove to be extremely beneficial for spray cooling and its potential use for cooling of high powered heat sources in microgravity conditions. Also additional work needs to be done with flow visualization to better understand the interaction between the impinging spray droplets and the vapor bubbles formed on the heated surface.

Additional work also needs to involve simulated microgravity using the NASA DC-9 performing parabolic flight paths. This would simulate microgravity more accurately than rotating the spray orientation from vertical to horizontal. Studies of the effectiveness of spray cooling with and without the enhancement of Electro-hydrodynamics in microgravity need to be determined. The study of the effectiveness of the Coulomb force produced by the use of an electrode to charge the spray needs to be investigated in both microgravity and terrestrial gravity conditions.

Another recommendation would to be installing a small siphon so that a small specimen of the working liquid could be extracted for testing. One would want to measure a property of the liquid, for example specific weight, before installing in the apparatus to compare with the extracted specimen for contamination of the working liquid.

REFERENCES:

Baysinger, K., Yerkes, K., Michalak, T. E., Harris, R., McQuillen, J., "Design of a Microgravity spray cooling experiment," *42nd AIAA Aerospace Sciences Conference and Exhibit,* 2004.

Baysinger, K., "Experimental testing and numerical modeling of spray cooling under terrestrial gravity conditions," *Thesis*, Wright State University, Dayton, OH, 2004.

Chow, L., Sebmbey, M., Pais, M., "High heat flux spray cooling," *Annual Review of Heat Transfer*, pgs 291-318, 1997.

Jones, T., "Electrohydrodynamically enhanced heat transfer in liquids- a review," *Advances In Heat Transfer*, Vol 14, pgs 107-148, 1978.

Kato, M., Abe, Y., Mori, Y., Nagashima, A., "Spray cooling characteristics under reduced gravity,"*Journal of Thermophysics,* Vol 9, No 2, Technical Notes, pgs 378-381, 1994.

Labus, T., "Liquid jet impingement normal to a disk in zero gravity," *NASA Technical Paper 1017*, August 1997.

Law, S., "Embedded-electrode electrostatic-induction spray-charging nozzle: Theoretical and engineering design," *American Society of Agricultural Engineers, Transactions of the ASAE,* pgs 1096-1104, 1978.

Lee, H., Merte, H. "Pool boiling mechanisms in microgravity," Proceedings of the Eng. Foundation Conf on *Microgravity Fluid Physics and Heat Transfer*, Hawaii, Ed Dhir,V.K., 1999.

Lin, L., Ponnappan, R., "Heat transfer characteristics of spray cooling in a closed loop," *International Journal of Heat and Mass Transfer 46,* pgs 3737-3746, 2003.

Rohsenow, W. M., "Boiling," *Handbook of Heat Transfer Fundamentals*, 2nd Ed., McGraw-Hill, New York, 1985.

Straub, J., "Boiling heat transfer and bubble dynamics in microgravity," *Advances In Heat Transfer*, Vol 35, pgs 57-172, 2001.

Takahashi, K., Yabe, A., Maki, H., "Electrohydrodynamical (EHD) Research of Saturated Pool Building Heat Transfer—Critical Heat Flux on Small Scale Surface and Measurements by Capacitance Probe," *Tenth International Heat Transfer Conference*, pgs 5153-5158, 1997.

Tilton, D., "Spray Cooling," *Dissertation*, University of Kentucky, Lexington, KY, 1989.

Webb, B., Ma, C., "Single-phase liquid jet impingement heat transfer," *Advances In Heat Transfer*, Vol 26, pgs 105-217, 1992.

Wolf, D., Incropera, F., Viskanta, R., "Jet impingement boiling," *Advance In Heat Transfer*, Vol 23, pgs 1-133, 1993.

Yabe, A., Lguchi, M., Taketani, T., Kikuchi, K., "Augmentation Mechanism of Burnout Heat Flux by Applying Electric Fields," *1st Report: Latent Heat Flux and Its Enhancements by Electric Fields*, *ASME/ JSME Thermal Engineering Joint Conference*, pgs 417-424, 1987.

Yagoobi, J., Bryan, J., "Enhancement of Heat Transfer and Mass Transport in Single-Phase Flows with Electrohydrodynamics," *Advances IN Heat Transfer*, Vol 33, pgs 95-186, 1999.

Yoshida, K., Abe, Y., Oka, T., Mori, Y., Nagashima, A., "Spray cooling under reduced gravity conditions," *Journal of Heat Transfer Vol 123*, pgs 309-318, 2001.

APPENDIX A : THERMOCOUPLE CALIBRATION

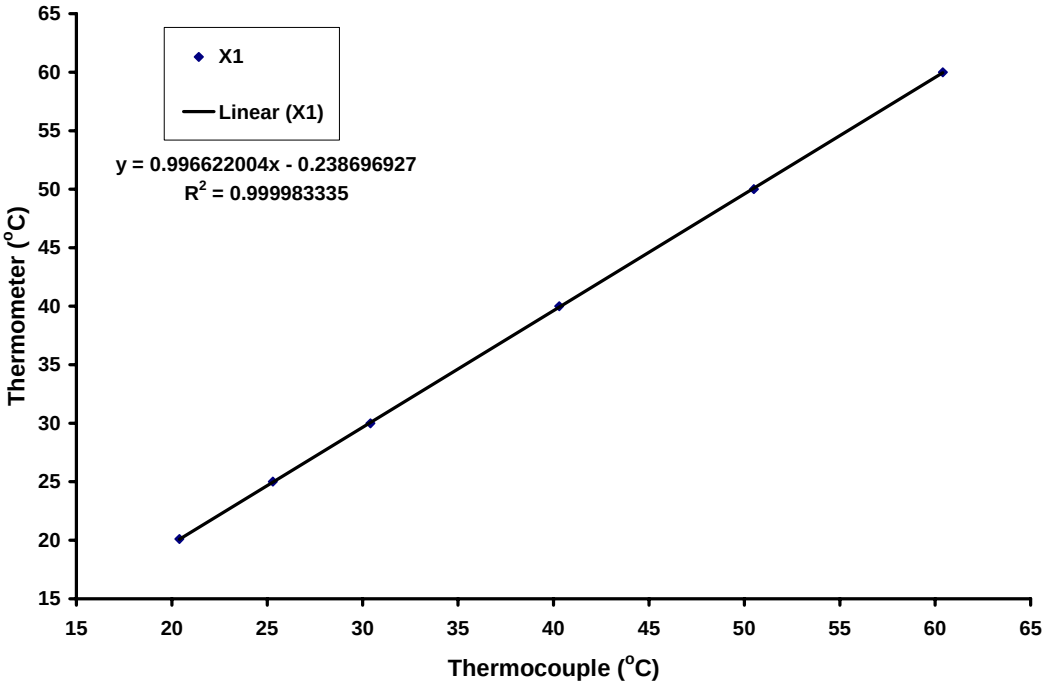

Figure A.1: Calibration Curve for Thermocouple X_1

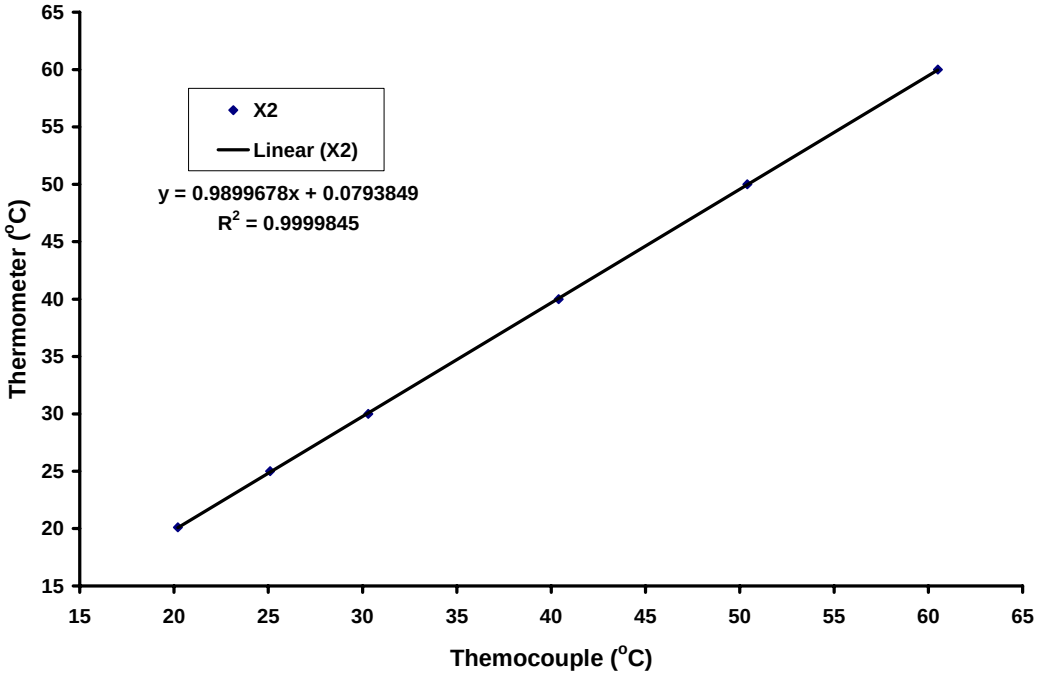

Figure A.2: Calibration Curve for Thermocouple X_2

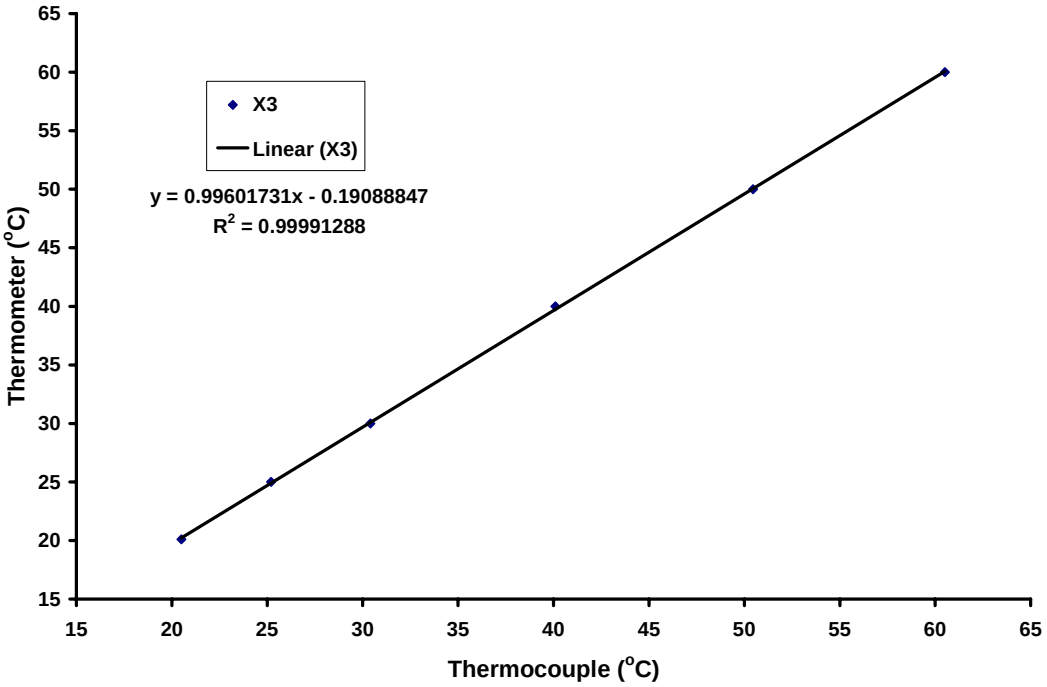

Figure A.3: Calibration Curve for Thermocouple X_3

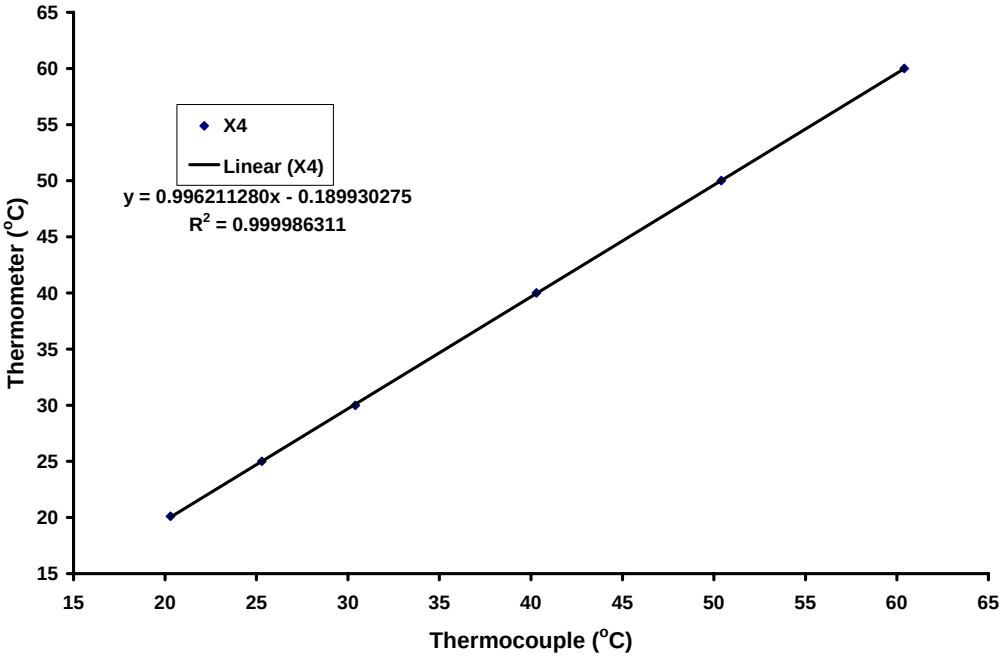

Figure A.4: Calibration Curve for Thermocouple X_4

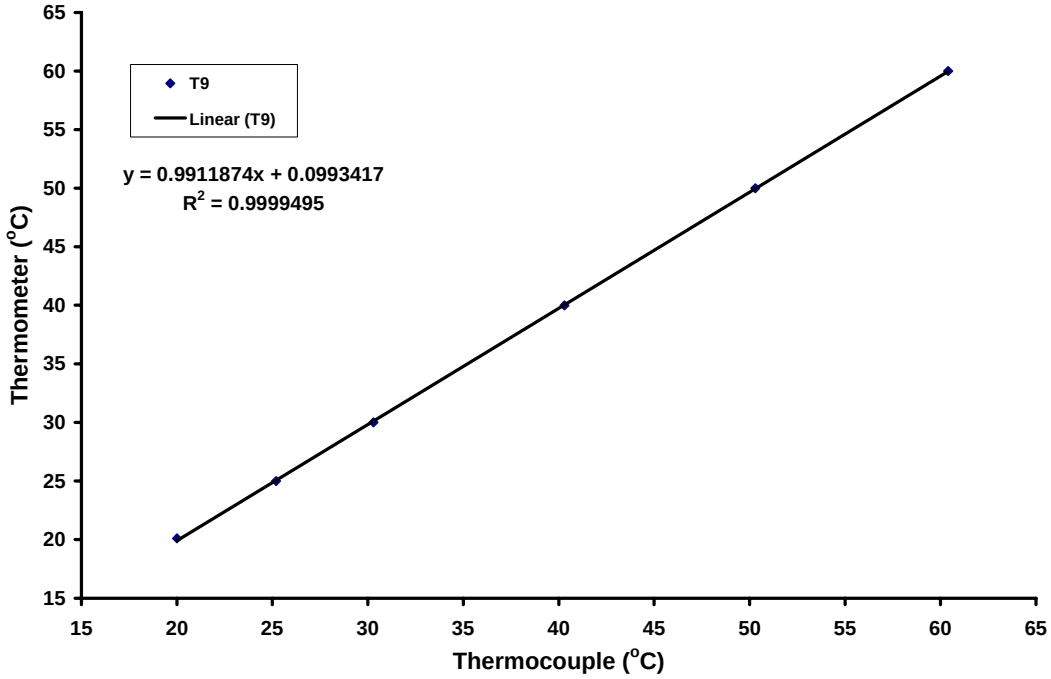

Figure A.5: Calibration Curve for Thermocouple T_9

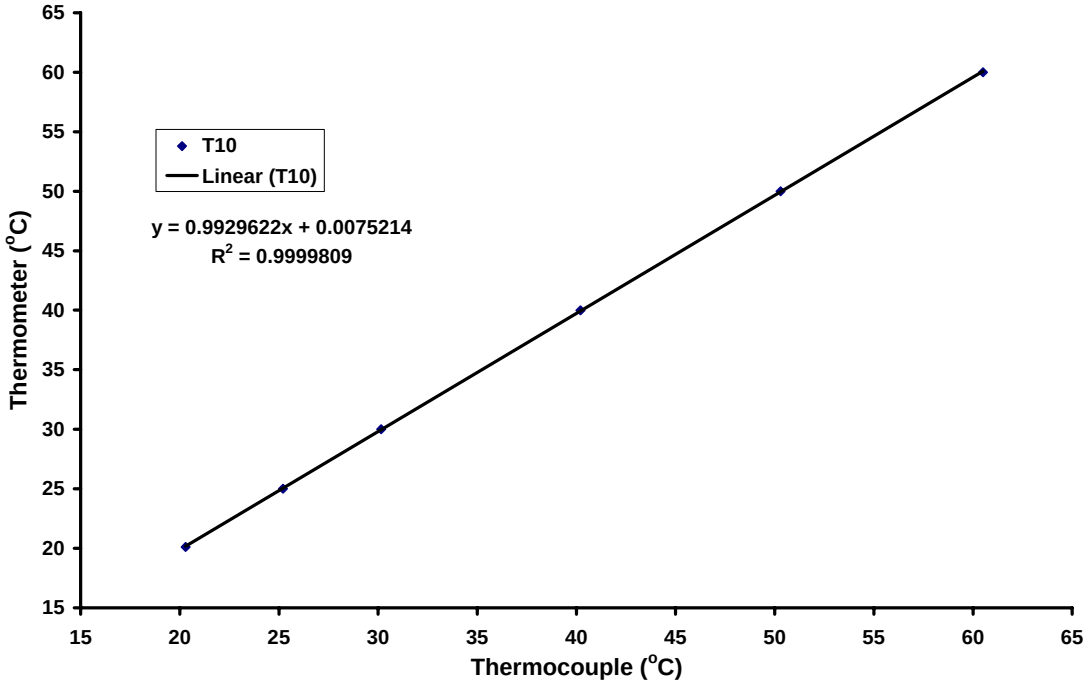

Figure A.6: Calibration Curve for Thermocouple T_{10}

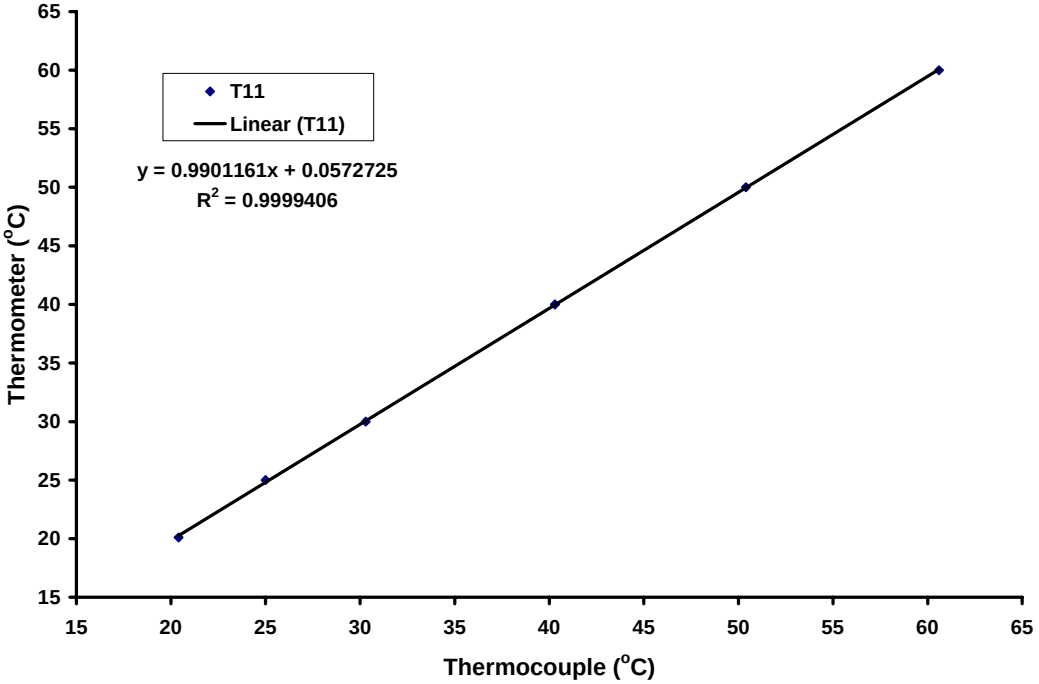

Figure A.7: Calibration Curve for Thermocouple T_{11}

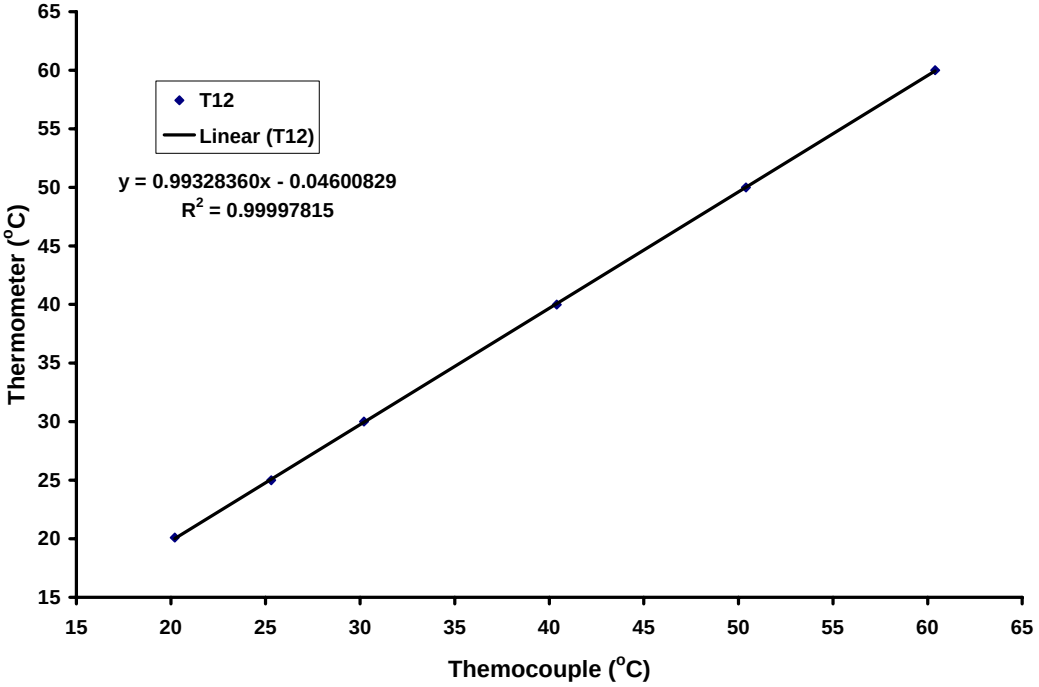

Figure A.8: Calibration Curve for Thermocouple T_{12}

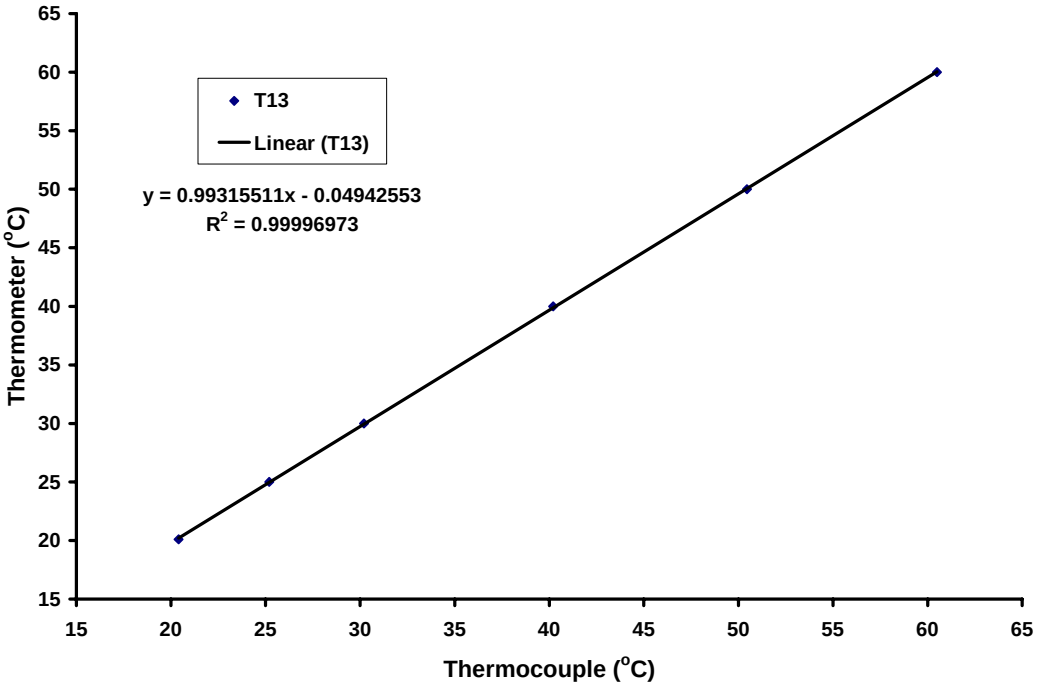

Figure A.9: Calibration Curve for Thermocouple T_{13}

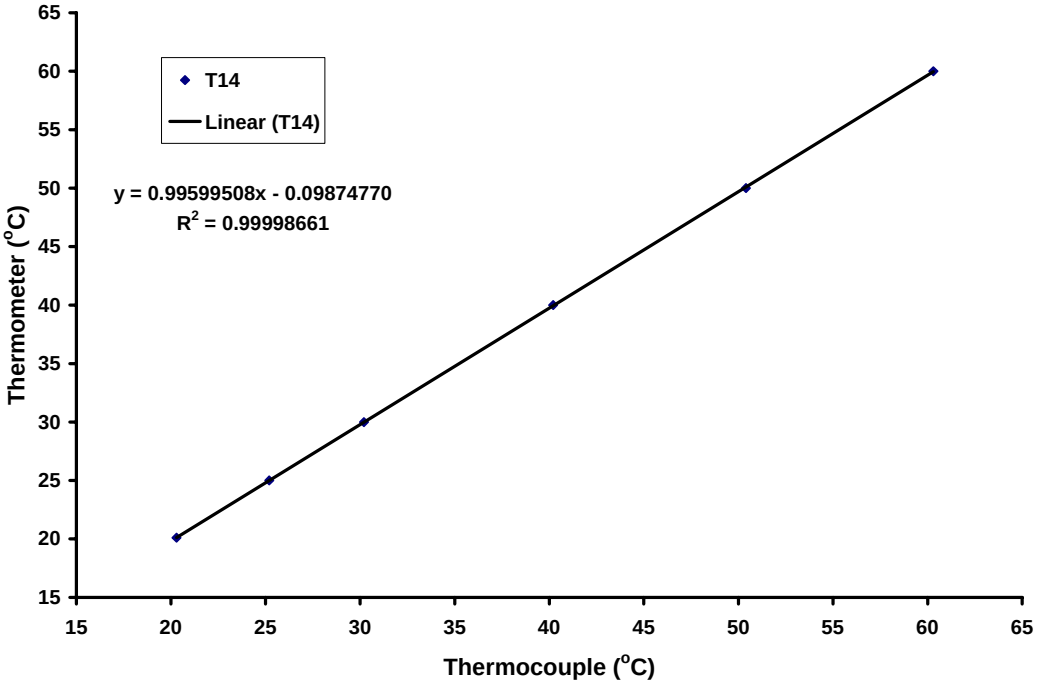

Figure A.10: Calibration Curve for Thermocouple T_{14}

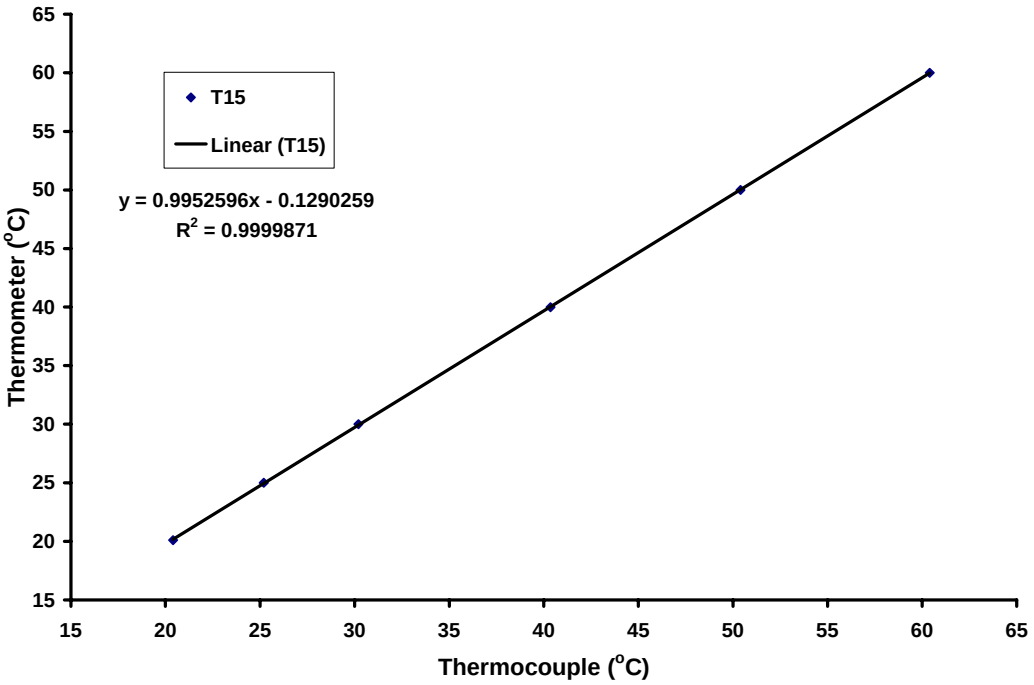

Figure A.11: Calibration Curve for Thermocouple T_{15}

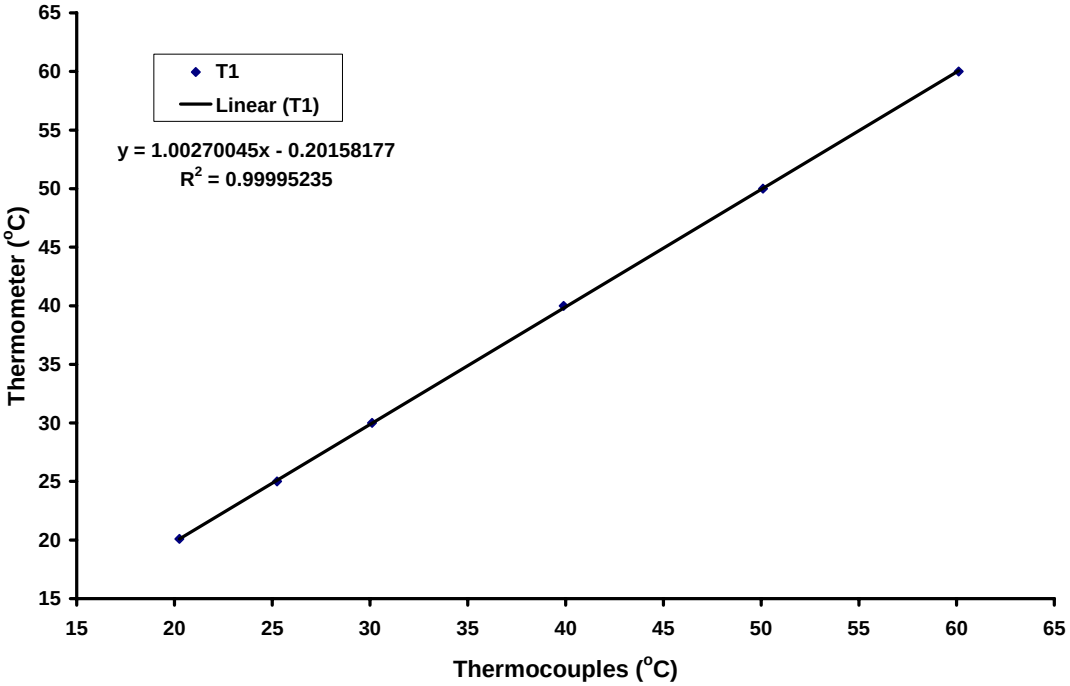

Figure A.12: Calibration Curve for TFR Pedestal Thermocouple T_1

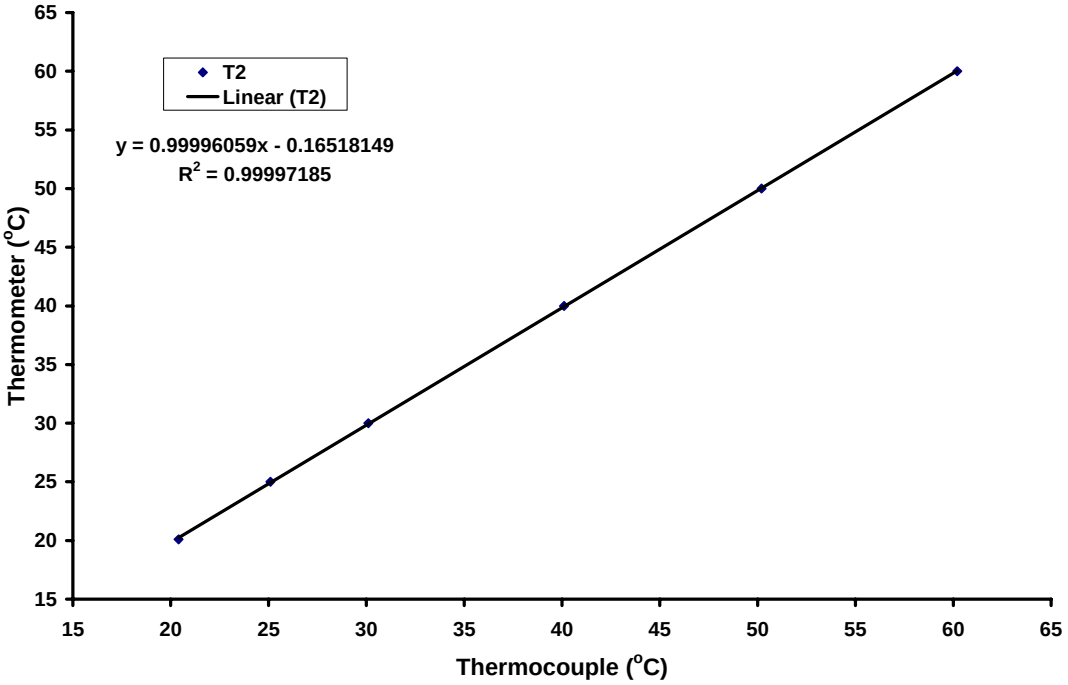

Figure A.13: Calibration Curve for TFR Pedestal Thermocouple T_2

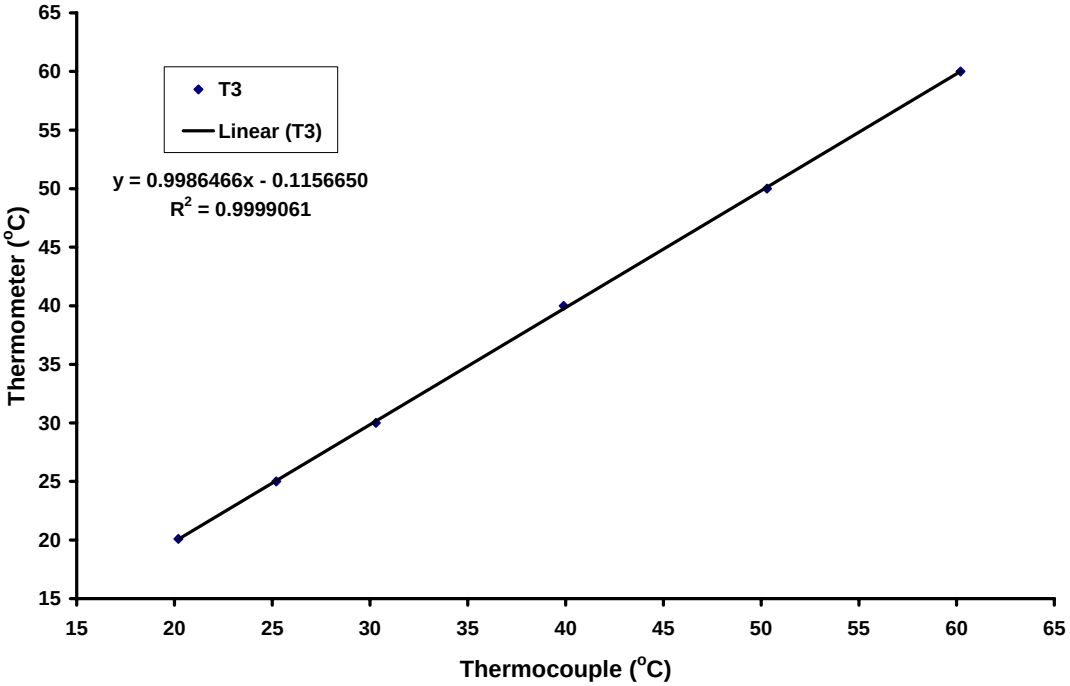

Figure A.14: Calibration Curve for TFR Pedestal Thermocouple T_3

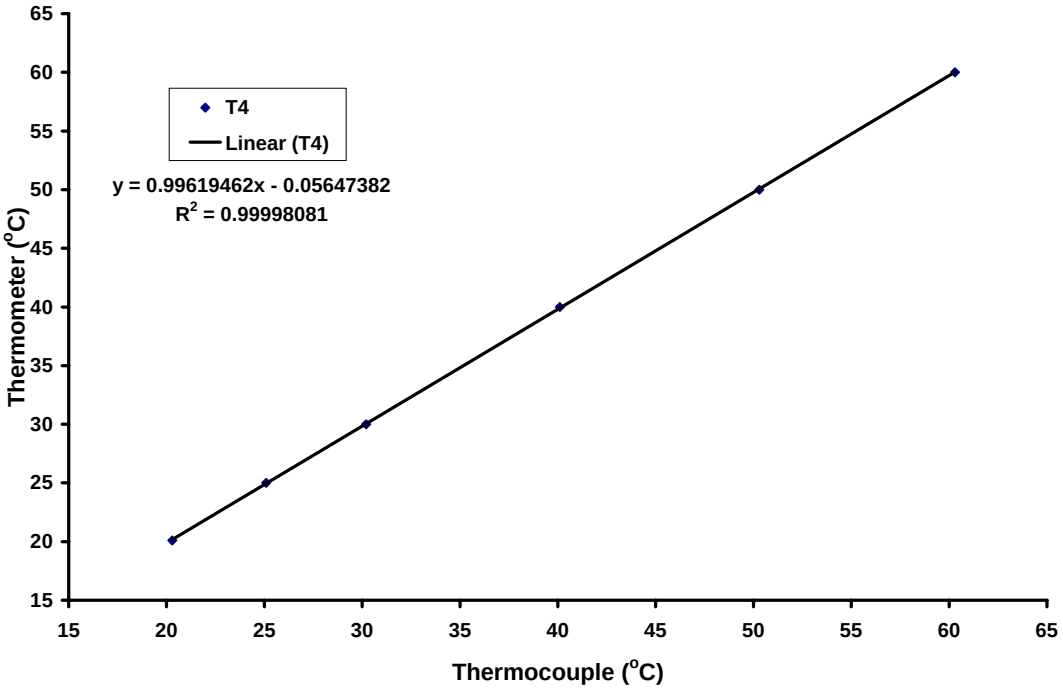

Figure A.15: Calibration Curve for TFR Pedestal Thermocouple T_4

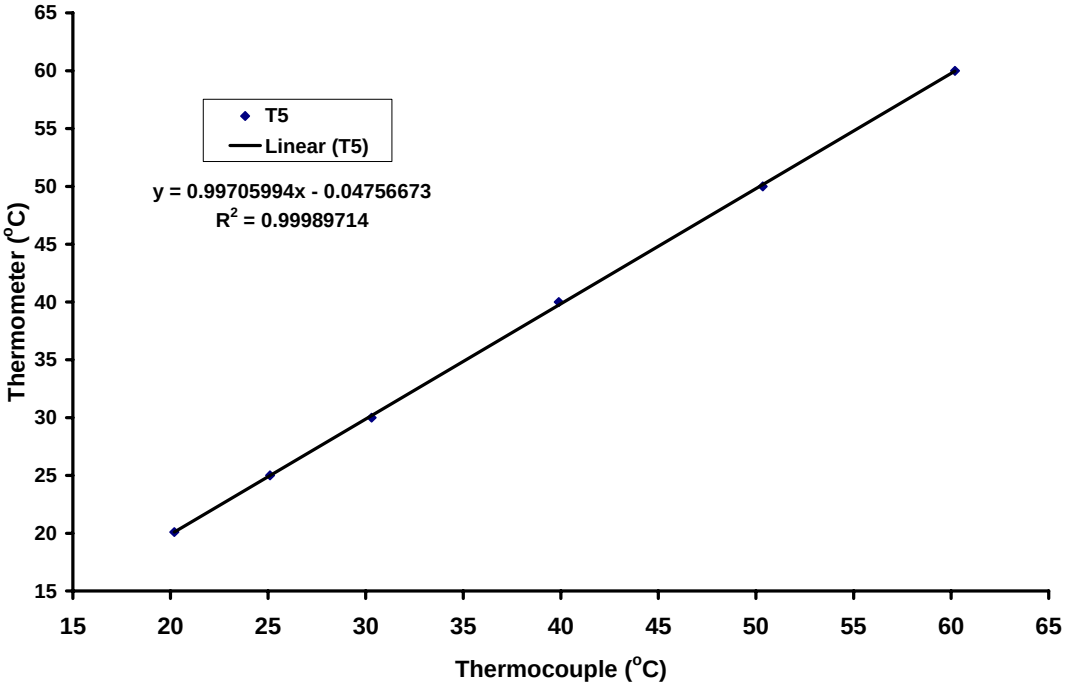

Figure A.16: Calibration Curve for TFR Pedestal Thermocouple T_5

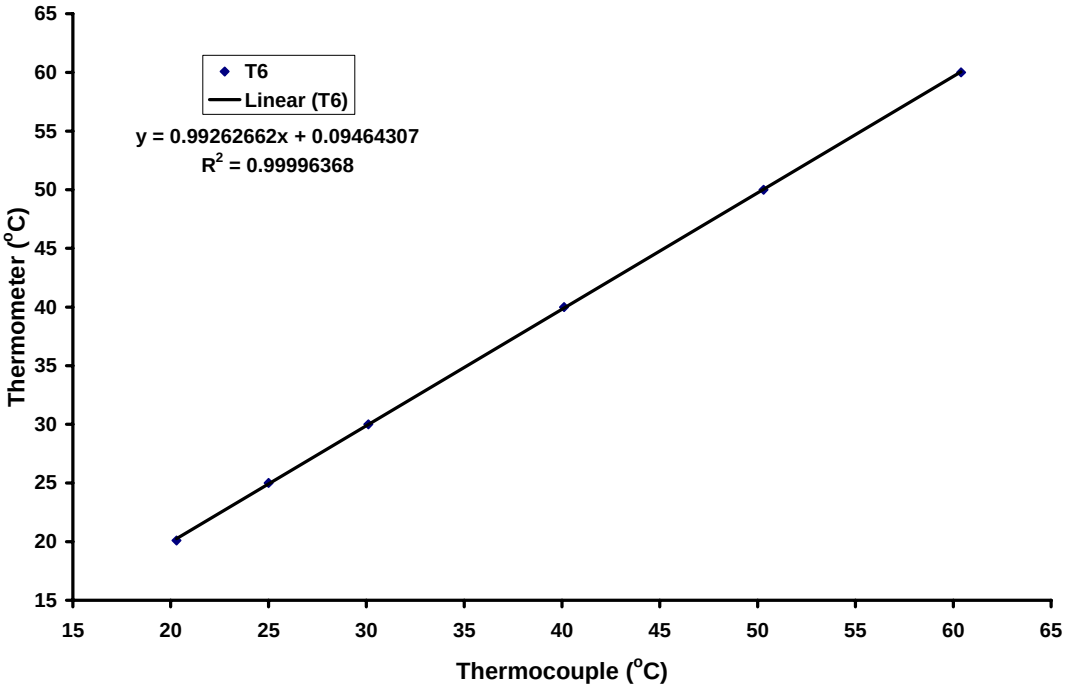

Figure A.17: Calibration Curve for TFR Pedestal Thermocouple T_6

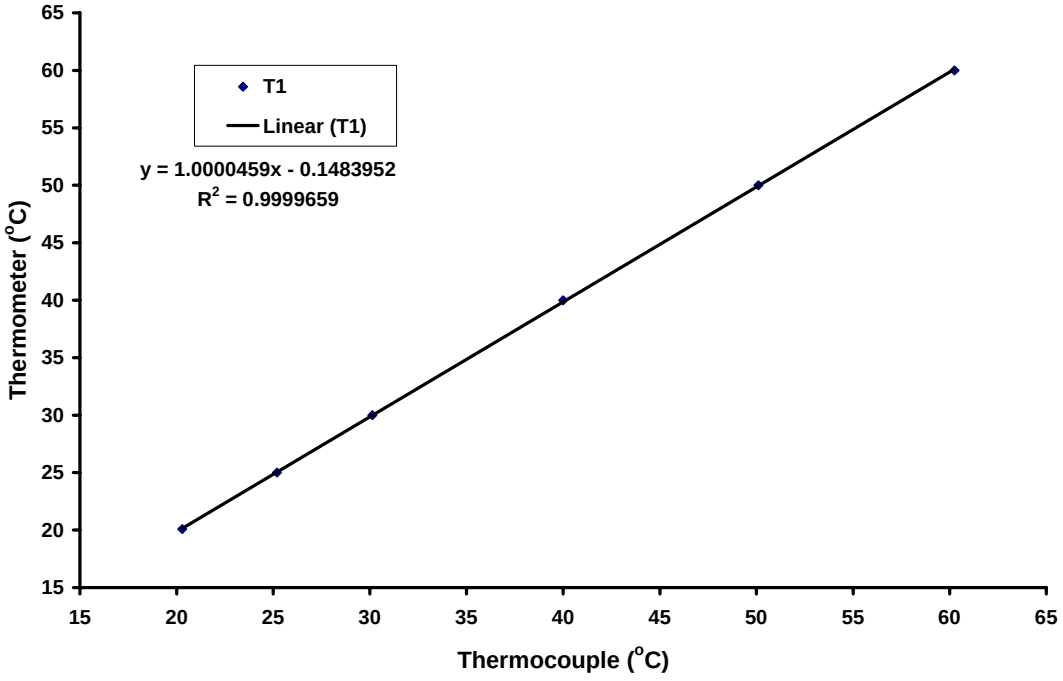

Figure A.18: Calibration Curve for ITO #1 Pedestal Thermocouple T_1

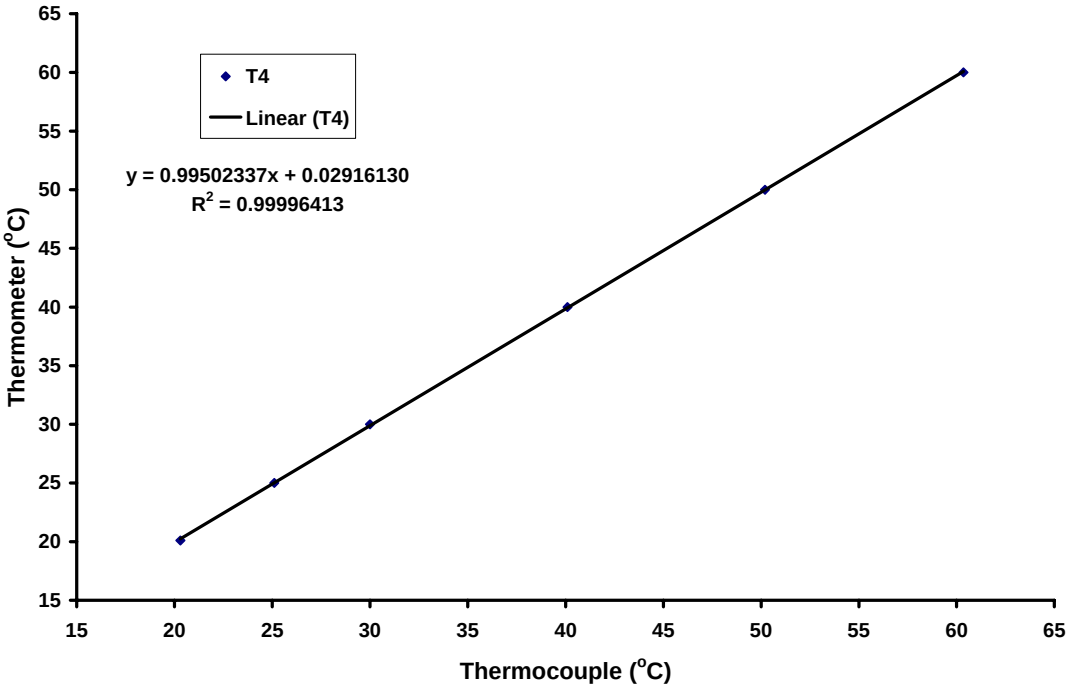

Figure A.19: Calibration Curve for ITO #1 Pedestal Thermocouple T_4

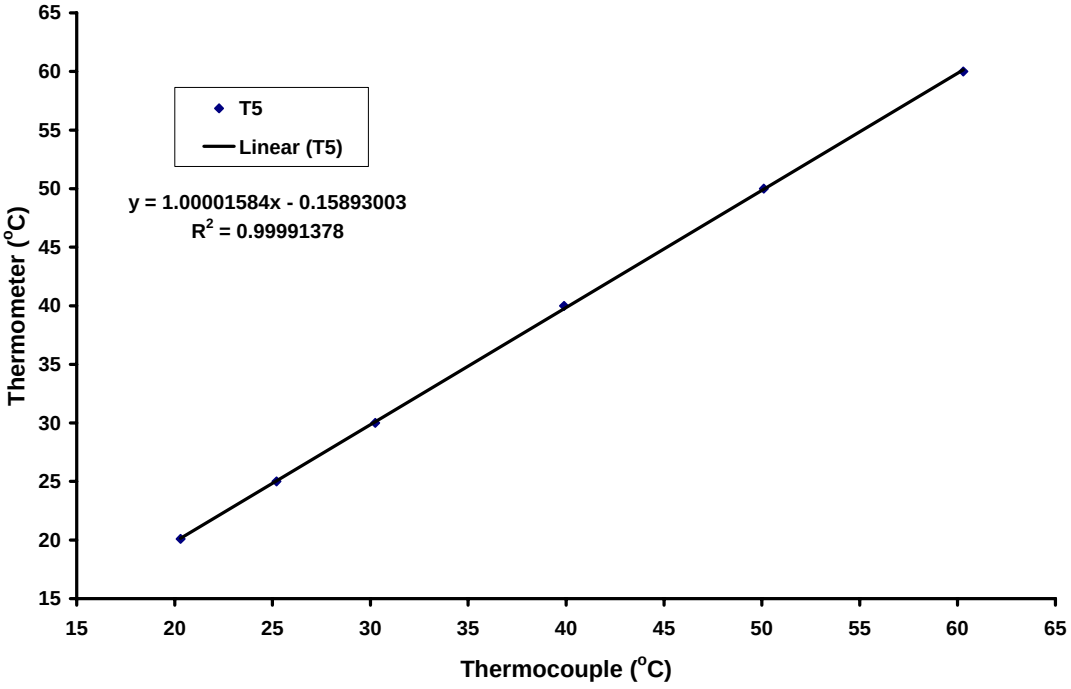

Figure A.20: Calibration Curve for ITO #1 Pedestal Thermocouple T_5

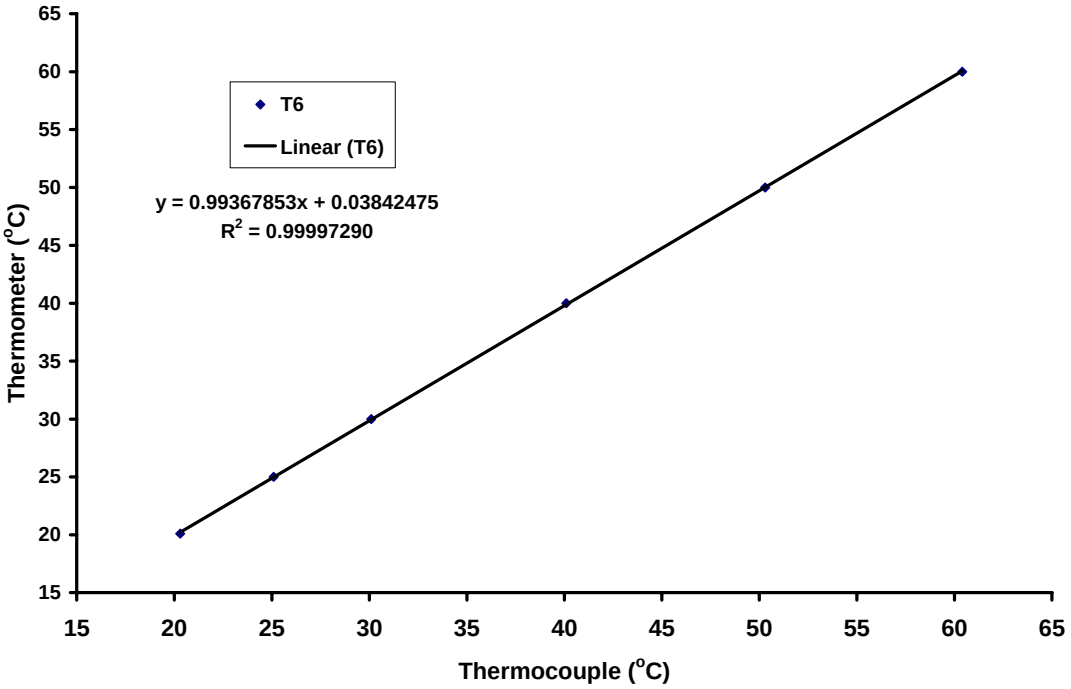

Figure A.21: Calibration Curve for ITO #1Pedestal Thermocouple T_6

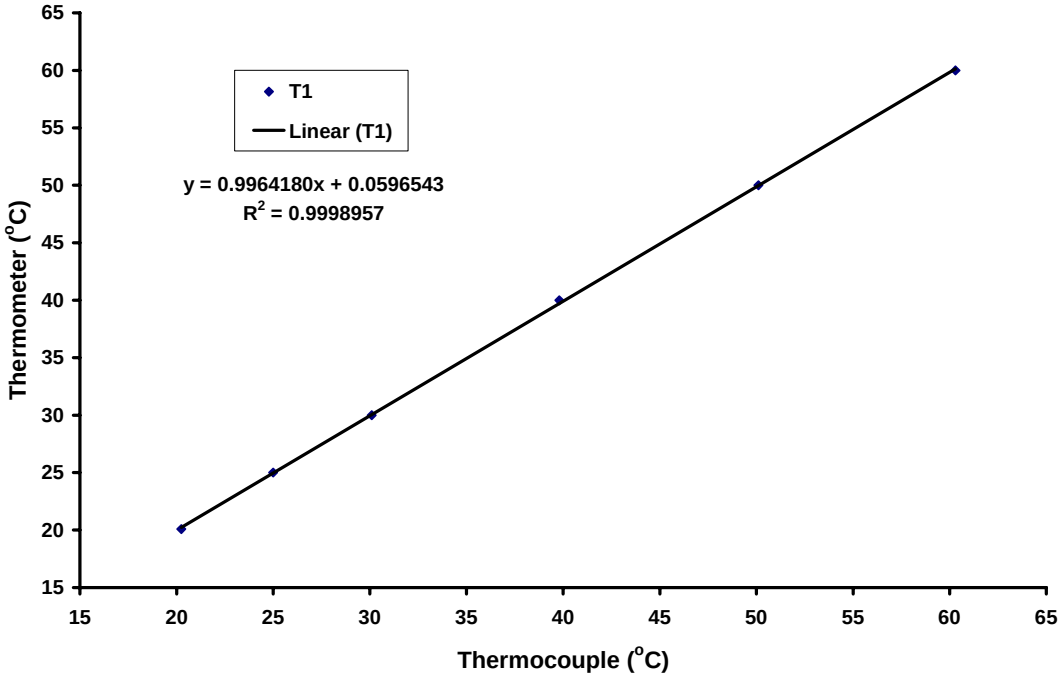

Figure A.22: Calibration Curve for ITO A Pedestal Thermocouple T_1

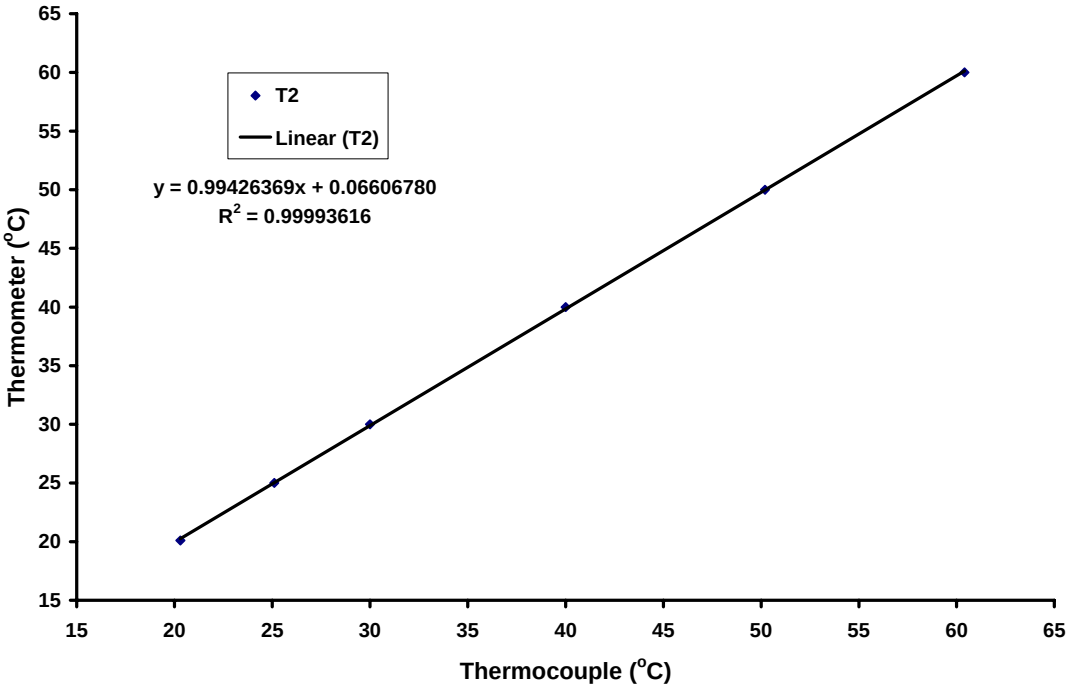

Figure A.23: Calibration Curve for ITO A Pedestal Thermocouple T_2

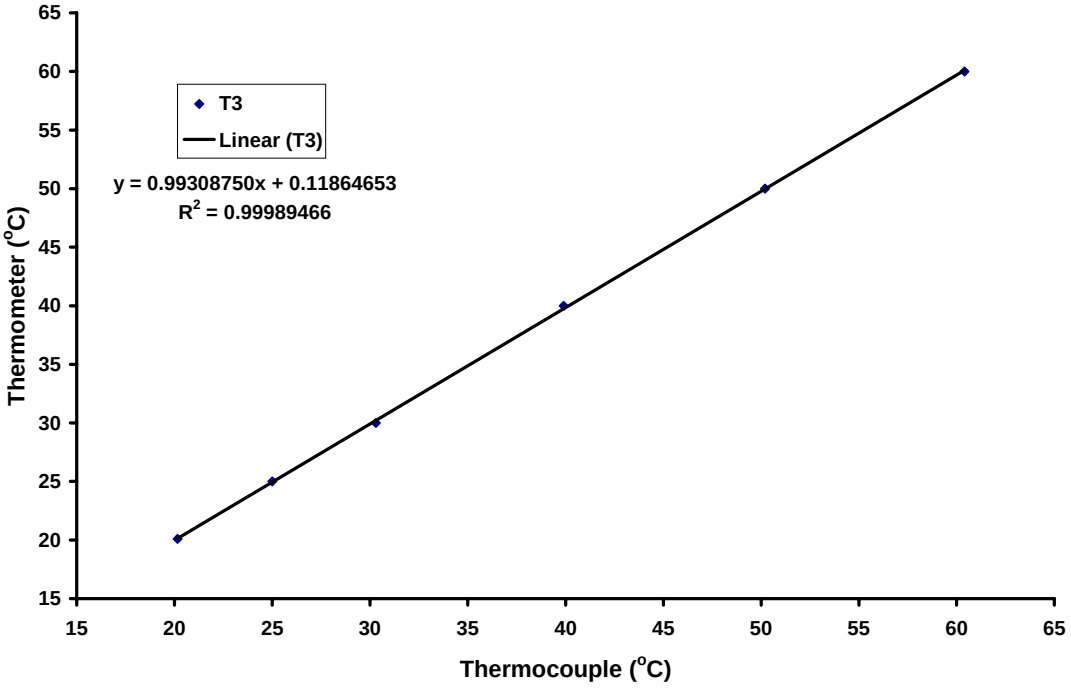

Figure A.24: Calibration Curve for ITO A Pedestal Thermocouple T_3

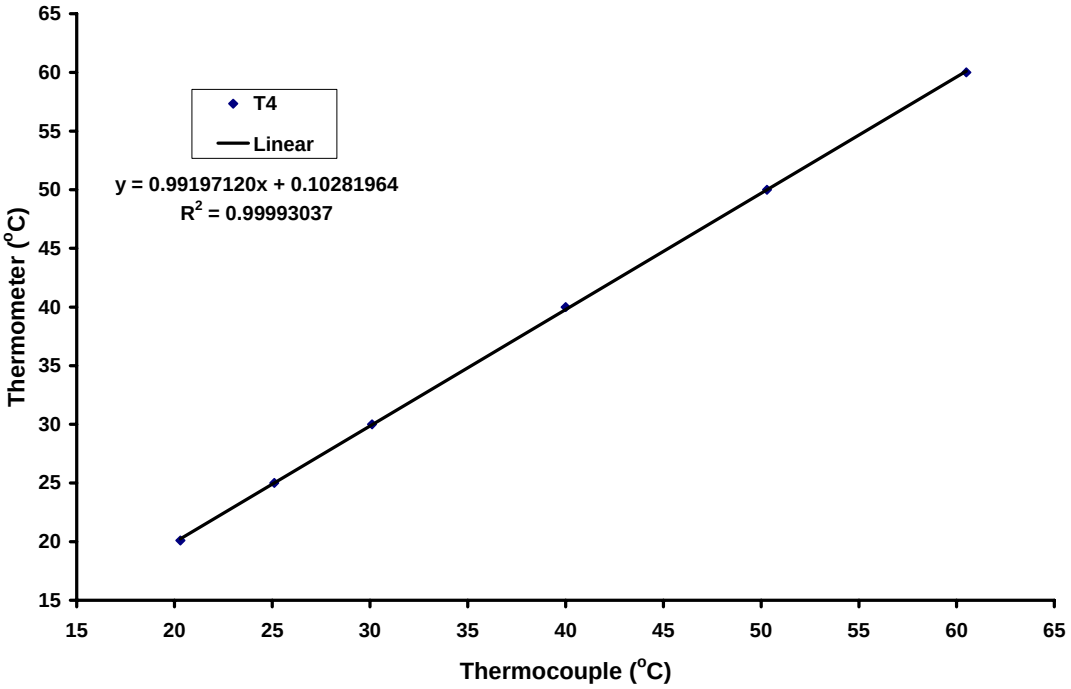

Figure A.25: Calibration Curve for ITO A Pedestal Thermocouple T_4

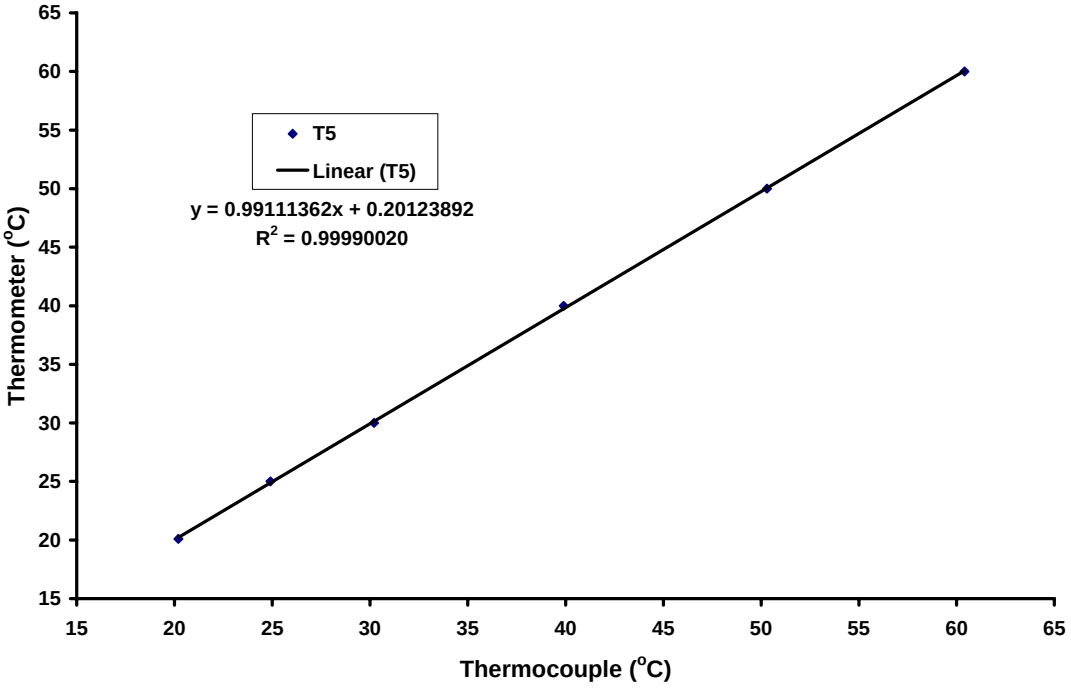

Figure A.26: Calibration Curve for ITO A Pedestal Thermocouple T_5

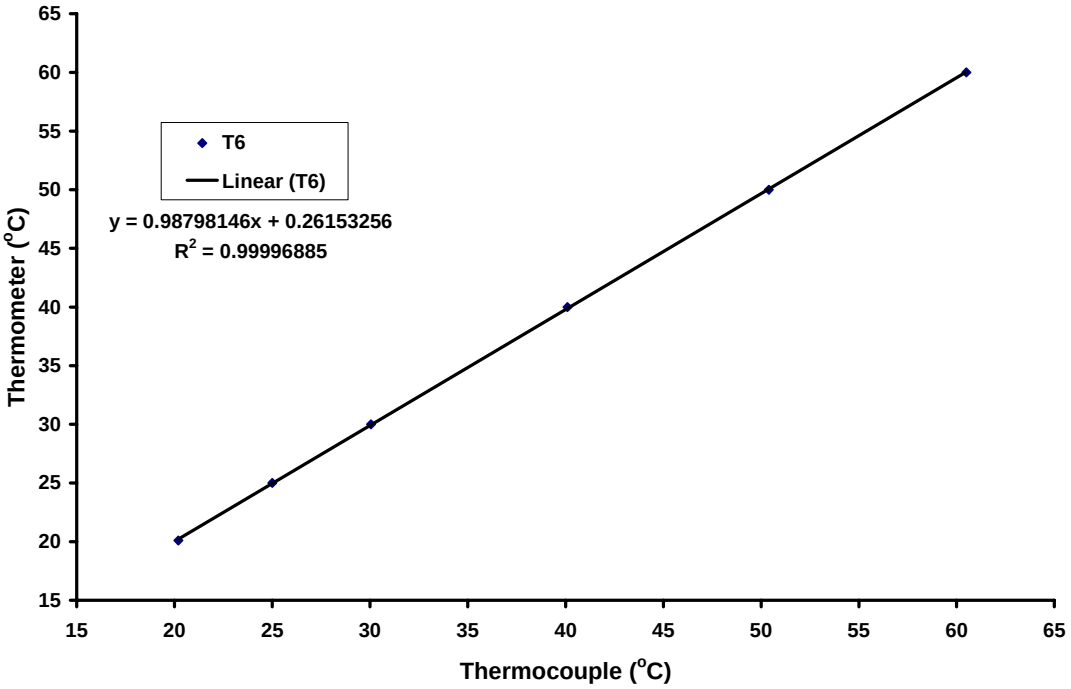

Figure A.27: Calibration Curve for ITO A Pedestal Thermocouple T_6

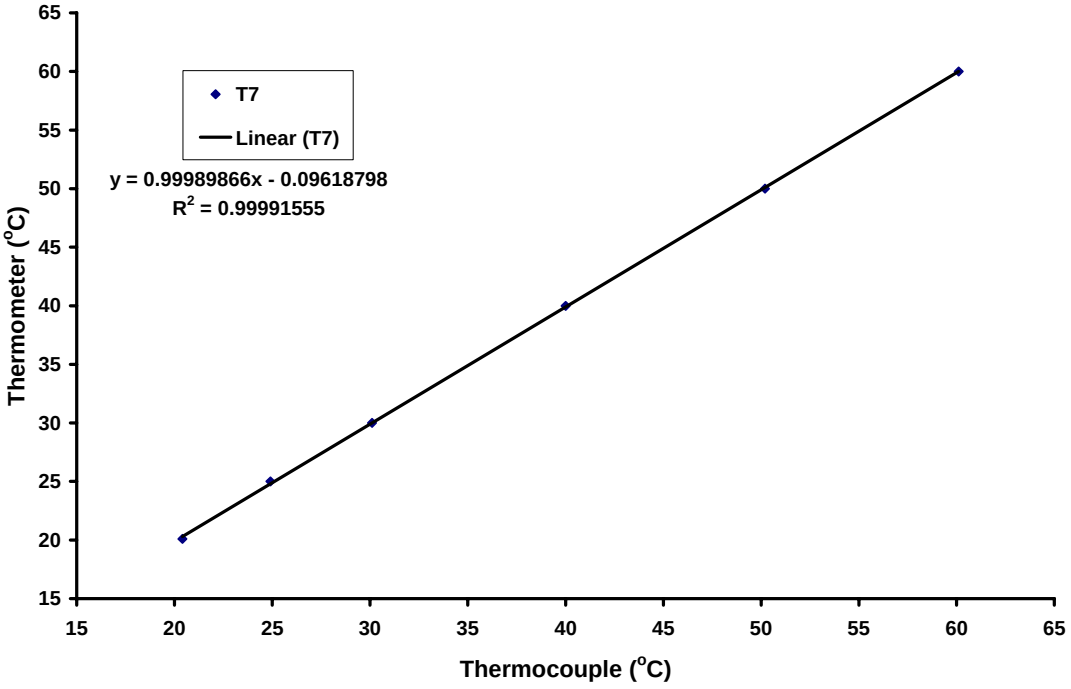

Figure A.28: Calibration Curve for ITO A Pedestal Thermocouple T_7

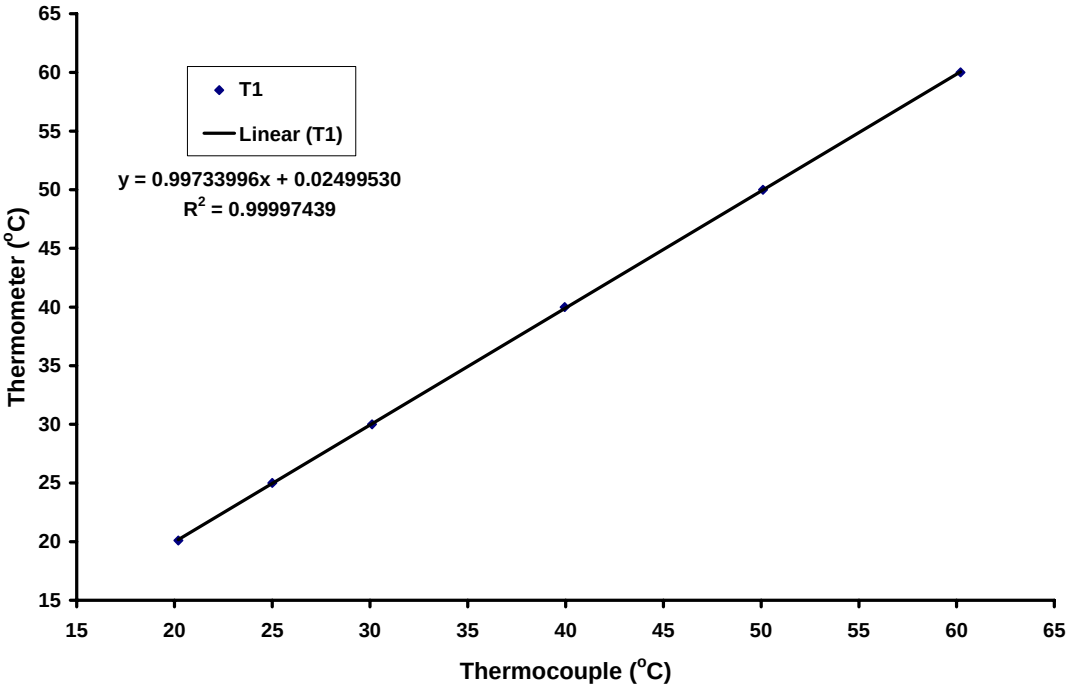

Figure A.29: Calibration Curve for ITO #2 Pedestal Thermocouple T_1

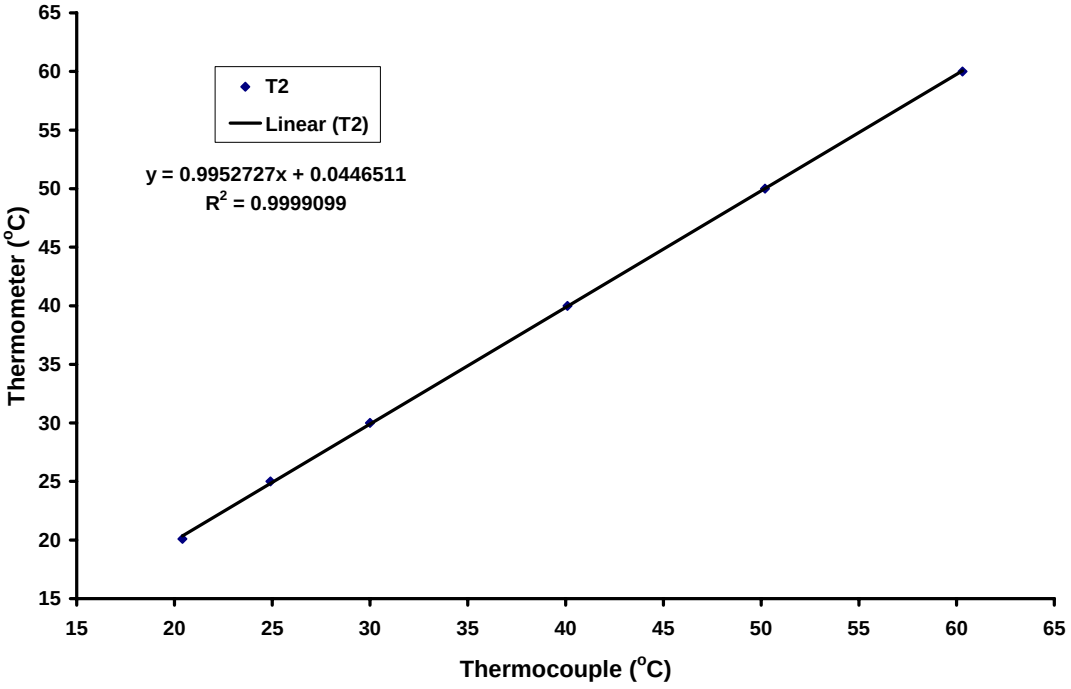

Figure A.30: Calibration Curve for ITO #2 Pedestal Thermocouple T_2

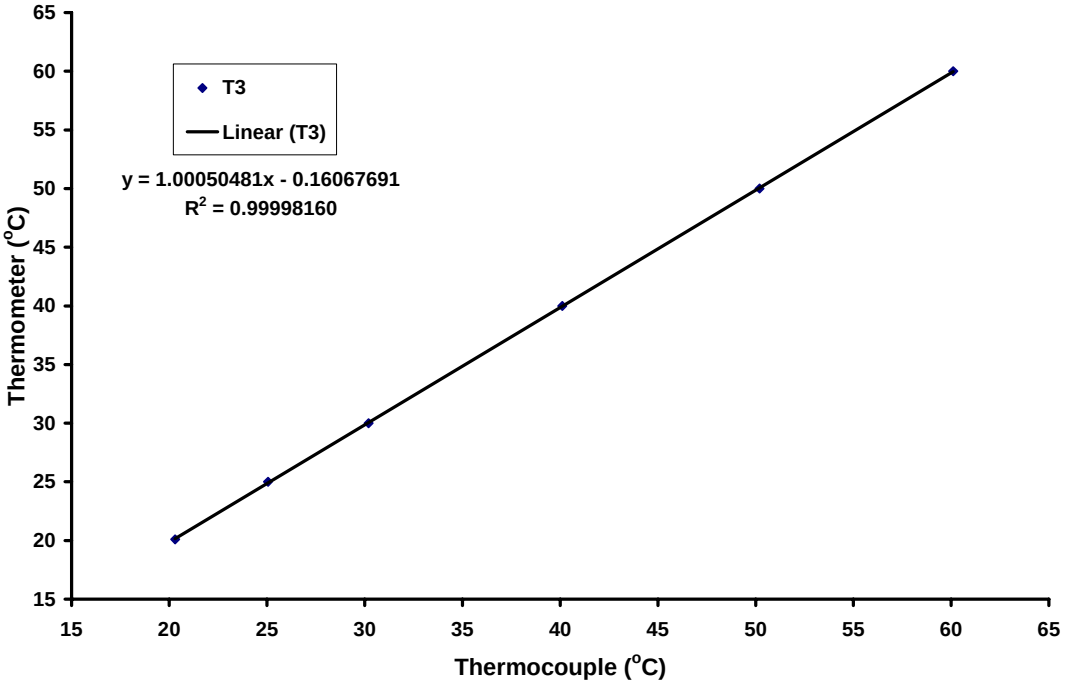

Figure A.31: Calibration Curve for ITO #2 Pedestal Thermocouple T_3

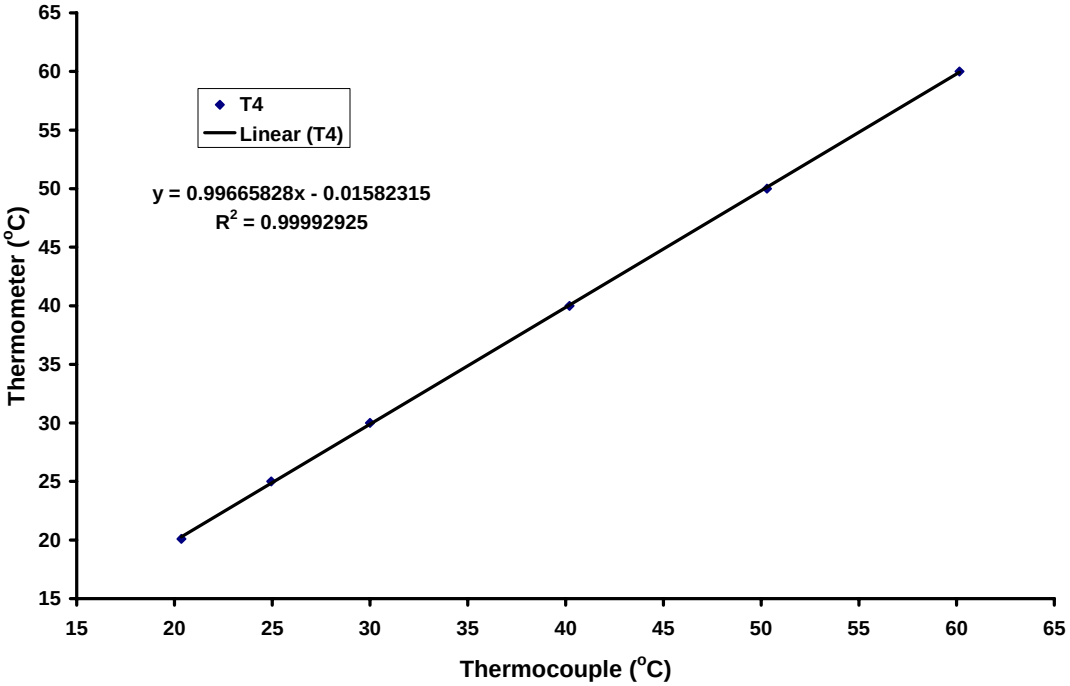

Figure A.32: Calibration Curve for ITO #2 Pedestal Thermocouple T_4

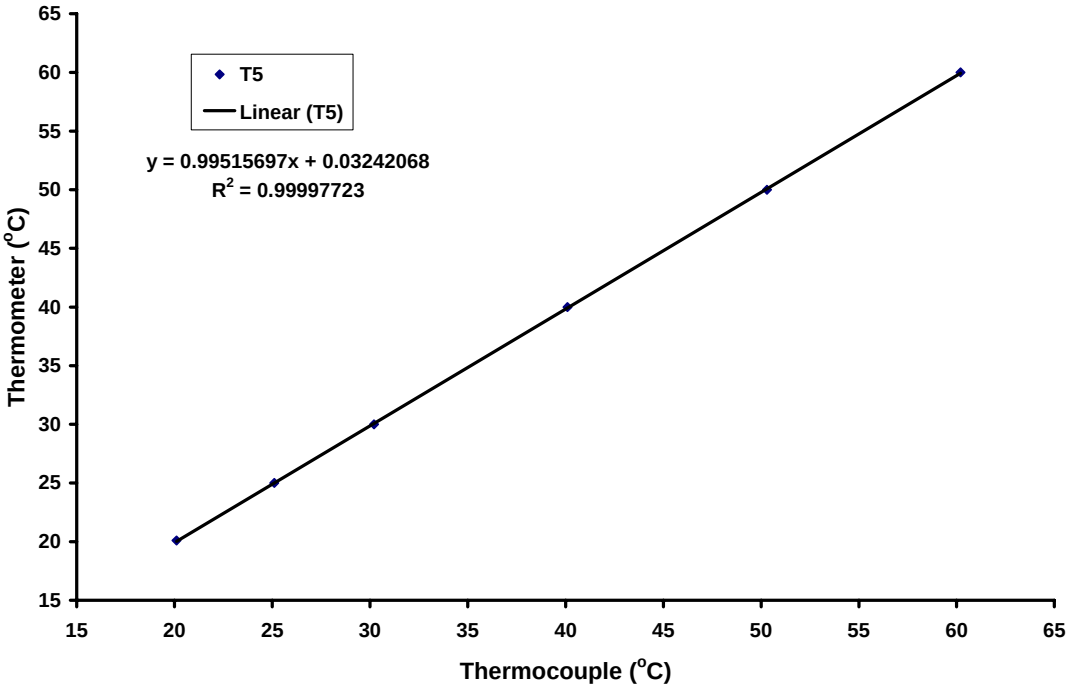

Figure A.33: Calibration Curve for ITO #2 Pedestal Thermocouple T_5

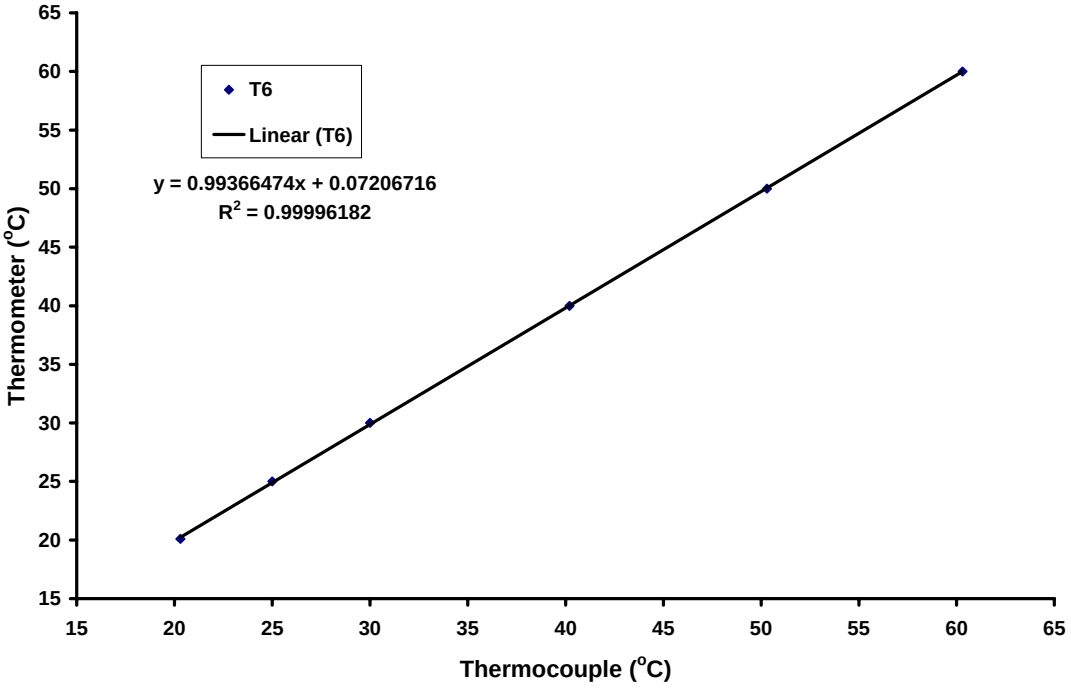

Figure A.34: Calibration Curve for ITO #2 Pedestal Thermocouple T_6

APPENDIX B : REDUCED DATA

Table B.1: Unconfined Flow Data in Terrestrial Gravity with a Flow Rate of 9.3 GPH, (A) Power and Pedestal Temperatures, (B) Chamber Temperatures, (C) Flow Rates and Pressures

(A)

	Pedestal Thermocouple Tempatures					
Power	T_1	T_2	T_3	T_4	T_5	T_6
Wattage	^oC	^oC	^oC	^oC	^oC	^oC
9.94	29.58	25.03	26.95	25.94	26.57	26.00
20.04	36.40	31.73	31.84	29.83	30.86	29.77
30.08	42.11	35.83	36.14	33.52	34.95	33.84
40.15	48.43	39.98	39.93	36.30	38.39	36.77
49.85	53.39	43.53	44.32	39.99	42.53	40.69
59.89	59.06	48.08	48.62	43.78	46.71	44.27
70.03	66.38	53.53	56.81	50.55	56.09	51.36

(B)

Chamber Thermocouple Temperatures						
T_8	T_9	T_{10}	T_{11}	T_{12}	T_{13}	T_{14}
^oC	^oC	^oC	^oC	^oC	^oC	^oC
22.73	22.70	23.79	23.92	22.05	22.30	21.77
22.19	22.00	24.63	24.12	21.91	22.10	21.77
22.19	22.00	24.63	24.12	21.91	22.10	21.77
23.48	23.39	26.97	26.99	23.69	23.89	22.36
24.28	24.33	28.70	28.92	24.79	24.98	22.56
25.57	25.57	30.39	29.76	25.98	25.67	22.86
27.17	27.06	31.78	29.36	27.27	27.16	22.76

(C)

Flow Rates			Pressure					
Nozz	Sump	H2O	Drain	FC-72 Heat X	Nozz	Chamber	Tuthill	Sump
GPH	GPH	GPH	psia	psia	psia	psia	psia	psia
10.14	10.14	12.00	11.86	18.82	24.82	11.12	26.82	16.12
10.14	10.14	12.00	11.86	17.82	24.82	11.12	26.82	15.92
10.14	10.14	12.00	11.86	17.32	24.82	11.12	26.82	15.62
10.14	10.14	12.00	11.86	17.32	25.32	11.12	27.07	15.12
10.14	10.14	12.00	12.11	17.32	25.32	11.12	27.32	15.12
10.14	10.14	12.00	11.86	17.32	25.32	11.12	26.82	14.72
10.14	10.14	12.00	11.86	17.32	25.32	11.37	27.32	14.72

Table B.2: Unconfined Flow Data in Terrestrial Gravity with Flow Rate of 7.7GPH, (A) Power, Flow Rates, and Pedestal Temperatures, (B) Chamber Temperatures, (C) Pressures

(A)

	$\dot{V}$			Pedestal Thermocouples					
Power	Nozz	Sump	H2O	T_1	T_2	T_3	T_4	T_5	T_6
Watts	GPH	GPH	GPH	^oC	^oC	^oC	^oC	^oC	^oC
9.92	8.45	8.45	12	30.88	25.03	28.15	25.35	27.37	26.60
20.02	8.45	8.45	12	40.01	28.03	34.04	28.63	32.56	30.07
29.89	8.45	8.45	12	48.03	29.63	38.73	30.73	36.54	33.05
39.93	8.45	8.45	12	55.45	31.13	42.73	32.62	40.13	35.33
50.06	8.45	8.45	12	63.57	33.53	47.82	35.61	44.32	38.41
59.89	8.45	8.45	12	70.29	35.23	52.11	37.30	47.91	40.59
70.03	8.45	8.45	12	77.51	37.43	56.51	39.59	51.60	43.37

(B)

Chamber Temperatures						
T_8	T_9	T_{10}	T_{11}	T_{12}	T_{13}	T_{14}
^oC	^oC	^oC	^oC	^oC	^oC	^oC
23.58	23.99	24.63	24.71	24.19	24.28	24.85
25.47	25.18	26.42	26.20	25.18	25.38	24.16
26.67	25.77	28.41	27.09	26.18	26.17	27.04
27.37	26.37	29.30	27.68	26.87	26.47	27.89
28.56	27.85	30.39	28.77	28.16	27.56	28.83
29.16	28.05	31.88	30.06	28.66	27.76	30.23
29.46	28.55	32.58	30.50	29.45	29.15	30.62

(C)

Pressure					
Drain	FC-72 Heat X	Nozz	Chamber	Tuthill	Sump
psia	psia	psia	psia	psia	psia
9.99	17.67	17.67	10.48	19.42	15.17
9.99	18.17	17.67	10.73	19.42	15.27
9.99	18.17	17.67	10.73	19.42	15.07
9.99	18.17	17.67	10.73	19.42	15.17
10.24	18.67	17.67	10.73	19.42	15.17
10.24	18.67	17.67	10.98	19.67	15.17
10.24	18.17	17.67	10.98	19.42	15.17

Table B.3: Unconfined Flow Data in Terrestrial Gravity with Flow Rate of 6.2GPH, (A) Power, Flow Rates, and Pedestal Temperatures, (B) Chamber Temperatures, (C) Pressures

(A)

	$\dot{V}$			Pedestal Thermocouples					
Power	Nozz	Sump	H2O	T_1	T_2	T_3	T_4	T_5	T_6
Watts	GPH	GPH	GPH	^oC	^oC	^oC	^oC	^oC	^oC
9.92	6.76	6.76	12	31.08	23.53	26.95	24.05	26.67	25.01
20.02	6.76	6.76	12	41.01	26.53	33.24	27.64	31.96	29.28
29.89	6.76	6.76	12	50.03	29.33	38.93	30.53	36.94	32.55
39.93	6.76	6.76	12	58.86	32.13	45.02	34.01	41.93	36.52
50.06	6.76	6.76	12	66.88	34.73	50.32	36.90	46.52	39.80
60.12	6.76	6.76	12	74.50	37.43	55.41	39.19	50.50	42.78
70.03	6.76	6.76	12	80.11	40.33	59.90	42.33	54.79	45.76

(B)

Chamber Temperatures						
T_8	T_9	T_{10}	T_{11}	T_{12}	T_{13}	T_{14}
^oC	^oC	^oC	^oC	^oC	^oC	^oC
25.37	24.48	25.53	25.21	24.59	25.28	24.55
24.98	24.98	26.72	25.50	24.89	25.28	25.95
25.67	25.57	28.41	26.59	25.58	25.97	26.94
26.67	26.27	29.99	27.78	26.97	26.57	28.14
27.37	27.06	31.68	29.17	27.87	27.46	29.23
28.36	27.95	32.87	30.26	28.86	27.96	30.38
29.36	28.45	33.77	31.05	29.85	28.65	31.52

(C)

Pressure					
Drain	FC-72 Heat X	Nozz	Chamber	Tuthill	Sump
psia	psia	psia	psia	psia	psia
9.75	17.61	14.54	10.48	15.40	14.76
9.75	17.61	14.54	10.48	15.40	14.86
9.75	17.61	14.66	10.48	15.52	14.91
9.99	17.61	14.78	10.73	15.52	14.96
10.24	17.85	14.78	10.73	15.64	15.05
10.24	17.85	15.03	10.98	15.89	15.10
10.48	18.10	15.15	11.22	15.89	15.15

Table B.4: Unconfined Flow Data in Terrestrial Gravity with Flow Rate of 4.6GPH, (A) Power, Flow Rates, and Pedestal Temperatures, (B) Chamber Temperatures, (C) Pressures

(A)

	$\dot{V}$			Pedestal Thermocouples					
Power	Nozz	Sump	H2O	T_1	T_2	T_3	T_4	T_5	T_6
Watts	GPH	GPH	GPH	^oC	^oC	^oC	^oC	^oC	^oC
10.03	5.28	5.28	12	32.39	24.63	28.15	25.05	27.37	25.80
20.02	5.28	5.28	12	43.92	29.43	35.14	29.43	33.65	30.77
29.89	5.28	5.28	12	52.64	32.13	41.53	32.82	38.84	34.14
39.93	5.28	5.28	12	61.26	35.33	47.62	36.60	44.92	38.51
50.06	5.28	5.28	12	69.89	38.33	53.11	39.59	49.31	41.59
59.89	5.28	5.28	12	77.11	40.83	58.01	42.38	53.39	44.86
70.03	5.28	5.28	12	84.13	42.83	62.30	44.57	57.18	46.55

(B)

Chamber Temperatures						
T_8	T_9	T_{10}	T_{11}	T_{12}	T_{13}	T_{14}
^oC	^oC	^oC	^oC	^oC	^oC	^oC
24.48	34.00	25.23	24.41	23.79	24.38	24.85
25.67	25.47	27.41	26.20	25.18	25.47	23.86
27.07	25.77	28.90	27.19	25.68	26.07	23.66
27.47	26.27	30.79	28.67	27.07	26.77	23.66
27.97	27.36	32.38	30.35	27.87	27.26	23.56
28.86	28.15	34.46	31.74	29.16	28.06	23.76
30.36	29.14	35.36	33.23	30.15	27.76	23.76

(C)

Pressure					
Drain	FC-72 Heat X	Nozz	Chamber	Tuthill	Sump
psia	psia	psia	psia	psia	psia
9.75	22.17	14.42	10.24	16.17	16.27
9.75	22.17	14.67	10.48	16.17	16.47
9.75	22.67	14.67	10.48	16.17	16.57
9.99	22.67	14.67	10.48	16.42	16.77
10.24	22.67	14.92	10.73	16.42	16.87
10.24	22.67	14.92	10.73	16.67	16.97
10.24	23.17	15.17	10.98	16.67	17.17

Table B.5: Straight Cap Data in Terrestrial Gravity with Flow Rate of 9.3GPH, (A) Power, Flow Rates, and Pedestal Temperatures, (B) Chamber Temperatures, (C) Pressures

(A)

	$\dot{V}$			Pedestal Thermocouples					
Power	Nozz	Sump	H2O	T_1	T_2	T_3	T_4	T_5	T_6
Watts	GPH	GPH	GPH	^oC	^oC	^oC	^oC	^oC	^oC
10.03	10.14	10.14	12	30.48	24.38	27.75	25.55	27.77	24.76
20.02	10.14	10.14	12	38.65	26.23	32.54	27.64	31.46	29.77
30.08	10.14	10.14	12	46.32	28.43	37.83	30.23	36.15	33.35
39.93	10.14	10.14	12	53.74	29.73	42.43	32.92	40.53	30.67
50.06	10.14	10.14	12	60.86	31.53	47.62	35.31	44.82	33.45
59.89	10.14	10.14	12	68.08	33.23	51.71	37.20	48.41	42.58
70.03	10.14	10.14	12	74.50	34.63	55.91	39.19	51.80	35.33

(B)

Chamber Temperatures						
T_8	T_9	T_{10}	T_{11}	T_{12}	T_{13}	T_{14}
^oC	^oC	^oC	^oC	^oC	^oC	^oC
22.98	23.39	25.53	24.17	23.99	23.79	23.26
24.68	24.19	27.31	25.11	25.48	23.79	23.96
25.97	25.28	28.80	26.39	26.77	24.48	24.55
26.67	25.67	30.14	26.94	27.87	24.68	25.05
27.07	26.37	31.93	28.03	29.26	24.78	26.15
28.46	27.90	33.77	29.66	31.34	25.57	26.94
29.36	28.35	33.97	29.66	31.74	26.27	26.74

(C)

Pressure					
Drain	FC-72 Heat X	Nozz	Chamber	Tuthill	Sump
psia	psia	psia	psia	psia	psia
11.72	19.17	21.67	11.47	23.17	16.77
11.72	19.17	21.67	11.47	23.17	15.37
11.72	18.17	21.42	11.47	23.17	15.97
11.72	17.17	21.17	11.47	22.92	15.67
11.72	16.67	20.67	11.47	22.67	15.17
11.72	16.17	20.92	11.23	22.67	14.87
11.72	15.17	20.67	11.23	22.42	14.57

Table B.6: Straight Cap Data in Terrestrial Gravity with Flow Rate of 7.7GPH, (A) Power, Flow Rates, and Pedestal Temperatures, (B) Chamber Temperatures, (C) Pressures

(A)

	$\dot{V}$			Pedestal Thermocouples					
Power	Nozz	Sump	H2O	T_1	T_2	T_3	T_4	T_5	T_6
Watts	GPH	GPH	GPH	^oC	^oC	^oC	^oC	^oC	^oC
10.03	8.45	8.45	12	30.88	24.83	28.45	25.84	28.07	25.61
20.02	8.45	8.45	12	39.61	26.83	33.24	28.34	32.26	27.59
30.08	8.45	8.45	12	46.98	28.28	38.13	31.12	36.64	34.54
39.93	8.45	8.45	12	54.35	29.63	43.13	33.52	41.73	31.21
49.85	8.45	8.45	12	62.07	31.83	48.52	36.80	46.32	33.74
59.89	8.45	8.45	12	68.83	33.13	52.81	39.39	50.30	36.03
70.03	8.45	8.45	12	76.61	35.13	57.11	41.58	53.69	48.09

(B)

Chamber Temperatures						
T_8	T_9	T_{10}	T_{11}	T_{12}	T_{13}	T_{14}
^oC	^oC	^oC	^oC	^oC	^oC	^oC
22.48	23.00	24.73	23.62	23.40	22.50	24.45
24.68	24.68	27.21	24.91	25.38	23.59	24.55
25.67	24.98	28.70	25.40	26.67	23.29	27.04
26.47	25.97	30.39	26.49	28.56	23.69	28.09
26.87	26.86	31.88	28.08	30.25	24.08	26.74
27.57	27.85	32.97	28.67	31.24	23.79	30.62
28.96	28.74	34.07	29.56	32.93	24.18	27.44

(C)

Pressure					
Drain	FC-72 Heat X	Nozz	Chamber	Tuthill	Sump
psia	psia	psia	psia	psia	psia
11.63	21.84	19.09	11.63	20.59	17.04
11.63	22.84	19.09	11.88	20.84	17.64
11.63	21.84	19.34	11.88	20.84	17.54
11.63	22.84	19.34	12.13	20.84	17.84
11.63	21.84	19.34	12.37	20.84	17.64
11.63	22.84	19.34	12.37	20.84	17.84
11.63	22.84	19.34	12.37	20.84	18.04

Table B.7: Straight Cap Data in Terrestrial Gravity with Flow Rate of 6.2GPH, (A) Power, Flow Rates, and Pedestal Temperatures, (B) Chamber Temperatures, (C) Pressures

(A)

	$\dot{V}$			Pedestal Thermocouples					
Power	Nozz	Sump	H2O	T_1	T_2	T_3	T_4	T_5	T_6
Watts	GPH	GPH	GPH	^oC	^oC	^oC	^oC	^oC	^oC
10.03	6.76	6.76	12	31.83	23.43	27.95	25.15	28.07	26.80
20.02	6.76	6.76	12	40.51	26.33	33.64	28.83	33.35	31.26
29.89	6.76	6.76	12	48.53	28.93	39.33	31.32	37.64	29.87
39.93	6.76	6.76	12	56.75	30.83	44.52	34.36	42.33	31.86
50.06	6.76	6.76	12	63.82	32.73	49.02	37.00	46.52	33.55
60.12	6.76	6.76	12	71.99	35.63	55.71	40.79	54.39	46.35
64.82	6.76	6.76	12	98.06	49.43				

(B)

Chamber Temperatures						
T_8	T_9	T_{10}	T_{11}	T_{12}	T_{13}	T_{14}
^oC	^oC	^oC	^oC	^oC	^oC	^oC
26.67	25.42	27.51	25.60	26.18	24.18	24.85
26.67	26.51	28.90	26.49	26.87	24.18	26.34
26.77	26.07	30.89	27.48	27.77	24.38	25.85
26.47	26.66	32.58	28.77	29.75	24.48	26.54
26.77	27.36	34.17	29.46	30.75	25.08	26.54
28.36	29.93	36.25	30.75	35.02	24.88	31.02
30.26	29.34	34.46				

(C)

Pressure					
Drain	FC-72 Heat X	Nozz	Chamber	Tuthill	Sump
psia	psia	psia	psia	psia	psia
11.63	19.50	16.06	11.88	16.42	16.01
11.63	19.74	16.42	11.88	16.67	16.20
11.63	19.74	16.06	11.88	16.79	16.40
11.63	19.74	16.18	11.88	16.79	16.40
11.63	19.74	16.30	12.13	16.92	16.55
11.63	19.99	16.30	12.37	16.92	16.11
11.63	19.99	16.30	12.62	17.04	16.11

Table B.8: Straight Cap Data in Terrestrial Gravity with Flow Rate of 5.0GPH, (A) Power, Flow Rates, and Pedestal Temperatures, (B) Chamber Temperatures, (C) Pressures

(A)

	$\dot{V}$			Pedestal Thermocouples					
Power	Nozz	Sump	H2O	T_1	T_2	T_3	T_4	T_5	T_6
Watts	GPH	GPH	GPH	^oC	^oC	^oC	^oC	^oC	^oC
10.01	5.49	5.49	12	31.88	24.93	28.65	25.84	28.17	27.09
20.12	5.49	5.49	12	40.81	27.53	34.94	29.33	33.50	30.97
30.02	5.49	5.49	12	49.93	30.08	40.63	32.42	38.84	35.04
39.89	5.49	5.49	12	58.66	32.03	45.92	35.21	43.62	38.31
50.02	5.49	5.49	12	66.78	34.23	51.02	37.70	47.81	40.89

(B)

Chamber Temperatures						
T_8	T_9	T_{10}	T_{11}	T_{12}	T_{13}	T_{14}
^oC	^oC	^oC	^oC	^oC	^oC	^oC
23.98	24.28	26.52	25.01	24.79	23.89	24.35
24.88	24.58	28.60	25.70	26.28	23.89	25.25
25.27	25.37	30.79	27.09	27.47	23.69	25.55
26.07	26.37	32.58	28.28	29.16	24.08	28.63
26.27	27.46	34.07	29.36	31.09	24.28	29.73

(C)

Pressure					
Drain	FC-72 Heat X	Nozz	Chamber	Tuthill	Sump
psia	psia	psia	psia	psia	psia
11.63	18.84	15.34	11.14	16.59	16.44
11.63	19.34	15.34	10.65	16.59	17.14
11.63	19.34	15.34	10.65	16.59	16.54
11.63	19.34	15.34	10.90	16.59	16.44
11.63	19.34	15.34	10.90	16.59	17.04

Table B.9: Curved Cap Data in Terrestrial Gravity with Flow Rate of 9.3 GPH, (A) Power, Flow Rates, and Pedestal Temperatures, (B) Chamber Temperatures, (C) Pressures

(A)

	$\dot{V}$			Pedestal Thermocouples					
Power	Nozz	Sump	H2O	T_1	T_2	T_3	T_4	T_5	T_6
Watts	GPH	GPH	GPH	^oC	^oC	^oC	^oC	^oC	^oC
10.03	10.14	10.14	12	30.43	24.63	29.14	26.04	28.27	26.70
20.02	10.14	10.14	12	38.15	26.43	32.64	28.04	32.11	29.87
30.08	10.14	10.14	12	46.47	28.18	37.33	30.08	36.20	32.60
39.93	10.14	10.14	12	53.14	29.38	41.63	31.47	39.24	34.89
49.85	10.14	10.14	12	59.86	30.48	45.62	33.42	42.98	37.42
60.12	10.14	10.14	12	65.98	31.93	49.67	35.71	46.61	40.15
70.03	10.14	10.14	12	72.80	32.63	53.31	36.60	49.16	40.00

(B)

Chamber Temperatures						
T_8	T_9	T_{10}	T_{11}	T_{12}	T_{13}	T_{14}
^oC	^oC	^oC	^oC	^oC	^oC	^oC
24.28	24.78	27.51	25.80	25.18	24.43	25.05
25.97	26.96	27.81	26.39	25.78	24.98	26.05
26.17	26.37	28.21	27.48	26.57	25.57	27.54
26.67	26.76	29.50	27.88	27.96	25.67	29.03
28.12	27.16	30.84	28.87	29.06	26.17	30.33
29.46	28.84	32.28	29.66	29.95	26.07	31.22
30.56	29.04	33.57	30.75	31.44	26.47	32.22

(C)

Pressure					
Drain	FC-72 Heat X	Nozz	Chamber	Tuthill	Sump
psia	psia	psia	psia	psia	psia
11.37	19.32	21.82	11.37	22.32	15.92
11.37	19.32	21.82	11.37	22.32	15.92
11.37	19.32	21.82	11.37	22.32	15.92
11.37	19.32	21.82	11.37	22.32	15.92
11.37	19.32	21.82	11.37	22.32	15.92
11.37	19.32	21.82	11.37	22.32	15.92
11.37	19.32	21.82	11.37	22.32	15.92

Table B.10: Curved Cap Data in Terrestrial Gravity with Flow Rate of 7.7 GPH, (A) Power, Flow Rates, and Pedestal Temperatures, (B) Chamber Temperatures, (C) Pressures

(A)

	$\dot{V}$			Pedestal Thermocouples					
Power	Nozz	Sump	H2O	T_1	T_2	T_3	T_4	T_5	T_6
Watts	GPH	GPH	GPH	^oC	^oC	^oC	^oC	^oC	^oC
9.99	8.45	8.45	12	29.93	23.83	27.65	24.95	27.17	25.90
20	8.45	8.45	12	38.50	25.73	31.84	27.04	31.06	28.48
29.86	8.45	8.45	12	46.42	27.63	36.98	29.73	35.65	31.36
40.08	8.45	8.45	12	53.64	29.23	41.73	31.22	39.34	34.04
50.02	8.45	8.45	12	60.56	30.33	45.82	33.12	42.63	36.33
60.08	8.45	8.45	12	67.78	31.93	50.22	35.11	46.22	39.10
69.98	8.45	8.45	12	74.10	33.23	54.21	37.00	49.41	41.69

(B)

Chamber Temperatures						
T_8	T_9	T_{10}	T_{11}	T_{12}	T_{13}	T_{14}
^oC	^oC	^oC	^oC	^oC	^oC	^oC
23.38	24.09	25.82	26.20	24.79	24.28	28.24
24.68	24.38	26.22	25.70	25.08	24.08	24.06
25.57	25.08	27.81	26.49	26.28	24.28	24.16
26.77	26.27	29.00	27.43	27.37	24.88	24.35
27.57	26.66	29.90	28.08	28.26	24.98	24.21
28.76	27.56	31.39	29.17	29.75	25.18	24.45
30.06	28.45	32.48	30.35	31.14	25.47	24.25

(C)

Pressure					
Drain	FC-72 Heat X	Nozz	Chamber	Tuthill	Sump
psia	psia	psia	psia	psia	psia
11.63	19.84	18.59	11.39	20.34	15.84
11.88	20.34	18.59	11.39	20.34	16.04
11.88	20.34	18.84	11.39	20.34	16.14
11.63	20.84	18.84	11.63	20.59	16.34
11.63	20.84	18.84	11.63	20.59	16.44
11.63	20.84	18.84	11.88	20.59	16.54
11.63	20.84	19.09	11.88	20.84	16.64

Table B.11: Curved Cap Data in Terrestrial Gravity with Flow Rate of 6.2 GPH, (A) Power, Flow Rates, and Pedestal Temperatures, (B) Chamber Temperatures, (C) Pressures

(A)

	$\dot{V}$			Pedestal Thermocouples					
Power	Nozz	Sump	H2O	T_1	T_2	T_3	T_4	T_5	T_6
Watts	GPH	GPH	GPH	^oC	^oC	^oC	^oC	^oC	^oC
10.01	6.76	6.76	12	34.49	25.33	28.85	26.64	28.37	27.39
20	6.76	6.76	12	42.01	28.83	34.74	29.93	33.25	30.62
30.05	6.76	6.76	12	49.43	31.03	39.83	32.22	37.74	33.55
39.89	6.76	6.76	12	57.45	34.43	45.42	35.51	42.33	37.22
50.02	6.76	6.76	12	64.97	36.83	50.32	38.20	46.42	40.10
60.08	6.76	6.76	12	72.29	40.43	55.11	40.79	50.70	43.08

(B)

Chamber Temperatures						
T_8	T_9	T_{10}	T_{11}	T_{12}	T_{13}	T_{14}
^oC	^oC	^oC	^oC	^oC	^oC	^oC
26.37	24.68	25.53	25.50	24.79	24.28	25.55
28.56	25.87	27.21	27.88	26.08	24.68	26.54
29.96	26.37	28.70	29.07	27.07	24.88	27.54
27.97	27.26	30.29	30.45	28.36	24.88	28.58
28.66	28.55	31.78	31.94	29.55	25.47	24.55
30.66	29.83	33.77	33.72	30.55	26.27	30.82

(C)

Pressure					
Drain	FC-72 Heat X	Nozz	Chamber	Tuthill	Sump
psia	psia	psia	psia	psia	psia
11.14	28.34	18.09	11.88	19.59	19.14
11.14	28.84	18.34	12.13	20.34	18.34
11.14	28.84	18.34	12.13	20.34	18.54
11.14	29.34	18.59	12.37	19.84	19.74
11.39	29.34	18.84	12.37	20.09	19.84
11.63	29.34	18.84	12.62	20.34	19.94

Table B.12: Curved Cap Data in Terrestrial Gravity with Flow Rate of 4.6 GPH, (A) Power, Flow Rates, and Pedestal Temperatures, (B) Chamber Temperatures, (C) Pressures

(A)

	$\dot{V}$			Pedestal Thermocouples					
Power	Nozz	Sump	H2O	T_1	T_2	T_3	T_4	T_5	T_6
Watts	GPH	GPH	GPH	^oC	^oC	^oC	^oC	^oC	^oC
10.03	5.28	5.28	12	32.39	24.63	28.75	25.25	28.07	26.00
20.02	5.28	5.28	12	42.31	27.73	34.34	28.24	32.96	29.48
29.89	5.28	5.28	12	50.43	29.33	39.63	30.23	37.24	32.45
39.93	5.28	5.28	12	58.96	31.53	45.52	32.92	42.23	35.73
50.06	5.28	5.28	12	67.98	34.33	51.02	36.11	46.81	38.91
59.89	5.28	5.28	12	74.90	36.33	55.41	38.00	50.40	41.29

(B)

Chamber Temperatures						
T_8	T_9	T_{10}	T_{11}	T_{12}	T_{13}	T_{14}
^oC	^oC	^oC	^oC	^oC	^oC	^oC
22.48	22.90	24.63	23.23	23.00	22.30	24.16
24.98	24.09	26.12	24.81	25.28	22.79	23.76
25.27	24.58	27.71	26.30	25.98	23.39	26.84
25.77	25.47	29.50	27.68	27.27	23.59	27.74
26.47	26.66	31.58	29.07	28.96	24.08	29.43
26.57	27.26	32.28	30.26	30.05	23.89	30.33

(C)

Pressure					
Drain	FC-72 Heat X	Nozz	Chamber	Tuthill	Sump
psia	psia	psia	psia	psia	psia
9.99	16.17	13.67	10.48	15.42	14.97
9.50	16.17	13.92	9.99	14.67	14.97
9.26	16.17	13.92	9.99	15.67	14.97
9.26	16.17	14.17	9.99	14.67	14.87
9.26	16.67	14.17	9.99	15.67	14.87
9.01	16.67	14.17	10.24	15.67	14.87

Table B.13: Unconfined Flow Data in Simulated Microgravity with Flow Rate of 9.3 GPH, (A) Power, Flow Rates, and Pedestal Temperatures, (B) Chamber Temperatures, (C) Pressure

(A)

	$\dot{V}$			Pedestal Thermocouples					
Power	Nozz	Sump	H2O	T_1	T_2	T_3	T_4	T_5	T_6
Watts	GPH	GPH	GPH	^oC	^oC	^oC	^oC	^oC	^oC
10.03	10.14	10.14	12	34.09	28.23	31.04	28.83	30.16	29.38
20.02	10.14	10.14	12	42.31	30.43	36.24	32.42	34.95	33.74
29.89	10.14	10.14	12	49.93	32.53	29.14	35.11	39.34	36.52
39.93	10.14	10.14	12	56.95	34.13	46.12	37.90	43.22	39.70
50.06	10.14	10.14	12	64.07	36.23	50.62	40.69	47.11	42.38
60.12	10.14	10.14	12	70.59	37.83	54.81	42.98	50.80	45.16

(B)

Chamber Temperatures						
T_8	T_9	T_{10}	T_{11}	T_{12}	T_{13}	T_{14}
^oC	^oC	^oC	^oC	^oC	^oC	^oC
28.56	28.05	28.11	27.98	28.96	27.86	28.43
29.56	28.45	28.70	28.77	29.36	28.55	28.43
29.66	29.14	29.30	29.46	29.95	29.35	28.53
30.66	29.74	29.80	29.96	30.75	29.65	28.53
31.65	30.33	30.49	31.15	31.34	30.04	28.43
32.35	30.93	30.99	31.54	31.94	30.74	28.34

(C)

Pressure					
Drain	FC-72 Heat X	Nozz	Chamber	Tuthill	Sump
psia	psia	psia	psia	psia	psia
11.36	20.41	23.11	11.65	24.21	15.61
11.65	20.21	23.21	12.00	24.21	15.61
11.26	20.41	23.11	11.51	24.31	15.71
11.26	20.71	23.21	11.51	24.46	15.81
11.26	21.01	23.21	11.75	24.61	15.81
11.26	20.71	23.21	11.75	24.61	15.91

Table B.14: Unconfined Flow Data in Simulated Microgravity with Flow Rate of 7.7 GPH, (A) Power, Flow Rates, and Pedestal Temperatures, (B) Chamber Temperatures, (C) Pressure

(A)

	$\dot{V}$			Pedestal Thermocouples					
Power	Nozz	Sump	H2O	T_1	T_2	T_3	T_4	T_5	T_6
Watts	GPH	GPH	GPH	^oC	^oC	^oC	^oC	^oC	^oC
10.03	8.45	8.45	12	36.30	28.43	32.34	29.63	30.96	29.97
20.02	8.45	8.45	12	45.02	30.93	38.13	33.32	36.15	34.34
29.89	8.45	8.45	12	51.74	32.83	42.43	35.31	40.03	36.42
39.93	8.45	8.45	12	58.96	34.53	47.42	38.60	44.42	40.40
50.06	8.45	8.45	12	65.98	36.13	51.81	41.09	48.31	43.27
59.89	8.45	8.45	12	73.00	38.33	56.21	44.07	52.40	46.35

(B)

Chamber Temperatures						
T_8	T_9	T_{10}	T_{11}	T_{12}	T_{13}	T_{14}
^oC	^oC	^oC	^oC	^oC	^oC	^oC
29.16	27.95	28.51	27.98	29.06	27.86	28.43
29.86	28.65	29.20	28.97	29.75	28.75	28.63
30.96	29.44	29.60	29.86	29.85	29.45	28.24
31.35	29.93	30.19	30.65	30.65	30.04	28.14
31.55	30.13	30.29	30.75	31.34	30.24	28.04
32.65	31.22	31.19	31.74	32.24	31.23	28.14

(C)

Pressure					
Drain	FC-72 Heat X	Nozz	Chamber	Tuthill	Sump
psia	psia	psia	psia	psia	psia
11.21	22.21	18.21	11.26	19.11	15.91
10.77	22.21	17.61	11.11	18.71	16.01
10.77	22.21	17.61	11.16	20.01	16.11
10.77	22.21	19.21	11.26	20.21	16.21
10.87	21.71	19.46	11.51	21.46	16.21
11.16	22.01	19.46	11.51	20.46	16.21

Table B.15: Unconfined Flow Data in Simulated Microgravity with Flow Rate of 6.2 GPH, (A) Power, Flow Rates, and Pedestal Temperatures, (B) Chamber Temperatures, (C) Pressure

(A)

	$\dot{V}$			Pedestal Thermocouples					
Power	Nozz	Sump	H2O	T_1	T_2	T_3	T_4	T_5	T_6
Watts	GPH	GPH	GPH	^oC	^oC	^oC	^oC	^oC	^oC
10.03	6.76	6.76	12	37.40	29.33	33.14	30.33	32.16	30.57
20.02	6.76	6.76	12	46.12	31.33	38.83	33.81	37.24	34.24
29.89	6.76	6.76	12	54.35	33.33	43.92	36.60	41.73	37.91
39.93	6.76	6.76	12	62.47	35.33	49.32	39.99	46.61	41.69
50.06	6.76	6.76	12	70.29	37.63	54.51	42.88	51.20	44.86

(B)

Chamber Temperatures						
T_8	T_9	T_{10}	T_{11}	T_{12}	T_{13}	T_{14}
^oC	^oC	^oC	^oC	^oC	^oC	^oC
30.16	29.24	29.20	28.47	29.06	28.65	27.84
30.16	29.24	29.30	29.27	29.45	29.05	28.14
30.86	29.74	29.70	30.06	30.35	29.65	27.94
31.95	30.73	30.49	30.85	30.75	30.14	27.64
32.15	30.93	30.99	31.54	31.24	30.74	27.64

(C)

Pressure					
Drain	FC-72 Heat X	Nozz	Chamber	Tuthill	Sump
psia	psia	psia	psia	psia	psia
10.77	23.01	15.96	11.02	16.96	16.21
10.52	22.21	15.71	10.89	16.61	16.31
10.52	21.21	15.71	10.77	16.71	16.01
10.52	21.71	15.71	10.87	16.71	16.01
10.52	21.71	16.01	11.02	16.81	16.11

Table B.16: Unconfined Flow Data in Simulated Microgravity with Flow Rate of 4.6 GPH, (A) Power, Flow Rates, and Pedestal Temperatures, (B) Chamber Temperatures, (C) Pressure

(A)

	$\dot{V}$			Pedestal Thermocouples					
Power	Nozz	Sump	H2O	T_1	T_2	T_3	T_4	T_5	T_6
Watts	GPH	GPH	GPH	^oC	^oC	^oC	^oC	^oC	^oC
10.03	5.28	5.28	12	38.40	28.93	33.24	30.43	32.36	30.67
20.02	5.28	5.28	12	48.53	32.13	40.03	34.51	38.34	35.23
29.89	5.28	5.28	12	57.35	34.63	46.32	38.40	43.82	39.50
39.93	5.28	5.28	12	66.58	37.23	52.11	41.68	48.81	43.27
50.06	5.28	5.28	12	74.00	30.83	57.11	44.87	53.30	46.25

(B)

Chamber Temperatures						
T_8	T_9	T_{10}	T_{11}	T_{12}	T_{13}	T_{14}
^oC	^oC	^oC	^oC	^oC	^oC	^oC
29.66	28.45	28.90	28.37	28.86	28.26	27.44
30.26	29.14	29.30	29.27	29.36	28.95	27.64
31.25	30.03	30.09	30.26	29.85	29.75	27.94
31.65	30.53	30.29	31.34	30.45	30.44	27.64
32.15	31.02	30.79	32.14	31.44	31.33	27.64

(C)

Pressure					
Drain	FC-72 Heat X	Nozz	Chamber	Tuthill	Sump
psia	psia	psia	psia	psia	psia
10.28	24.21	14.21	10.65	15.21	16.21
10.18	24.21	14.21	10.52	15.01	16.21
10.23	24.21	14.21	10.65	15.21	16.21
10.28	23.21	14.46	11.26	15.21	16.21
10.28	23.21	14.61	10.77	15.21	16.26

Table B.17: Curved Cap Data in Simulated Microgravity with Flow Rate of 9.3 GPH, (A) Power, Flow Rates, and Pedestal Temperatures, (B) Chamber Temperatures, (C) Pressure

(A)

	$\dot{V}$			Pedestal Thermocouples					
Power	Nozz	Sump	H2O	T_1	T_2	T_3	T_4	T_5	T_6
Watts	GPH	GPH	GPH	^oC	^oC	^oC	^oC	^oC	^oC
10.03	10.14	10.14	12	34.89	28.33	31.34	28.93	30.46	29.67
20.02	10.14	10.14	12	43.22	30.83	36.43	32.32	35.05	33.05
29.89	10.14	10.14	12	50.74	32.93	41.33	34.91	38.94	36.42
39.93	10.14	10.14	12	58.36	34.83	46.12	37.60	43.13	39.40
50.06	10.14	10.14	12	65.17	36.83	50.62	40.09	46.71	42.48
60.12	10.14	10.14	12	71.99	39.03	55.11	42.48	50.70	44.86

(B)

Chamber Temperatures						
T_8	T_9	T_{10}	T_{11}	T_{12}	T_{13}	T_{14}
^oC	^oC	^oC	^oC	^oC	^oC	^oC
28.07	27.85	28.41	27.98	30.05	27.76	29.83
29.26	28.65	29.20	29.17	30.55	28.65	29.53
30.06	29.74	30.19	29.96	31.24	29.35	29.63
30.76	30.03	30.99	31.05	32.04	30.14	29.63
31.45	30.63	31.58	31.94	32.63	31.04	29.63
32.15	31.52	32.58	32.83	33.63	31.53	29.53

(C)

Pressure					
Drain	FC-72 Heat X	Nozz	Chamber	Tuthill	Sump
psia	psia	psia	psia	psia	psia
11.02	18.21	22.46	11.26	23.71	14.61
10.77	18.21	22.21	11.26	23.21	14.81
10.28	18.21	22.21	11.02	23.21	14.81
10.77	18.71	22.21	11.02	23.21	14.81
10.28	19.21	21.21	11.26	23.21	14.91
10.28	19.21	22.46	11.26	23.46	14.91

Table B.18: Curved Cap Data in Simulated Microgravity with Flow Rate of 7.7 GPH, (A) Power, Flow Rates, and Pedestal Temperatures, (B) Chamber Temperatures, (C) Pressure

(A)

	$\dot{V}$			Pedestal Thermocouples					
Power	Nozz	Sump	H2O	T_1	T_2	T_3	T_4	T_5	T_6
Watts	GPH	GPH	GPH	^oC	^oC	^oC	^oC	^oC	^oC
10.03	8.45	8.45	12	37.60	30.33	33.44	30.93	32.26	31.36
20.02	8.45	8.45	12	45.52	32.33	38.33	33.71	36.54	34.54
29.05	8.45	8.45	12	52.64	33.93	42.73	35.91	40.23	37.02
39.93	8.45	8.45	12	61.16	35.93	48.22	38.89	44.82	40.40
50.06	8.45	8.45	12	68.53	38.23	53.41	42.28	49.11	43.47
59.89	8.45	8.45	12	75.60	40.43	57.81	44.47	52.90	45.95

(B)

Chamber Temperatures						
T_8	T_9	T_{10}	T_{11}	T_{12}	T_{13}	T_{14}
^oC	^oC	^oC	^oC	^oC	^oC	^oC
30.56	29.74	30.29	29.46	30.15	29.45	29.73
30.76	30.13	31.19	30.35	30.65	29.75	29.53
31.06	30.23	31.58	31.15	31.34	30.04	29.43
31.75	30.33	32.38	32.04	32.24	30.64	29.43
32.05	31.12	32.78	32.63	32.83	31.23	29.33
32.15	31.22	33.37	33.23	33.43	31.73	29.33

(C)

Pressure					
Drain	FC-72 Heat X	Nozz	Chamber	Tuthill	Sump
psia	psia	psia	psia	psia	psia
10.77	20.21	18.71	11.02	19.46	14.81
10.28	20.21	18.46	10.77	19.21	14.81
10.28	20.21	18.46	10.77	19.21	14.91
10.28	20.21	18.21	10.77	19.21	14.91
10.52	20.21	18.46	11.02	19.21	14.91
10.77	20.21	18.46	11.26	19.21	14.91

Table B.19: Curved Cap Data in Simulated Microgravity with Flow Rate of 6.2 GPH, (A) Power, Flow Rates, and Pedestal Temperatures, (B) Chamber Temperatures, (C) Pressure

(A)

	$\dot{V}$			Pedestal Thermocouples					
Power	Nozz	Sump	H2O	T_1	T_2	T_3	T_4	T_5	T_6
Watts	GPH	GPH	GPH	^oC	^oC	^oC	^oC	^oC	^oC
10.03	6.76	6.76	12	38.10	30.13	33.94	31.12	32.66	31.46
20.02	6.76	6.76	12	47.43	32.63	39.63	34.51	37.84	35.23
30.08	6.76	6.76	12	56.35	35.03	45.62	37.80	42.53	38.81
39.93	6.76	6.76	12	64.77	37.53	50.92	40.89	47.31	42.28
50.06	6.76	6.76	12	72.80	39.93	55.91	43.98	51.80	45.16

(B)

Chamber Temperatures						
T_8	T_9	T_{10}	T_{11}	T_{12}	T_{13}	T_{14}
^oC	^oC	^oC	^oC	^oC	^oC	^oC
29.86	29.24	29.60	29.17	30.05	29.05	29.33
29.86	29.44	30.09	30.06	30.45	29.55	29.33
30.46	29.74	31.09	30.95	31.24	30.24	29.23
30.76	29.93	31.78	31.94	31.84	30.54	29.03
31.65	30.73	32.87	32.93	32.53	31.14	29.03

(C)

Pressure					
Drain	FC-72 Heat X	Nozz	Chamber	Tuthill	Sump
psia	psia	psia	psia	psia	psia
10.28	20.21	15.96	10.52	16.71	15.01
10.28	20.71	15.46	10.52	16.21	15.01
10.28	20.21	15.21	10.52	16.21	15.21
10.28	20.21	15.21	10.77	16.21	15.21
10.28	20.21	15.21	11.02	16.21	15.21

Table B.20: Curved Cap Data in Simulated Microgravity with Flow Rate of 4.6 GPH, (A) Power, Flow Rates, and Pedestal Temperatures, (B) Chamber Temperatures, (C) Pressure

(A)

	$\dot{V}$			Pedestal Thermocouples					
Power	Nozz	Sump	H2O	T_1	T_2	T_3	T_4	T_5	T_6
Watts	GPH	GPH	GPH	^oC	^oC	^oC	^oC	^oC	^oC
10.03	5.28	5.28	12	38.40	29.93	33.84	31.12	32.86	31.46
20.02	5.28	5.28	12	48.13	32.63	40.23	35.16	38.44	35.53
30.08	5.28	5.28	12	58.16	35.63	47.12	39.39	44.42	40.20
39.93	5.28	5.28	12	66.38	37.53	52.61	42.68	49.01	43.47
50.06	5.28	5.28	12	74.80	41.13	58.01	45.77	53.69	46.35

(B)

Chamber Temperatures						
T_8	T_9	T_{10}	T_{11}	T_{12}	T_{13}	T_{14}
^oC	^oC	^oC	^oC	^oC	^oC	^oC
30.26	29.14	29.30	28.97	29.85	28.95	29.13
30.36	29.24	30.19	29.96	30.35	29.35	28.93
30.76	29.54	31.39	30.85	31.14	29.75	28.53
31.35	30.03	32.48	32.14	32.04	30.44	28.83
31.85	30.63	33.77	33.42	32.93	30.94	28.83

(C)

Pressure					
Drain	FC-72 Heat X	Nozz	Chamber	Tuthill	Sump
psia	psia	psia	psia	psia	psia
9.79	19.71	14.21	10.28	14.21	15.01
9.79	19.71	14.21	10.28	14.21	15.01
9.79	19.71	13.21	10.03	14.21	15.11
9.79	19.71	14.21	10.28	14.21	15.11
10.03	18.21	14.21	10.28	14.21	15.01

Table B.21: Straight Cap Data in Simulated Microgravity with Flow Rate of 9.3 GPH, (A) Power, Flow Rates, and Pedestal Temperatures, (B) Chamber Temperatures, (C) Pressure

(A)

	$\dot{V}$			Pedestal Thermocouples					
Power	Nozz	Sump	H2O	T_1	T_2	T_3	T_4	T_5	T_6
Watts	GPH	GPH	GPH	^oC	^oC	^oC	^oC	^oC	^oC
10.03	10.14	10.14	12	34.09	27.83	30.74	28.34	30.16	29.28
20.02	10.14	10.14	12	41.91	30.03	35.44	31.62	34.55	32.55
24.94	10.14	10.14	12	46.42	31.53	38.53	33.81	37.64	34.64
29.89	10.14	10.14	12	50.33	32.43	40.73	34.81	39.04	36.03
34.92	10.14	10.14	12	54.25	33.33	43.13	36.01	40.83	37.62
39.93	10.14	10.14	12	57.45	33.93	45.12	37.10	32.36	39.20
50.06	10.14	10.14	12	65.38	36.43	50.42	40.29	47.01	42.78
59.89	10.14	10.14	12	71.39	37.83	53.91	41.88	50.20	44.56

(B)

Chamber Temperatures						
T_8	T_9	T_{10}	T_{11}	T_{12}	T_{13}	T_{14}
^oC	^oC	^oC	^oC	^oC	^oC	^oC
26.07	26.37	26.62	26.49	29.75	26.57	29.53
27.87	27.36	28.11	27.88	27.07	27.56	28.63
28.76	28.05	28.70	28.57	27.77	28.45	28.83
29.16	28.25	29.30	28.97	28.86	28.55	29.23
29.66	28.74	29.60	29.76	30.75	29.05	29.43
30.06	38.95	30.19	29.96	31.34	29.75	29.23
30.96	29.83	31.19	30.85	32.24	30.44	29.53
31.35	30.13	31.88	31.25	32.63	30.64	29.03

(C)

Pressure					
Drain	FC-72 Heat X	Nozz	Chamber	Tuthill	Sump
psia	psia	psia	psia	psia	psia
10.28	17.71	22.21	10.77	22.71	15.01
10.28	17.71	22.21	10.77	22.96	15.01
10.28	17.71	22.21	10.77	22.96	15.01
10.28	17.71	22.21	11.26	22.96	14.91
10.28	17.21	22.21	10.77	22.96	14.71
10.28	17.71	22.21	11.26	22.96	14.71
10.28	17.21	22.21	10.77	22.96	14.21
10.28	17.21	22.21	10.77	22.96	14.21

Table B.22: Straight Cap Data in Simulated Microgravity with Flow Rate of 7.7GPH, (A) Power, Flow Rates, and Pedestal Temperatures, (B) Chamber Temperatures, (C) Pressure

(A)

	$\dot{V}$			Pedestal Thermocouples					
Power	Nozz	Sump	H2O	T_1	T_2	T_3	T_4	T_5	T_6
Watts	GPH	GPH	GPH	^oC	^oC	^oC	^oC	^oC	^oC
10.03	8.45	8.45	12	36.80	29.03	32.34	29.93	31.66	30.57
20.02	8.45	8.45	12	44.72	31.33	37.23	33.02	35.95	34.34
29.89	8.45	8.45	12	53.04	33.53	42.63	36.01	40.23	36.82
39.93	8.45	8.45	12	60.66	35.13	47.42	38.70	44.52	40.59
50.06	8.45	8.45	12	68.28	37.23	52.41	41.58	48.71	43.77
60.12	8.45	8.45	12	75.10	39.13	56.41	43.58	52.00	45.85

(B)

Chamber Temperatures						
T_8	T_9	T_{10}	T_{11}	T_{12}	T_{13}	T_{14}
^oC	^oC	^oC	^oC	^oC	^oC	^oC
29.26	28.15	28.31	28.18	29.75	28.06	29.33
29.56	28.74	29.30	28.87	30.45	29.25	29.73
30.36	29.83	30.49	29.96	31.44	29.75	29.93
30.86	30.13	30.99	30.45	31.94	30.04	29.73
31.65	30.43	31.88	31.54	32.63	30.74	29.63
31.85	30.73	32.38	32.24	33.13	30.94	29.63

(C)

Pressure					
Drain	FC-72 Heat X	Nozz	Chamber	Tuthill	Sump
psia	psia	psia	psia	psia	psia
10.03	17.71	18.46	10.52	19.21	14.21
9.79	17.21	18.21	10.28	19.21	14.21
9.79	17.21	18.21	10.28	18.96	14.21
9.79	16.71	18.21	10.52	18.71	14.21
9.79	17.21	18.21	10.52	18.96	14.21
10.28	17.21	18.21	10.52	18.96	14.21

Table B.23: Straight Cap Data in Simulated Microgravity with Flow Rate of 6.2 GPH, (A) Power, Flow Rates, and Pedestal Temperatures, (B) Chamber Temperatures, (C) Pressure

(A)

	$\dot{V}$			Pedestal Thermocouples					
Power	Nozz	Sump	H2O	T_1	T_2	T_3	T_4	T_5	T_6
Watts	GPH	GPH	GPH	^oC	^oC	^oC	^oC	^oC	^oC
10.03	6.76	6.76	12	38.00	29.73	33.44	30.83	33.05	31.66
20.02	6.76	6.76	12	47.83	32.83	39.53	34.81	38.24	34.94
30.08	6.76	6.76	12	56.15	34.33	44.32	36.90	42.23	38.01
39.93	6.76	6.76	12	63.37	36.23	49.32	39.59	47.11	41.29
50.06	6.76	6.76	12	71.79	39.53	55.11	43.28	51.50	44.76

(B)

Chamber Temperatures						
T_8	T_9	T_{10}	T_{11}	T_{12}	T_{13}	T_{14}
^oC	^oC	^oC	^oC	^oC	^oC	^oC
29.86	29.24	29.00	28.47	30.15	28.65	29.33
29.66	29.74	30.39	30.06	30.85	29.35	30.33
29.86	29.44	30.59	30.35	31.44	29.45	29.13
29.86	29.64	30.59	30.65	32.43	29.55	29.93
30.96	30.63	31.68	31.74	33.73	30.54	30.23

(C)

Pressure					
Drain	FC-72 Heat X	Nozz	Chamber	Tuthill	Sump
psia	psia	psia	psia	psia	psia
9.79	16.71	15.46	10.03	16.21	14.21
9.54	17.21	15.46	10.03	15.96	14.21
9.79	17.21	14.71	10.03	15.71	14.21
9.79	17.21	15.71	10.03	16.21	14.21
9.79	17.21	15.21	10.28	15.96	14.21

Table B.24: Straight Cap Data in Simulated Microgravity with Flow Rate of 4.6GPH, (A) Power, Flow Rates, and Pedestal Temperatures, (B) Chamber Temperatures, (C) Pressure

(A)

	$\dot{V}$			Pedestal Thermocouples					
Power	Nozz	Sump	H2O	T_1	T_2	T_3	T_4	T_5	T_6
Watts	GPH	GPH	GPH	^oC	^oC	^oC	^oC	^oC	^oC
10.03	5.28	5.28	12	39.41	30.73	34.54	31.62	33.65	32.55
20.02	5.28	5.28	12	49.53	33.53	40.83	35.11	31.26	36.33
39.93	5.28	5.28	12	67.38	38.53	52.11	41.98	49.01	43.27
50.96	5.28	5.28	12	74.30	40.13	57.01	44.57	53.00	45.95

(B)

Chamber Temperatures						
T_8	T_9	T_{10}	T_{11}	T_{12}	T_{13}	T_{14}
^oC	^oC	^oC	^oC	^oC	^oC	^oC
29.16	28.74	28.90	28.67	30.35	28.65	29.63
29.76	29.44	30.09	29.76	31.24	28.75	29.33
31.65	30.53	31.98	32.38	33.03	30.54	29.63
31.95	30.73	32.68	33.23	34.12	30.94	29.63

(C)

Pressure					
Drain	FC-72 Heat X	Nozz	Chamber	Tuthill	Sump
psia	psia	psia	psia	psia	psia
9.30	17.21	12.21	9.79	14.21	14.21
9.30	17.21	12.21	9.79	14.21	14.21
9.30	17.21	12.21	9.79	14.21	14.21
9.30	17.21	12.21	10.03	14.21	14.21

Table B.25: Unconfined Flow Data in Terrestrial Gravity with a Flow Rate of 9.3GPH and an ITO Pedestal, (A) Power, Flow Rates, and Pedestal Temperatures, (B) Chamber Temperatures, (C) Pressure

(A)

	$\dot{V}$			Pedestal Thermocouples						
Power	Nozz	Sump	H2O	T_1	T_2	T_3	T_4	T_5	T_6	T_7
Watts	GPH	GPH	GPH	^oC	^oC	^oC	^oC	^oC	^oC	^oC
10.03	10.14	10.14	12	31.25	29.30	29.51	28.47	29.49	28.81	27.80
20.04	10.14	10.14	12	37.67	31.78	33.39	30.85	33.01	31.23	29.20
24.97	10.14	10.14	12	41.01	32.98	35.17	31.65	33.30	31.38	28.90
30.11	10.14	10.14	12	44.10	34.57	37.16	32.64	34.99	32.37	29.40
34.97	10.14	10.14	12	47.69	35.76	39.05	33.23	35.98	32.86	29.20
39.99	10.14	10.14	12	51.28	37.85	41.63	34.82	37.96	34.25	29.60

(B)

Chamber Temperatures						
T_8	T_9	T_{10}	T_{11}	T_{12}	T_{13}	T_{14}
^oC	^oC	^oC	^oC	^oC	^oC	^oC
24.08	24.78	25.53	25.40	24.79	25.38	25.55
26.17	25.87	26.62	26.20	26.57	26.47	25.15
26.77	34.99	27.41	26.10	26.57	27.06	25.15
27.47	26.56	27.61	26.49	26.57	26.77	25.75
28.36	26.96	27.61	26.49	26.57	26.77	25.25
28.26	27.16	34.46	27.19	27.27	27.26	25.25

(C)

Pressure					
Drain	FC-72 Heat X	Nozz	Chamber	Tuthill	Sump
psia	psia	psia	psia	psia	psia
13.23	21.71	24.11	13.72	26.46	17.21
13.23	23.21	24.61	13.96	26.96	17.91
13.72	23.96	25.11	14.16	27.21	18.71
13.96	24.21	25.21	13.96	28.21	17.01
13.72	24.71	25.46	13.96	27.21	19.61
13.47	25.21	25.11	14.21	27.46	20.01

Table B.26: Straight Cap Data in Terrestrial Gravity with a Flow Rate of 9.3GPH and an ITO Pedestal, (A) Power, Flow Rates, and Pedestal Temperatures, (B) Chamber Temperatures, (C) Pressure

(A)

	$\dot{V}$			Pedestal Thermocouples						
Power	Nozz	Sump	H2O	T_1	T_2	T_3	T_4	T_5	T_6	T_7
Watts	GPH	GPH	GPH	^oC	^oC	^oC	^oC	^oC	^oC	^oC
10.04	10.14	10.14	12	31.55	28.40	29.41	27.78	28.45	28.02	27.20
19.91	10.14	10.14	12	38.32	31.78	33.98	31.15	33.30	31.38	29.10
24.99	10.14	10.14	12	41.71	33.37	36.07	32.44	34.79	32.57	29.40
29.95	10.14	10.14	12	44.00	33.67	37.06	32.44	35.29	32.57	28.90
34.97	10.14	10.14	12	47.09	35.06	39.64	33.63	36.87	33.66	29.60
40.02	10.14	10.14	12	50.98	37.35	42.32	35.42	39.35	35.63	30.40

(B)

Chamber Temperatures						
T_8	T_9	T_{10}	T_{11}	T_{12}	T_{13}	T_{14}
^oC	^oC	^oC	^oC	^oC	^oC	^oC
25.67	25.87	26.52	26.49	26.28	25.77	27.94
26.87	26.56	27.51	27.19	26.97	26.57	28.24
29.06	28.45	29.40	28.57	28.46	27.66	27.94
29.86	28.55	30.29	28.87	29.06	28.26	27.74
29.96	29.14	30.89	29.17	29.26	28.26	27.74
29.76	29.04	31.09	29.56	29.26	28.06	28.34

(C)

Pressure					
Drain	FC-72 Heat X	Nozz	Chamber	Tuthill	Sump
psia	psia	psia	psia	psia	psia
10.28	17.21	21.46	11.26	23.71	14.61
10.28	16.71	20.71	11.26	23.96	14.61
10.28	16.71	21.71	11.26	24.21	14.21
10.28	16.21	21.21	11.26	23.71	14.21
10.28	16.71	21.21	11.26	23.71	14.21
10.28	16.71	21.21	11.26	23.71	14.21

APPENDIX C : LIST OF PARTS

Num.	Part	Location	Manufacturer	Range or Description	Model Number
1	CFDRC Pressure Gage	FC-72 Loop	Wikai	-30 "Hg - +15 psi	-
2	Scavenge Pump	FC-72 Loop	Aquatec	Diaphragm pump	5850-7F12-B584 (DDP)
3	Air Accumulator	FC-72 Loop	Dangerden.com	Clear Reservoir	RESCYL
4	Heat Exchanger	FC-72 Loop	Lytron (McMaster)	4095BTU/HR	35145K514
5	Switch	FC-72 Loop	Hamlet (McMaster)	-	-
6	Pressure Gage	FC-72 Loop	Ashcroft	-30 "Hg - +100 psi	2071A
7	Switch	FC-72 Loop	Hamlet (McMaster)	-	-
8	Filter	FC-72 Loop	Swagelock	15 um	-
9	Flow meter	FC-72 Loop	Dwyer	0-12 GPH H2O	RMB-82-SSV
10	Reservoir	FC-72 Loop	MDC	Nipple	402006
11	FC-72 Pump	FC-72 Loop	Tuthill	Gear Pump	DDS1.3PPPV2NN37000
12	Filter	FC-72 Loop	Swagelock	15 um	-
13	Flow meter	FC-72 Loop	Dwyer	0-12 GPH H2O	RMB-82-SSV
14	Pressure Gage	FC-72 Loop	Wikai	-30 "Hg - +30 psi	-
15	Pressure Transducer	FC-72 Loop	Omega	0-100 PSIA	PX303-100A5V
16	Pressure Gage	Chamber	Wikai	-15 "Hg - +30 psi	
17	Pressure Transducer	Chamber	Omega	-	PX303-050A5V
18	Heat Exchanger	Water Loop	Lytron (McMaster)	4095BTU/HR	35145K514
19	H2O Pump	Water Loop	Grainger	Impellor Pump	4Z248D (Dayton)
20	Filter	Water Loop	Swagelock	140 um	-
21	Flow meter	Water Loop	Dwyer	0-12 GPH H2O	RMB-82-SSV
22	Reservoir	Water Loop	MDC	Nipple	402006
23	Spray Chamber	Chamber	MDC	Spec order Cross	404057-2006
24	Glass Pedestal	Chamber	New Port Glass	Dia = .625 +/- .01 in	Zkn-7 grade B or Better
25	Thermocouples	Chamber	Omega	Type E	EMQSS-0--G-12
26	View Ports	Chamber	AIN Plastics	Polycarbonate Sheet	540081-Clear
27	Nozzle	Chamber	Spraying Systems	Full Cone Spray	1/8G-1